Moritz Theissing, BSc

Correlative Microscopy: Combining X-Ray Spectroscopy, Raman Microscopy and Ultramicrotomy with Scanning Electron Microscopy

MASTER'S THESIS

to achieve the university degree of

Diplom-Ingenieur

Master's degree programme: Technical Physics

submitted to

Graz University of Technology

Supervisor

Ao.Univ.-Prof. Dipl-Ing. Dr.techn. Werner Grogger

Co-Supervisor

Dipl-Ing. Dr.techn. Armin Zankel

Institute of Electron Microscopy and Nanoanalysis

Graz, April 2021

AFFIDAVIT

I declare that I have authored this thesis independently, that I have not used other than the declared sources/resources, and that I have explicitly indicated all material which has been quoted either literally or by content from the sources used. The text document uploaded to TUGRAZonline is identical to the present master's thesis.

Date, Signature

Abstract

The investigation of sample volumes has become a well-established method in scanning electron microscopy (SEM) in the last 15-20 years. To achieve this task several commercial products are available on the market. Until now in most cases only imaging methods are used for data acquisition and therefore some scientific questions cannot be answered. With additional spectroscopic measurements, a deeper insight into a sample can be obtained.

In the first part of this thesis serial block-face scanning electron microscopy (SBFSEM) was combined with energy dispersive X-ray spectroscopy (EDX) and Raman microscopy. SBFSEM is a technique which uses *slice and view* for the investigation of volumes. In such an investigation the top surface of a sample gets imaged and then a thin slice is cut away. This process is repeated for a defined number of slices. The combination with EDX was already successfully implemented and published by the FELMI-ZFE, but should be repeated to test new instrumentation. Technically the combination of both methods could be successfully implemented, but with the present EDX system only inferior results were obtainable. During the experiment with EDX it was discovered that the backscattered electron (BSE) detector shadows the EDX detector in its conventional position. For recording of BSE images during the measurement a special detector holder was developed, manufactured and tested. For the combination with Raman spectroscopy, a transfer of the sample from the SBFSEM device to another SEM with an inbuilt Raman microscope and back had to be established. With a test sample Raman measurements could be successfully performed after a defined number of slices. The usage of Raman microscopy in a 3D investigation can help to determine the material compounds. This combination of methods was performed the first time.

In the second part of this thesis an alternative method for 3D SEM was tested in a materials science point of view. The new method automated tape collecting ultramicrotomy (ATUM) was originally developed for life sciences. It uses an ultramicrotome which cuts the sample into slices and collects them on a polymer tape. Compared to other 3D methods it was not possible to examine a paper sample, because of the swelling of the cellulose fibers in water, which changes the shape of the slices. For the evaluation of the micrographs of the slices the machine learning software *ilastik* was tested and applied. Despite poor image quality due to slicing artifacts this program produced image segmentations with a considerably high quality after little preceding image enhancement. The software *ilastik* was already successfully applied for the evaluation of SBFSEM micrographs. Additionally to imaging of a materials science sample prepared with ATUM, also spectroscopic measurements on the sections were performed successfully.

Kurzfassung

Die Untersuchung von Probenvolumina hat sich in den letzten 15 bis 20 Jahren zu einer etablierten Methode in der Rasterelektronenmikroskopie (REM) entwickelt. Um diese Aufgabe zu erfüllen, sind verschiedene kommerzielle Produkte auf dem Markt erhältlich. Bisher wird in den meisten Fällen nur die Bildgebung zur Datenerfassung verwendet, weshalb einige wissenschaftliche Fragen nicht beantwortet werden können. Mit zusätzlichen spektroskopischen Messungen kann jedoch ein tieferes Verständnis für den Aufbau einer Probe erhalten werden.

Im ersten Teil dieser Arbeit ist die Methode „serial block-face scanning electron microscopy“ (SBFSEM, *in situ*-Ultramikrotomie) mit energiedispersiver Röntgenspektroskopie (EDX) und Raman-Mikroskopie kombiniert worden. SBFSEM ist eine Technik, die das Konzept *slice and view* (Schneiden und Aufnehmen) für die Untersuchung von Volumina verwendet. Hierbei wird die Probenoberfläche elektronmikroskopisch aufgenommen und dann wird von der Oberseite der Probe eine dünne Schicht weggeschnitten. Dieser Prozess wird für die gewünschte Anzahl von Schnitten wiederholt. Die Kombination mit EDX wurde bereits erfolgreich implementiert und vom FELMI-ZFE veröffentlicht, sollte jedoch wiederholt werden, um einen neuen Detektor zu testen. Technisch konnte die Kombination beider Methoden erfolgreich implementiert werden, aber mit der vorliegenden Instrumentierung waren nur vergleichsweise schlechte Ergebnisse erzielbar. Während des Experiments mit EDX wurde festgestellt, dass der Rückstreuelektronen-Detektor (RE) den EDX-Detektor in seiner herkömmlichen Position abschattet. Für die Aufzeichnung von RE-Bildern während der Messung wurde ein spezieller Detektorhalter entwickelt, hergestellt und getestet. Für die Kombination mit Raman-Mikroskopie musste ein Transfer der Probe vom *in situ*-Ultramikrotom in ein anderes REM mit eingebautem Raman-Mikroskop und zurück durchgeführt werden. Mit einer Testprobe konnten Raman-Messungen nach einer definierten Anzahl von Schnitten erfolgreich durchgeführt werden. Die Verwendung der Raman-Spektroskopie in einer 3D-Untersuchung kann zur Bestimmung von Materialverbindungen beitragen. Diese Methodenkombination wurde zum ersten Mal durchgeführt.

Im zweiten Teil dieser Arbeit wurde eine alternative Methode für 3D-REM aus materialwissenschaftlicher Sicht getestet. Die neue Methode ATUM (automated tape collecting ultramicrotomy) wurde ursprünglich für die Biowissenschaften entwickelt. Dieser Ansatz verwendet ein Ultramikrotom, um die Probe in dünne Schnitte zu schneiden und diese auf einem Polymerband zu sammeln. Im Vergleich zu anderen 3D-Methoden war es nicht möglich, eine Papierprobe zu untersuchen. Aufgrund des Kontaktes mit Wasser während des ATUM-Prozesses quellen die Cellulosefasern und die Form der Schnitte ändert sich zufällig. Für die Auswertung der Aufnahmen der Schnitte wurde das *machine learning* Programm *ilastik* getestet und verwendet. Trotz der schlechten Bildqualität, aufgrund von Schneideartefakten, konnte das Programm gute Bildsegmentierungen mit wenig vorhergehenden Bildverbesserungen erstellen. Diese Software wurde schon zur erfolgreichen Auswertung der SBFSEM-Aufnahmen verwendet. Zusätzlich zu elektronenmikroskopischen Aufnahmen von einer materialwissenschaftlichen Probe, die mit ATUM präpariert wurde, wurden spektroskopische Messungen auf den Schnitten erfolgreich durchgeführt.

Acknowledgement

First, I want to thank Prof. Ferdinand Hofer (head of the ZFE) for giving me the possibility to write my master's thesis at the FELMI-ZFE and Prof. Werner Grogger for taking over the supervision of my thesis.

My greatest gratitude belongs to my co-supervisor Dr. Armin Zankel whose advice and support were essential for my thesis. He perfectly introduced me to SEM and the *3View* system and offered many ideas in the field of correlative electron microscopy, which could be realized in this thesis.

Further thanks to my colleagues at FELMI-ZFE. Especially to: Dr. Manfred Nachtnebel for his support with the *3View* system, Ing. Claudia Mayrhofer for preparing all microtomy samples, Dr. Stefan Mitsche who helped me with the EDX system, Dr. Harald Fitzek for the introduction to Raman spectroscopy and Ing. Hartmuth Schröttner, the group leader of the SEM group.

Special thanks go to the “Core Facility Ultrastructure Analysis” team of the Medical University of Graz, especially to Priv.-Doz. Dr. Dagmar Kolb for enabling my work with *ATUMtome* and *Atlas 5*. I also want to thank Kerstin Hingerl for her great support with *Atlas 5* software and Dominique Pernitsch, BSc for the perfect preparation of the sample with *ATUMtome*.

And another big thank you goes to my family and friends who supported me at all times during my studies.

This work was enabled by the project "HRSM-Projekt ELMINet Graz - Korrelative Elektronenmikroskopie in den Biowissenschaften" (i.e. a cooperation within "BioTechMed-Graz", a research alliance of the University of Graz, the Medical University of Graz, and Graz University of Technology), which was financed by the Austrian Federal Ministry of Education, Science and Research (BMBWF).

Table of content

List of abbreviations

ATUM	automated tape collecting ultramicrotome/ultramicrotomy
BSE	backscattered electrons
CNT	carbon nano tubes
cps	counts per second
ESEM	environmental scanning electron microscope/microscopy
HV	high voltage
LAI	large area imaging
LAM	large area mapping
LFD	large field detector
LIMI	light microscope/microscopy
PET	polyethylene terephthalate
RISE	Raman imaging and scanning electron microscopy
ROI	region of interest
SBFSEM	serial block-face scanning electron microscopy
SE	secondary electrons
SEM	scanning electron microscope/microscopy
SI	spectral imaging
SNR	signal to noise ratio
TEM	transmission electron microscope/microscopy
UI	user interface
VPSEM	variable pressure scanning electron microscope/microscopy
WD	working distance

1 Motivation

In the last 15-20 years the investigation of 3D volumes within scanning electron microscopy (SEM) has become a well-established method. Compared to classical tomographic methods like electron tomography in transmission electron microscopy (TEM) the 3D investigation methods of SEM use the concept *slice and view*. In such an investigation the top surface of a sample gets imaged and then a thin slice is cut away. This process is repeated for a defined number of slices. Until now in most investigations only imaging was used for data collection. By the evaluation of the images the digital 3D structure (morphology) of the sample can be generated and used for further characterization of the material. For some scientific questions imaging alone cannot provide enough information. In such a case the usage of additional spectroscopic techniques can help to answer further questions.

In the scope of SEM energy dispersive X-ray spectroscopy (EDX) comes to mind. EDX offers the possibility to get insight into the elemental composition of a sample. Lately Raman spectroscopy became used in correlative electron microscopy. Thus there are SEMs available with an inbuilt Raman microscope. With Raman microscopy it is possible to determine of which compounds a sample consists. This information is very useful during investigations of polymeric materials. The usage of these techniques can extend the results of a 3D investigation.

In the first part of this thesis the possibility of combining the *slice and view* technique serial block-face scanning electron microscopy, short SBFSEM (Denk and Horstmann, 2004) with spectroscopic techniques was tested. In this part the SBFSEM device *3View* was used for all investigations. The combination of *3View* and EDX was already successfully implemented as *3D elemental mapping* at the FELMI-ZFE with a different EDX system (Zankel et al., 2011). This experiment should be repeated within this work to test the capability of a recently installed new EDX detector for this method. The main of this method is a volume reconstruction of elemental maps. Interesting materials which can be investigated with *3D elemental mapping* are light alloys with a complex precipitate structure. Combining *3View* and Raman spectroscopy is a new approach and was implemented in this thesis. Both methods are on separate systems so a transfer between both was realized. The main motivation for such a combination is the possibility to characterize the sample during an investigation or the determination of newly discovered material phases during the experiment. For several polymeric or biobased materials this combination would enhance a conventional *3View* investigation.

The second part of this thesis evaluates the capability of the newer method automated tape collecting ultramicrotomy, short ATUM (Schalek et al., 2011), for 3D investigations with SEM in materials science. Such a test is interesting because the origin of the method is in life sciences. This method uses the slices cut by an ultramicrotome and collects them on a polymer tape for the investigation. The possible combination of this method with spectroscopic techniques is also discussed in this thesis. Due to the availability of the slices on the tape measurements in different devices are possible which can be interesting for materials which should be investigated with several techniques. For evaluation of the images cut by the ATUM device the machine learning software *ilastik* was tested and applied.

2 Introduction to the Methods

2.1 Scanning Electron Microscopy

Scanning electron microscopy (SEM) is a microscopic technique to investigate the surface of a (bulk) sample. The basic working principle contains a focused electron beam which scans the surface of the sample. Due to the interaction of the incident electron beam with the sample various signals are generated which are used to gather information about the sample.

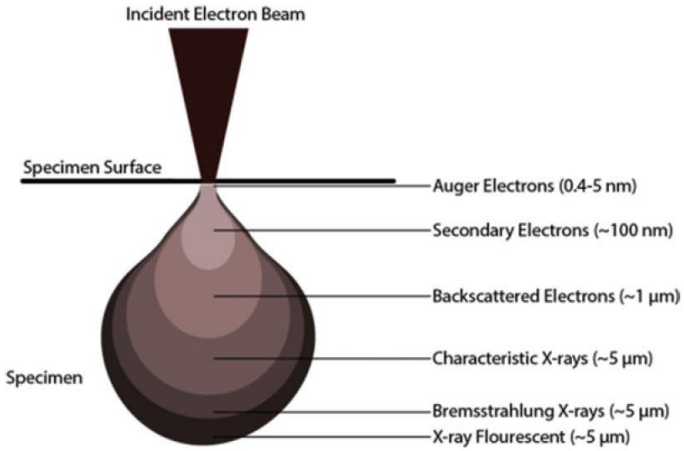

Figure 1: Typical interaction products of the primary electron beam and the sample in an SEM (Ul-Hamid, 2018)

In Figure 1 different interaction products (possible signals for the determination of the surface morphology, different phases and chemical information of the sample) caused by the impinging primary electrons are shown. This image illustrates only the most important interactions. There are additional more specific ones. In most cases the generated Auger electrons are not detected within a conventional SEM. The figure also shows the size of the interaction volume (the volume of the possible signal generation) for each signal. The size of the interaction volume is important because it determines the lateral and depth resolution. For imaging mostly secondary electrons (SE) and backscattered electrons (BSE) are used (more details how imaging works are given below). Characteristic X-rays (EDX) are used to gather information of the elemental composition of the sample (an introduction to this topic is given in section 2.3). The other signals are more specific and not regularly used in SEM.

Basically, an SEM consists of five main parts: the electron source, the magnetic lens system (optic system), the vacuum system, the specimen chamber and the detectors. Figure 2 shows a sketch of an SEM. In SEMs mainly two types of electron guns are used: thermionic emitters (cheap, worse energy spread) and field emission guns (more expensive, stable and have better energy spread). For the electron optics to work a high vacuum is needed which requires a suitable vacuum system in an SEM.

The lenses in the optic system lower the diameter of the electron beam. With the scan coils the focused electron beam is deflected in order to scan the surface of the sample. With the objective lens the electron beam gets its final diameter and is focused onto the surface of the specimen. Magnetic lenses suffer, like glass lenses, from lens aberrations. These aberrations

limit the maximum possible resolution of the system. In standard SEMs only astigmatism is corrected with multipole lenses. Within the optic system there are several apertures which are important to control the electron current. A higher electron current increases the signals (very important for EDX measurements), but in most cases the imaging quality is decreased due to a stronger impact of the lens aberrations.

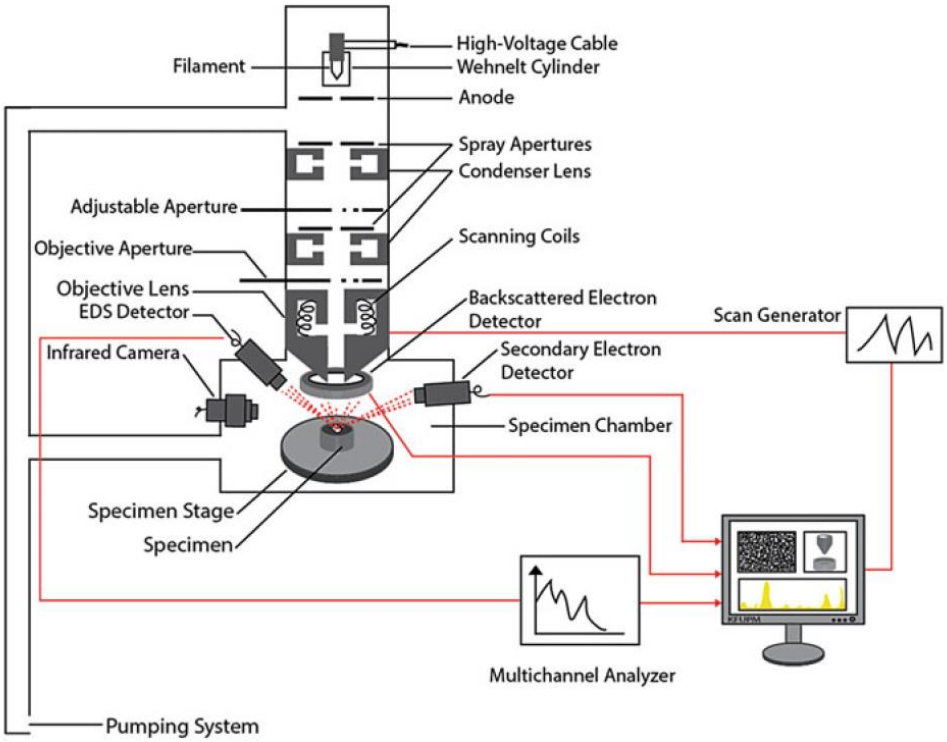

Figure 2: Schematic drawing of the most important parts of an SEM, more details are given in the text (Ul-Hamid, 2018)

The two imaging signals, secondary electrons and backscattered electrons, are distinguished by their origin and energy. Secondary electrons are produced by an inelastic scattering process of an incident electron with an outer shell electron in the sample. By definition all electrons which are leaving the sample with an energy $E < 50\,\mathrm{eV}$ are secondary electrons. Backscattered electrons are primary electrons which get elastically scattered at the sample atoms and leave the sample. By definition all electrons with an energy $E \geq 50\,\mathrm{eV}$ are backscattered electrons. The contrast of backscattered electrons is dependent on the atomic number Z (Z contrast). Higher atomic numbers (heavier elements) cause a stronger signal, because more backscattered electrons leave the sample.

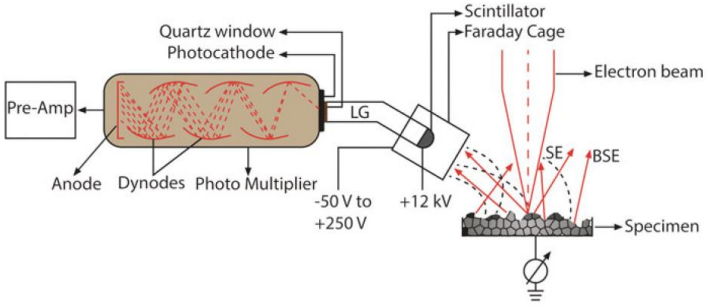

Figure 3: Sketch of the Everhart-Thornley detector for secondary electron detection (Ul-Hamid, 2018)

For secondary electrons the standard detector is the so-called Everhart-Thornley detector (Figure 3). The electrons get collected with a grid (in the sketch denoted as faraday cage) and are accelerated onto a scintillator. The scintillator signal is amplified by a photomultiplier and then detected. With this detector it is possible to record even backscattered electrons. With a negative grid voltage primarily a BSE signal is detected. In modern SEMs for the detection of the BSE signal mostly semiconductor detectors are used (Goldstein et al., 2017).

2.2 Variable Pressure Scanning Electron Microscopy (VPSEM)

In a conventional SEM an electrically conducting sample is needed for investigation, because the incident electrons cause charging (built up of negative charge near the surface layer of the sample) which leads to image distortions. Nonconductive samples can be investigated by applying a conductive coating (carbon evaporation coating, metal sputtering) on the sample. Such coatings compromise all samples in a certain degree and an alternative for the investigation of nonconductive samples is preferable. Such a technique is described in (Danilatos, 1988, 1991).

In contrast to a conventional SEM the VPSEM operates with chamber pressures in the range of $\sim 10 - 2500$ Pa. The higher pressure compared to high vacuum enables charge compensation by the gas molecules in the chamber (the negative charge induced by the incident electrons gets compensated). Thus charging of nonconductive samples can be avoided in a VPSEM. Due to the necessity of high vacuum in the column (electron optics) a special vacuum system is needed for the VPSEM. Figure 4 shows a diagram of the vacuum system. To separate the high vacuum of the column from the pressure in the chamber pressure limiting apertures (PLA) are used.

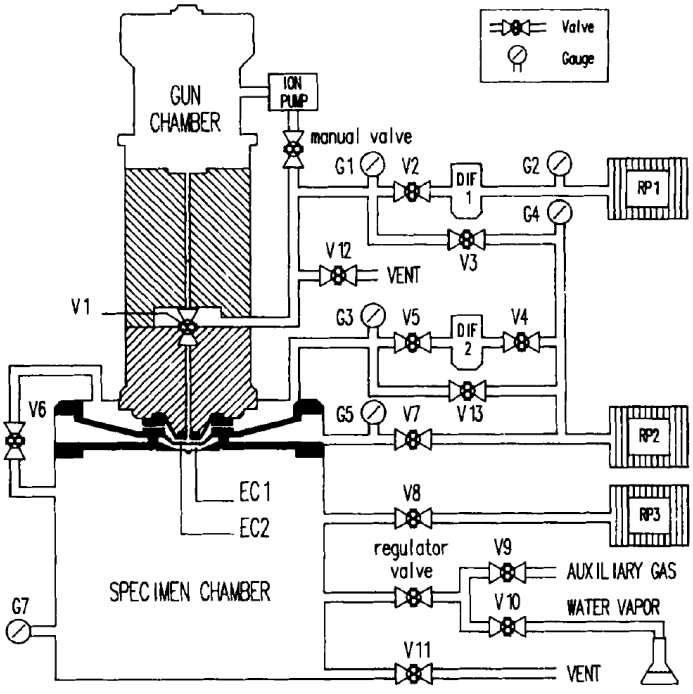

Figure 4: Schematic drawing of the vacuum system (Danilatos, 1991)

Imaging with the VPSEM works differently compared to the conventional SEM. For this work only chamber pressures up to 80 Pa were used. In this pressure regime BSE detection is performed with the semiconductor detectors which are also used in conventional operation in the SEM (high vacuum). For the detection of secondary electrons, the so-called large field detector (LFD) is used. Basically, the LFD is a positively biased electrode (up to +720 V) which attracts secondary electrons. Due to the acceleration of the SEs into the direction of the detector gas molecules in their way are ionized. The electrons, created by the ionization processes, themselves ionize more molecules creating an avalanche of electrons. This charge avalanche enhances the signal for image formation. This type of detector is only usable up to a pressure limit (200 Pa). Above this pressure an alternative detector in position of the BSE detector has to be used (Goldstein et al., 2017).

2.3 Introduction to Microanalysis – EDX

Energy dispersive X-ray spectroscopy (short EDX) is a technique for qualitative and quantitative elemental analysis which can be used in SEM. The method utilizes characteristic X-rays which are generated by the interaction of the beam and the specimen.

2.3.1 X-ray Generation

Two types of X-rays are generated by the interaction of high energy beam electrons and the atoms in the specimen: bremsstrahlung and characteristic X-rays. Characteristic X-rays are generated by an ionization process of atoms. A primary electron scatters inelastically with a bound inner shell electron of an atom and the bound electron gets ejected. This interaction process leaves the atom in an unstable excited state. The relaxation can happen in two possible processes: An outer shell electron relaxes in the vacancy and a characteristic X-ray gets emitted (the energy of the X-ray is the difference of the binding energy of the outer and inner shell). The second possible process is the Auger process. In this case also an outer shell electron relaxes in the vacancy, but a second outer shell electron is emitted (illustrated in Figure 5).

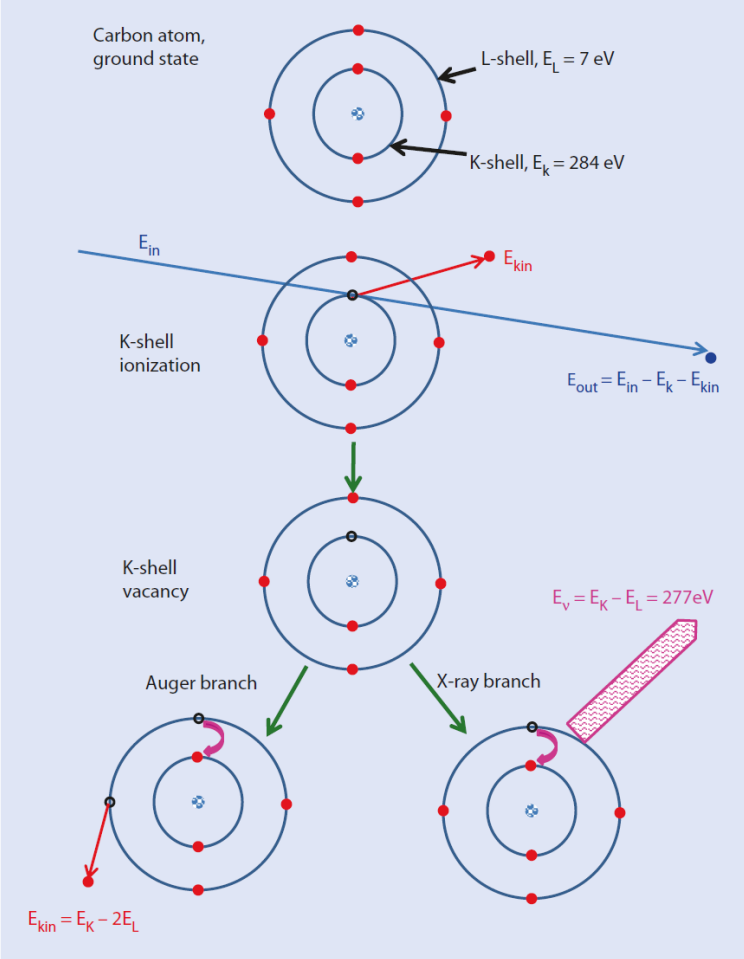

Figure 5: Generation process of characteristic X-rays (a carbon atom is used as example) (Goldstein et al., 2017).

Both processes are not equally probable. For low atom numbers the Auger process is more likely, heavy atoms emit mostly X-rays. This behavior is summarized under the term fluorescence yield.

Additional to characteristic X-rays, also a continuous spectrum is emitted the so-called bremsstrahlung. This type of radiation is generated if a primary electron gets decelerated in the specimen by deflection at atomic nuclei (Goldstein et al., 2017).

2.3.2 X-ray Detection and Spectrum Acquisition

The classical detector for EDX was the lithium-drifted silicon [Si(Li)] detector. The general working principle of this detector type is electron-hole pair generation in the detector crystal after an incident X-ray photon is absorbed. With an applied voltage electrons and holes are separated and the current pulse of the electrons is measured. The height of this pulse is proportional to the energy of the absorbed X-ray photon. In the last 15 years most of Si(Li) detectors are replaced by silicon drift detectors. This detector uses the same physical principle for detection (generation of electron-hole pairs), but the structure of the electrode is more complex to achieve higher count rates.

During spectrum acquisition some problematic phenomena can appear. The most prominent one is peak broadening – the characteristic X-rays appear as Gaussian like peaks and not like lines. The reason for this lies in physics and in the limited resolution of the spectrometers. Another phenomenon are silicon escape peaks. The origin of Si-escape peaks is X-ray generation within the detector. Coincidence or sum peaks are a phenomenon which happens if a second X-ray photon is absorbed in the detector during the measurement of another one, creating a peak at the summed energy of the photons.

Before spectrum acquisition there are parameters which can be altered in order to get the optimal result for specific tasks. The amplifier time constant of an EDX system defines how quickly an X-ray pulse is processed. Shorter time constants mean higher throughput, but lower resolution. With the channel width the energy resolution is determined. For large energy ranges only a larger channel width can be used due to limitations in the device. One of the most important parameters for spectrum acquisition is the dead time which is the amount of measurement time the spectrometer does not measure. It is used to compensate for spectral artifacts. The dead time is mostly influenced by the beam current (electron dose) which is related to the incoming count rate.

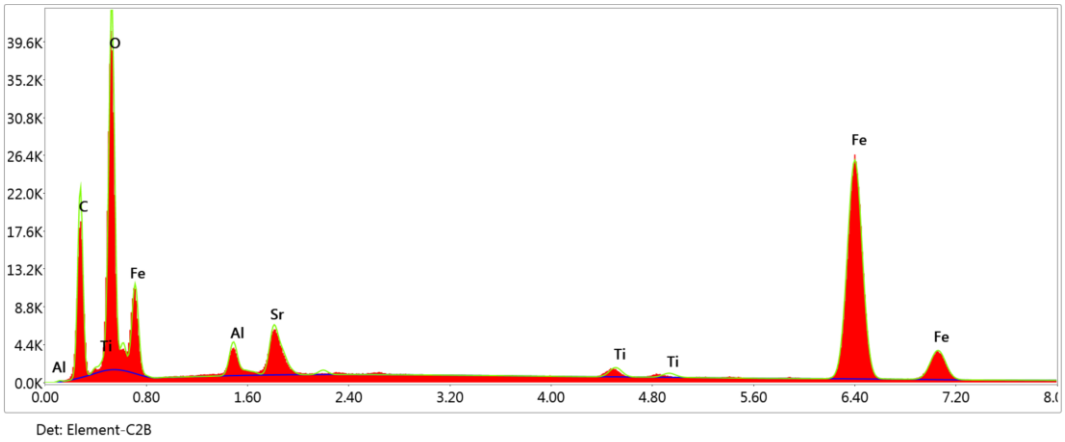

Figure 6: Example of an EDX spectrum

Figure 6 shows an example of a typical EDX spectrum. This spectrum consists of two parts: the background and the characteristic X-ray lines in form of Gaussian peaks (Goldstein et al., 2017).

2.3.3 Low Vacuum EDX

X-ray microanalysis in a variable pressure SEM (VPSEM) is generally possible, but there are effects which compromise the result of the experiment. The biggest influence on the result has the so-called skirt effect: primary electrons are scattered at gas atoms on their way through the chamber. This means that electrons hit the sample in the area around the nominal beam spot. The size of the area is described by the so-called skirt radius. In (Danilatos, 1988) an equation for the skirt radius R_s is given (single-event elastic scattering is used as assumption for the derivation):

$$R_S = 0.364 \frac{Z}{E} \left(\frac{p}{T}\right)^{\frac{1}{2}} L^{\frac{3}{2}}$$

In this equation R_s corresponds to the skirt radius in m, Z to the atomic number of the gas, E to the energy of the primary beam in keV, p to the pressure in Pa, T to the temperature in K and L to the path length in the gas in m. For better visualization of the skirt effect Figure 7 shows the skirt effect for H_2O (imaging gas). Obviously, a skirt radius up to 100 µm under conventional microscopic parameters in the VPSEM is expectable. Therefore, an EDX analysis of a micron sized object is compromised with spectral information of the skirt area around the examined spot.

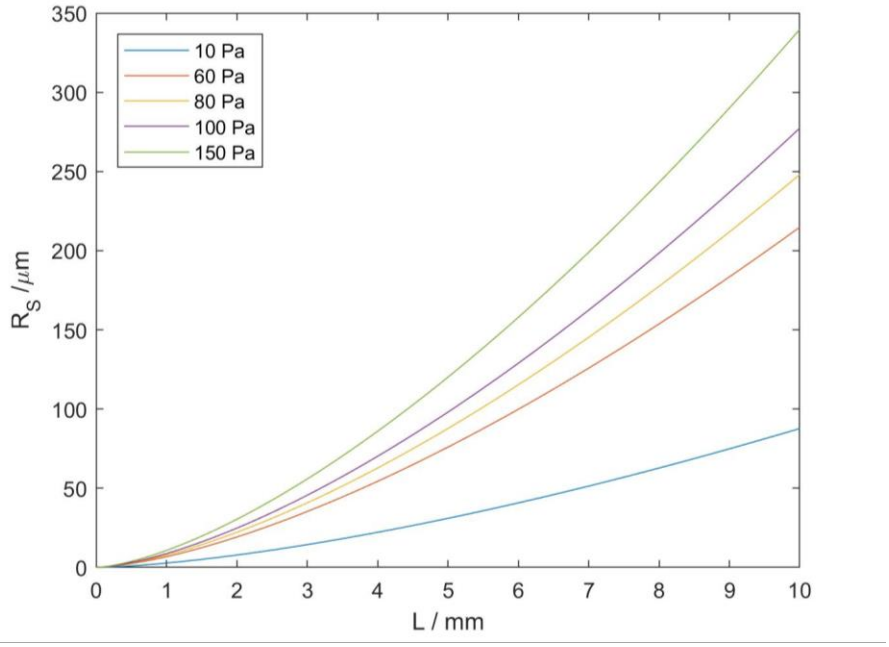

Figure 7: Skirt radius in water vapor for different pressures depending on the path length with Z = 7.42 (effective atomic number of water), E = 10 keV and T = 293.15 K (generated with MATLAB)

Another effect is the generation of X-rays in the imaging gas. The density of the gas (and often also the atomic number) is smaller than the examined material, but the path length in the gas is much longer. At higher pressures this can lead to an X-ray peak of the imaging gas.

2.3.4 EDX Mapping

With EDX mapping an image is created which has information about the elemental distribution by using characteristic X-rays. The basic working principle of this technique is an EDX measurement in every pixel of a defined region of interest (ROI). Before the introduction of silicon drift EDX detectors the classical Si(Li) detectors were used. With these detectors only relatively low count rates could be achieved and the data processing was also much slower compared to newer types. Therefore, only X-rays within certain energy windows (pre-defined elements) were counted. With this type of EDX map only a qualitative information of the elemental distribution is obtained and no additional elements can be added.

The more modern approach is the so-called spectral imaging (SI). The main difference to the method described above is that for each pixel a complete EDX spectrum is recorded and saved. The recorded data can be evaluated afterwards like quantification of the whole map. Adding new elements to the evaluation is also possible, because the whole EDX information is available.

For the acquisition of spectral images, a sufficient count rate is needed to maintain reasonable recording times. Each single spectrum needs a minimum number of counts in order to have a sufficient signal to noise ratio (SNR). The maximum count rate itself is capped by the processing speed of the detector. Additionally, high count rates cause significant peak broadening in the spectrum (this is important if two used X-ray lines are close in energy). In general, a larger pixel size compared to imaging is used, because the interaction volume of X-rays is much larger than for the imaging signals (Figure 1). A way to increase the spatial resolution is the use of a lower high voltage. The drawback of this approach is that lower electron energies only excite L-lines. For L lines the energy difference is smaller and therefore it is harder to distinguish between two lines (Goldstein et al., 2017).

2.4 Raman Spectroscopy

Raman spectroscopy utilizes inelastic scattering of light at a sample. Scattering of light is a phenomenon on molecular level. A molecule gets excited (it rises from the ground state to a virtual energy state) after the absorption of a photon. After a short time the molecule relaxes back into the ground state by emitting a photon. In the case of elastic scattering the emitted photon has the same energy, but most likely a different direction. This scattering process is called Rayleigh scattering. The second possibility is that the molecule relaxes from the virtual energy state to a vibrational excited state. Then the emitted photon has less energy than the incoming photon (the direction of the photon is also different). This type of scattering is called Stokes scattering. Sketched energy diagrams for both scattering types are shown in Figure 8.

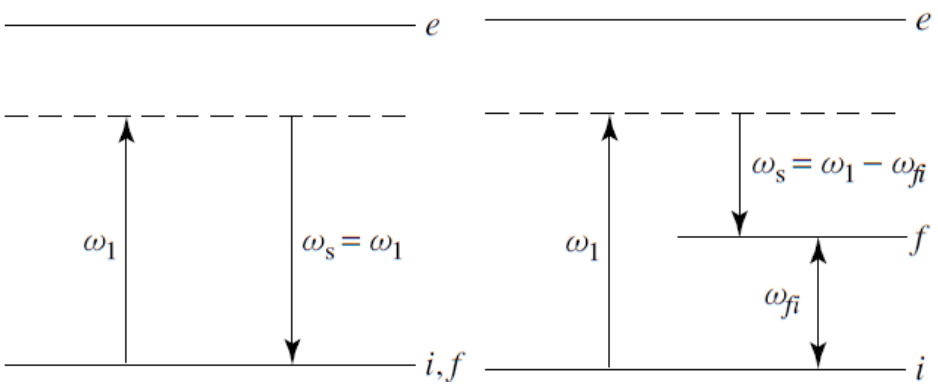

Figure 8: Energy diagram Rayleigh scattering (left), energy diagram Stokes scattering (right); ω_1 denotes as the frequency of the incident photon, ω_S denotes as the frequency of the scattered photon and ω_{fi} denotes as the transition frequency (Long, 2002)

Stokes scattering is often named Raman scattering. There are several more possible ways for Raman scattering, but a more detailed discussion would exceed the scope of this introduction (Stokes scattering is the most probable form of Raman scattering). A big drawback of this spectroscopic technique is that the probability of Raman scattering is much smaller than the probability of Rayleigh scattering (the probability of Rayleigh scattering is 10^8 times higher than the probability of Raman scattering). This fact needs to be implemented in the design of a spectrometer (Long, 2002).

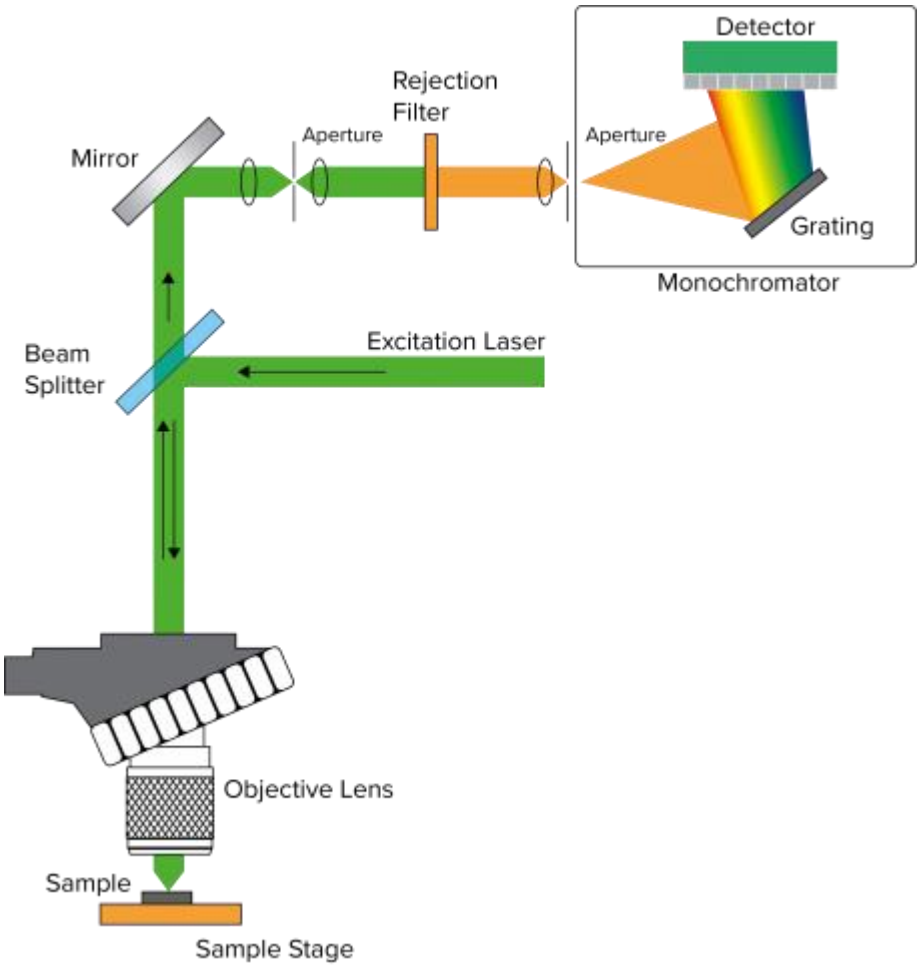

Figure 9: Basic setup of a Raman spectrometer (JASCO, 2021)

The basic setup (simplified schematic without the optical arrangement) of a Raman spectrometer is sketched in Figure 9. As light source a laser with adjustable power is used (the wavelength has to be chosen according to the needs of the investigation). Then the light interacts with the sample and the scattering processes described above take place. The outgoing light from the sample consists of elastically and inelastically scattered light. Due to the high probability of elastically scattered light this part has to be filtered out (otherwise the Raman signal would not be detectable). After the filter the remaining light enters the actual spectrometer. On a grid the light is separated by wavelengths and then the spectrum is recorded with a detector (Vandenabeele, 2013).

In a typical Raman spectrum not the wavelengths of the Raman scattered photons are shown, but the shift in wavelength compared to the primary wavelength is displayed. Figure 10 shows a typical Raman spectrum. The Raman shift is usually given in wavenumbers (cm^{-1}). The characteristic Raman peaks provide information about the composition (qualitative) of the material. It is also possible to get insight into other quantities of the material like stress/strain or crystal symmetry.

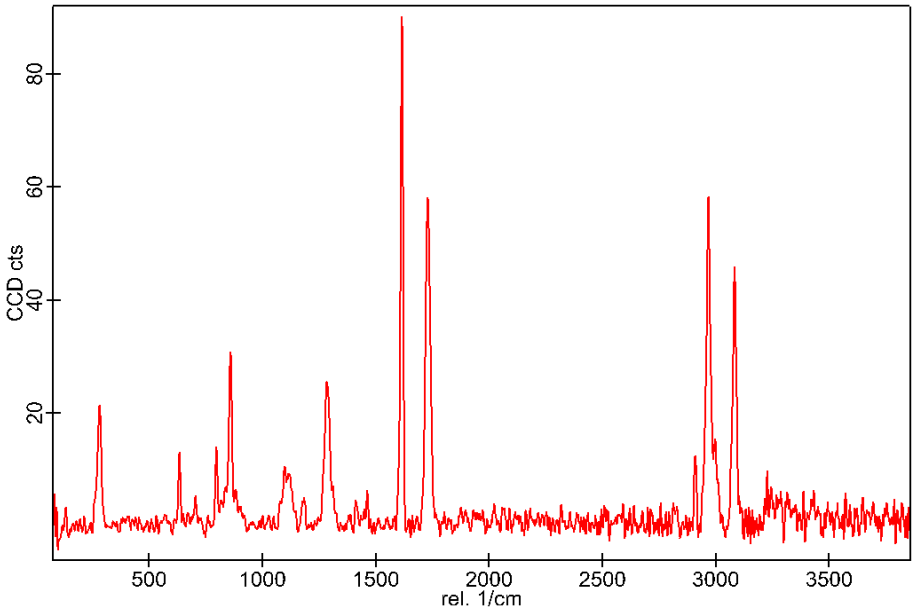

Figure 10: Example of a Raman spectrum

Like in EDX analysis it is also possible to acquire Raman maps with a suitable Raman microscope. For this procedure a Raman spectrum is recorded in each pixel of a defined ROI. The biggest drawback of Raman mapping are the long recording times needed for each spectrum.

2.5 SBFSEM – *in situ* Ultramicrotomy

Conventional SEM investigations can probe only the surface (or a small layer below the surface) of a sample. For some samples also an investigation of the volume would be interesting. One method to achieve 3D investigation within an SEM is serial block-face scanning electron microscopy (SBFSEM). This method was first described in (Denk and Horstmann, 2004) for the investigation of biological samples. The basic idea of this method is to image the block-face of a sample and then slice a thin layer from the top away and image the sample again. This process is repeated for the chosen number of slices. The main body of the system is an ultramicrotome which can be inserted into an SEM for *in situ* cutting. Therefore it is also called *in situ ultramicrotomy* in the ESEM. Ultramicrotomy on its own is a well-established sample preparation method in electron microscopy (Michler, 2019).

The ultramicrotome is mounted on a special door for the SEM (a sketch is shown in Figure 11a) and can be operated in the chamber of the SEM in vacuum. For navigation of the sample in the chamber, the whole device is mounted on a very precise stage (the conventional stage of the SEM is mounted on the original door of the SEM and therefore not available). The ultramicrotome itself consists (in the most basic view) of a sample holder and the diamond knife. A very precise motor connected to the sample holder is used to control the sample elevation (z-direction). The diamond knife itself is also motor driven.

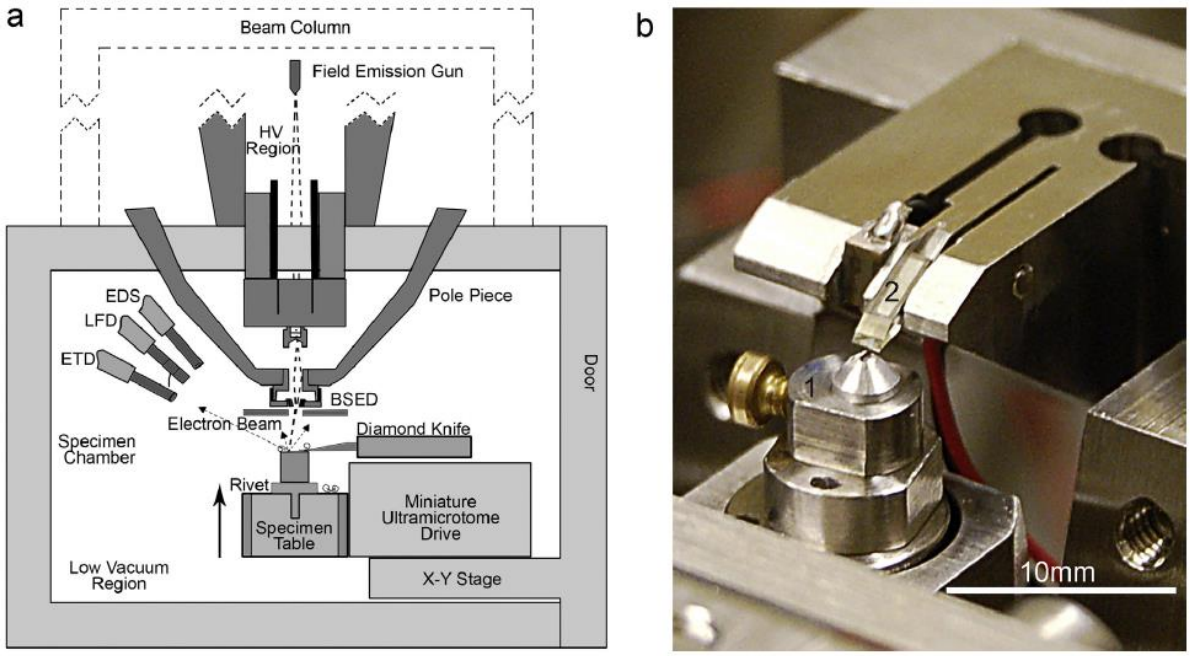

Figure 11: (a) Sketch of the *in situ* ultramicrotome and the chamber with possible detectors (more information in the text), (b) photograph of the sample holder with sample and the diamond knife (Zankel et al., 2014)

Before recording, the mounting and approach of the sample (see chapter 4) has to be performed. After this procedure the chamber is closed and the ultramicrotome can be operated under vacuum. For imaging the conventional detectors of an SEM are available (all possible ones are mentioned in Figure 11a). In Figure 11b a photograph of the sample holder (1) with the sample and the diamond knife (2) is shown. Usually the BSE detector is used for SBFSEM due to the flat imaging surface of the sample. The usage of energy dispersive X-ray spectroscopy is also possible (see section 5.1). A region of interest and a suitable pixel resolution is chosen. Additionally, a slice thickness (typically 50-100 nm) has to be defined. After alignment of the optics for imaging the actual SBFSEM process can be started: the first step is the recording of the ROI, then the sample is lifted by the defined slice thickness and the top layer of the sample is sliced away. This process is repeated for a defined number of slices. During an SBFSEM experiment it is recommended to stop the recording process in order to clean sample and knife from debris (residues from the slices cut) which accumulates on them. Unfortunately, there is no defined number of cuts when this cleaning process should happen, because this is strongly dependent on the investigated material (Zankel et al., 2014).

This concept was commercially implemented by the company *Gatan, Inc.* (Pleasanton, CA, USA) with the system *3View* (Genoud et al., 2008). With this device biological samples can be investigated, but also several materials science samples like polymers, paper or light metals/alloys (Zankel et al., 2009, 2014). In this thesis *3View* was used in combination with an *ESEM Quanta 600 FEG* from *FEI* (Eindhoven, The Netherlands).

2.6 Automated Tape-Collecting Ultramicrotome

Automatic tape-collecting ultramicrotomy (ATUM) is a relatively new technique for 3D reconstructions within SEM (Schalek et al., 2011). This method uses a series of ultrathin (50-100 nm) slices of samples cut by an ultramicrotome.

During the ATUM process the sections cut by an ultramicrotome are collected automatically by a moving polymer tape out of the water filled boat of the diamond knife. The tape works in this case like a conveyer belt for the thin sections. The tip of the tape collecting device has to be submerged in the water to ensure a successful collection by the tape (a weak stream in the water is induced which attracts the sections to the tape). This process is strongly affected by the shape of the block-face of the used microtomy sample (Baena et al., 2019).

After the collecting process the tape is transferred onto a silicon wafer. An electrically conducting adhesive tape is used to secure the polymer tape. The whole process is illustrated in Figure 12.

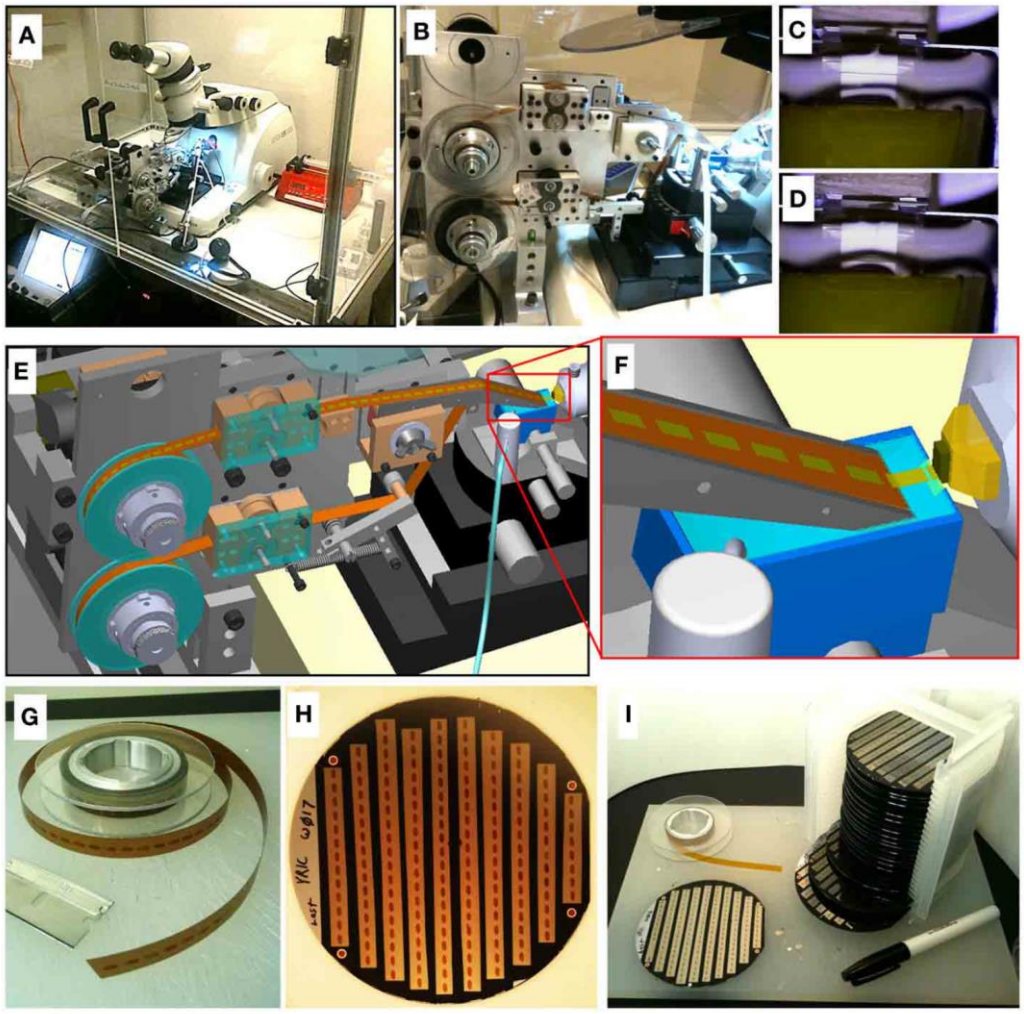

Figure 12: ATUM Process: (A) the ATUM device with the conventional ultramicrotome, (B) side view of the ATUM device, (C) and (D) cutting of a section, (E) 3D sketch of the ATUM device during operation, (F) 3D sketch of the knife and section collection during operation, (G) tape with the sections on it, (H) transferred tape on the silicon wafer, (I) several wafers of a section set (Hayworth et al., 2014)

Before imaging in a conventional SEM, an electrically conducting coating (frequently carbon is used) of the whole wafer needs to be applied. This step can be skipped if a VPSEM (or ESEM) is used for imaging.

There are some failures which can occur during the collecting process: there is a possibility that sections are lost or break during cutting. Wrinkling of sections is another problem which occurs sometimes. In literature it is stated that the (partial) loss of 1-2 sections per 100 sections should be no problem if they are not consecutive (Hayworth et al., 2014).

The company *RMC Boeckeler Instruments, Inc.* (Tucson, AZ, USA) has commercially implemented ATUM-SEM with the product name *ATUMtome*. Additionally there are a few choices which polymer tape (type or special coating) is used for section collecting. The type or coating can have a significant impact on imaging and additional analytical investigations. An example for this are PET tapes coated with carbon nanotubes (CNT) which should improve the imaging of biological tissues (Kubota et al., 2018).

3 Image processing

Concerning 3D investigations of samples in SEM, image processing is a crucial part for data evaluation. Frequently a first step is a digital 3D reconstruction of the volume. To achieve this task the individual phases of the sample need to be segmented on each image of an image stack. An image stack is a series of separate images combined in one file. The data of SBFSEM are mostly saved using image stacks. Therefore, the image segmentation is very important for the analysis (see section 3.2). Before an image segmentation can take place frequently additional image enhancement is needed.

3.1 Image Enhancement with *FIJI*

For image enhancement the open source software bundle *FIJI* was used. *FIJI* is a distribution of the open source image analysis program *ImageJ* with several preinstalled useful plugins (Schindelin et al., 2012). In this work only basic image transformations and a so-called denoising of images was performed. Figure 13 shows an SEM micrograph (recorded with a BSE detector) with typical problems after an SBFSEM investigation which need to be addressed by image enhancement. Several regions which are problematic for image segmentation are marked.

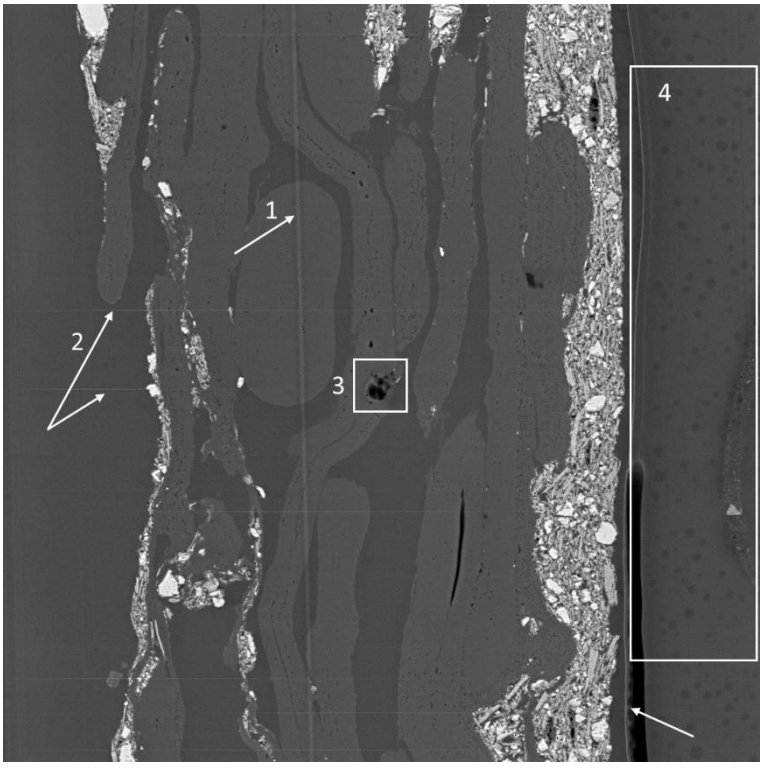

Figure 13: Typical raw image of a 3D investigation in the SEM. Several problematic regions for image segmentation are marked with numbers. (sample: paper label, image width: 68.31 µm, BSE detector)

Arrow 1 marks a relatively vertical line. This line is a groove created by a notch in the diamond knife during the cutting process. If a problem occurs in combination with the knife, then all images of this session are affected by this error. Unfortunately, there is no good way to remove this line without compromising the rest of the image. Filters were tested for removing the lines, they but did not work. With a general denoising (see below) this line gets a bit less

prominent, but on the whole this artifact has to be addressed in image segmentation. The horizontal lines marked by the arrows 2 have their origin most probably in instabilities in the vacuum system. They occur randomly on some sections. Like for the vertical line there is no sufficient possibility to address them.

The square on position 3 marks a region with strong beam damage. It occurred due to a wrong beam resting position during the 3D investigation process (SBFSEM). Such damages need to be addressed, because they do not represent the real structure of the sample. Due to the fixed position of the damage during the investigation the fastest way to address this issue is to manually correct it. On the right side (region 4) there are several issues which complicate image segmentation. Near the sample there is a layer (marked with a white arrow) which got detached from the sample (in this state no useful information is provided for a 3D reconstruction). In the whole marked area, there are spots with different grayscales (this value should be constant over the whole area, because the same material should result in the same BSE contrast). Most probably the spots are a result of beam damage. In section 3.2 it is explained why such spots are a big problem for the image segmentation process. Left from the sample area there are also inhomogeneities in the background (embedding resin). Such inhomogeneities are problematic for image segmentation. Since no information about the sample is in this area the best countermeasure is the removal of the whole background area.

A problem which can occur during an SBFSEM investigation is debris on the block-face within the region of interest. Figure 14 shows such a situation. For this issue a very easy solution is possible if only one successive section is affected. The according micrograph can be interpolated with a simple average of the previous and the following image.

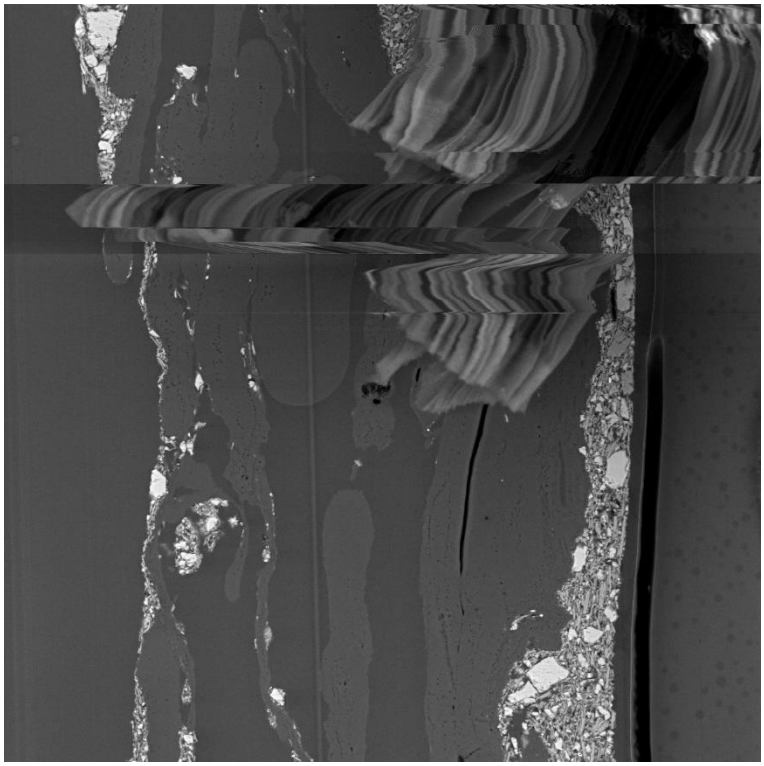

Figure 14: Block-face image with debris on the cutting surface within the region of interest (sample: paper label, image width: 68.31 µm, BSE detector)

Figure 13 and Figure 14 suggest that the raw images are noisy. In Figure 15a an enlarged part of such an image is shown. Here it is obvious that the recordings have a strong noise which makes segmentation much harder. The denoised image is shown in Figure 15b. For denoising the *ImageJ* plugin *Non Local Means Denoise* (Wagner and Behnel, 2016) was used. The theoretical background for this plugin is given in (Darbon et al., 2008) and (Buades et al., 2011).

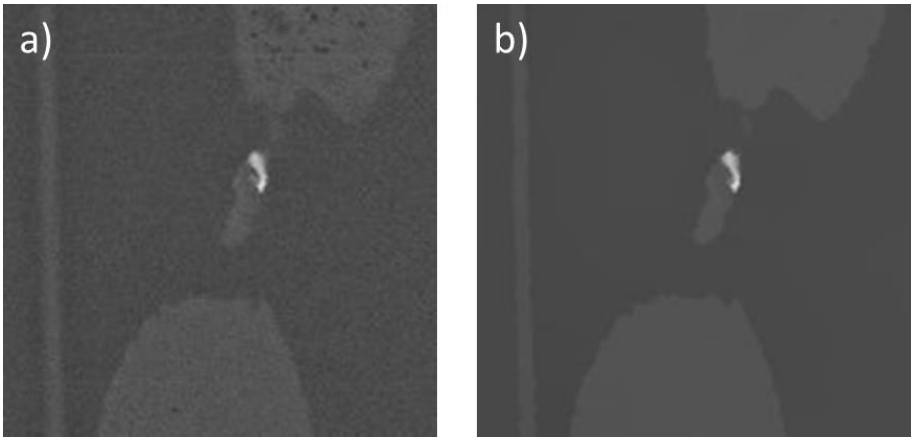

Figure 15: Close-up of a typical BSE image of SBFSEM: a) raw image b) image after an applied denoising algorithm (image width: 8.9 µm)

To achieve this kind of denoising the plugin was applied several times (in most cases up to 5 times) with a small sigma value (represents the standard deviation of the noise). With this approach it is possible to get images with a low noise and maintained edges. The application of the plugin with high sigma values results in blurry edges. An example for a recording after the whole image enhancement process is shown in Figure 16. With this quality the segmentation process was performed.

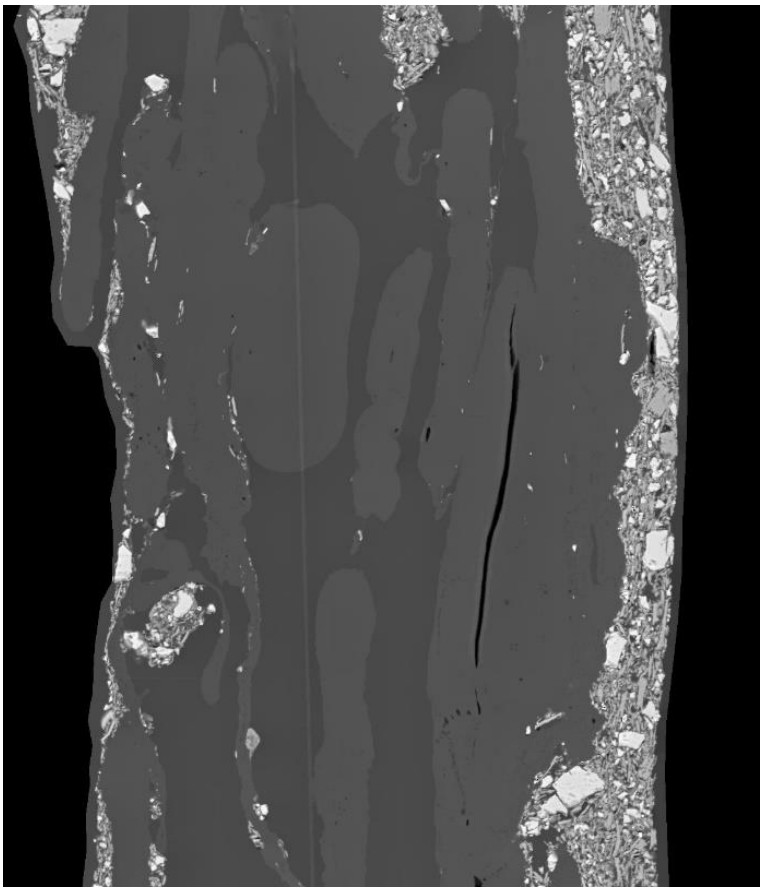

Figure 16: Example for an SBFSEM micrograph after the whole image enhancement process (sample: paper label, image width: 58.6 µm, BSE detector)

3.2 Image Segmentation

Image segmentation has the goal to digitally separate all phases which are interesting in a sample. In the case of the example of the previous section there are four phases which are typical for paper. Figure 17 marks these phases: region 1 includes the cellulose fibers, region 2 marks the areas with the embedding resin (this is basically background), region 3 marks filler materials and region 4 marks voids within the sample. The black areas on the side are introduced during image enhancement to eleiminate the gradient in grayscale of the embedding resin.

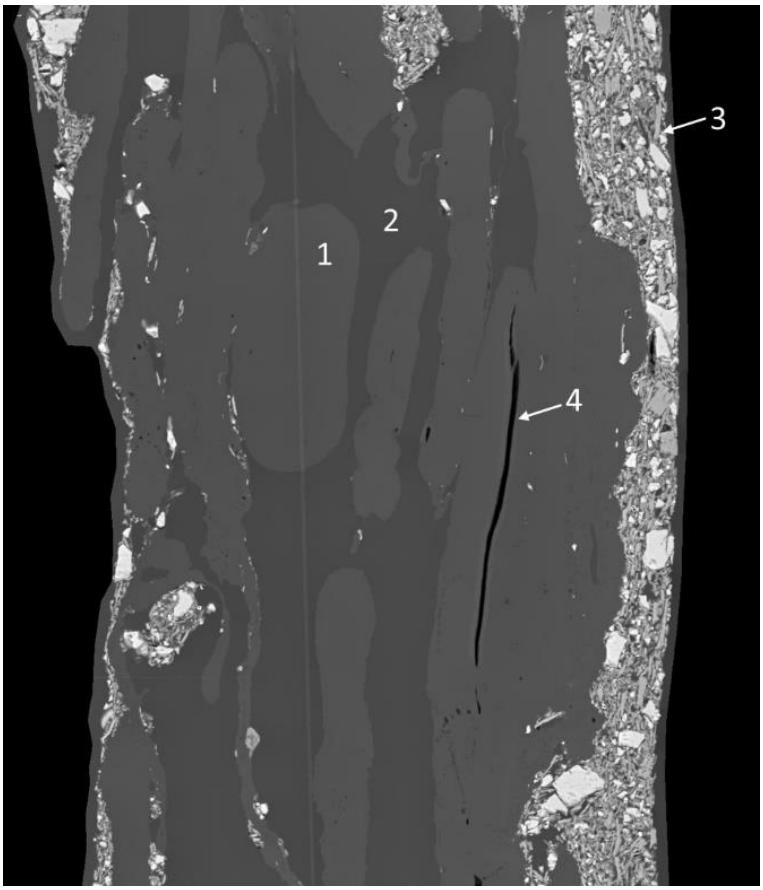

Figure 17: Phases of an exemplary paper sample which should be segmented: region 1: cellulose, region 2: embedding resin, region 3: filler particles, region 4: voids (image width: 58.6 µm, BSE detector, after image enhancement)

In this thesis only two methods of image segmentation were used: basic (global) thresholding and interactive machine learning. Thresholding is a basic function of *ImageJ* and therefore a part of *FIJI*. For the interactive machine learning approach, the open source software *ilastik* (Berg et al., 2019) was used. The working principle of global thresholding is trivial: a cutoff grayscale is set to separate two phases. The calculation of separated phases with thresholding, even for a large number of images, is very fast. The main drawback of this approach is that phases need a distinct difference in contrast. Only very few samples deliver such a high image quality intrinsically. In most cases thresholding needs sophisticated image enhancement to work. Segmentation of the example image with standard thresholding is impossible, because the grayscales of several phases have overlapping values.

A newer approach in the field of image segmentation is the use of interactive machine learning algorithms. With these methods it is possible to segment images with complicated phase structure (like the example given in Figure 17) without the usage of extensive image enhancement. In the following the working principle of *ilastik* during image segmentation is explained. Evaluation of large datasets starts with the training of the so-called classifier (a non-linear algorithm which is used to calculate the image segmentation of the dataset). Training of the classifier starts with the selection whether a 2D dataset (images of the same sample which are independent of each other) or a 3D dataset (the dataset describes a volume or timeseries) is evaluated. The process itself is similar for 2D and 3D datasets.

Feeding the program with a suitable training set which represents the data is crucial. Unfortunately, the question what size such a training set should have cannot be answered explicitly. Generally larger datasets provide better results, but on the other hand large datasets result in very long computation time. For a suitable calculation time these two opposing arguments need to be balanced. After selection of a training set the “feature selection” is performed. In this stage scales for different features like color/intensity, edge and texture are chosen. These scales can be selected in a 2D and 3D context. In most cases a larger number of scales deliver better results, but also increase the computation time. Then the actual training process starts.

In Figure 18 the process of training is illustrated. The starting point is the training set (for illustrative purposes the training set for this segmentation consists only of one image). For each phase a label in *ilastik* has to be defined. Figure 18b shows the labels for the selected image: yellow for epoxy resin, blue for cellulose, red for filler material, light blue for voids and green for the arbitrary additional background (the extra label is needed for better results). After a fast marking of the image the first calculation of *ilastik* (the algorithm tries to segment the image) is performed. The result is shown in Figure 18c. For the little amount of input information, the result is not bad, but obviously there are some problems (examples are marked with the white arrows). Areas with wrong image segmentation get corrected by hand and the segmentation is recalculated. This process is repeated iteratively until the result is fitting. Figure 18d shows the result from this demonstration run, where some areas are not perfect (due to the limited training set and the complexity of the image). An example is marked with a white arrow. On this position *ilastik* has problems with the vertical line (in most areas the line gets filtered out). The best way to deal with such minor problems is to correct the segmentation manually afterwards with *FIJI*.

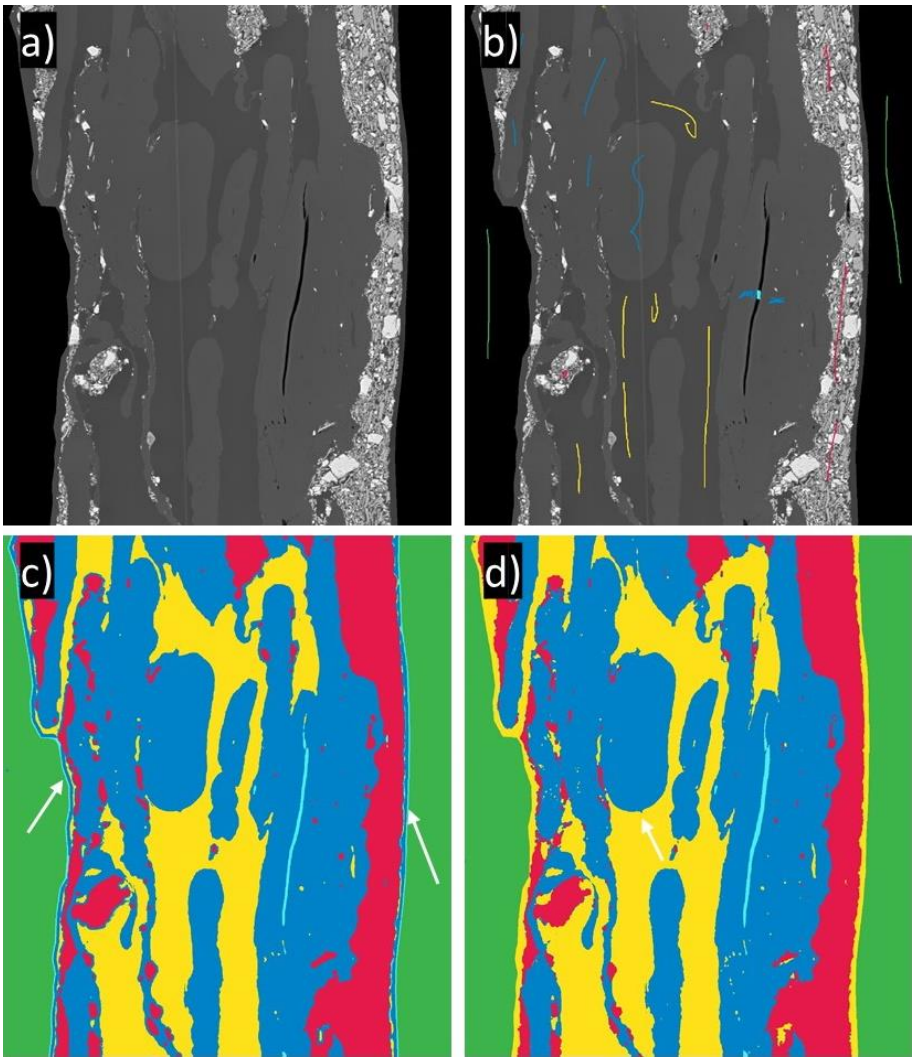

Figure 18: Training process of the classifier in ilastik: (a) training image (raw data after enhancing), (b) manually drawn marks for each phase, (c) first result after calculation with ilastik, (d) final result after iteration (image width: 58.6 µm, BSE detector, after image enhancement)

With the trained classifier the actual dataset is evaluated (also the results of the training set are exportable). Due to the 3D experiments in this thesis only segmentation of 3D volumes was used. As training set 30 consecutive images were used in form of an image stack to train the classifier as explained above. The evaluation of the residual dataset afterwards is relatively fast. The program *ilastik* needs that the evaluated image stacks have the same size as the training stack. Retraining of the classifier was only needed if a strong change in contrast happened.

3.3 Summary Image Processing

This chapter shows the steps which are needed for the evaluation of micrographs in a 3D investigation. By the usage of the machine learning program *ilastik* the preceding image enhancement can be limited to a reasonable amount. In most cases only a denoising was applied and area with beam damage were corrected manually. The segmentation process of complex materials was performed in one step with *ilastik*. After the application of ilastik only minor problems in the image segmentations were fixed manually.

4 Optimization of the Sample Adjustment in *3View*

The adjustment of a sample in *3View* is a time-consuming procedure with several individual steps. In this thesis an optimization for some steps of this process was realized and documented. For the adjustment several steps are needed:

- Insertion and centering of the rivet (cylindrical sample holder with a cone shaped top where the sample gets glued onto) with sample in the *3View* holder
- Aligning the holder in *3View* and centering of the diamond knife
- Mechanical approach of the sample height in relation to the diamond knife
- Final height approach with the motor

Insertion of the rivet (with sample) into the *3View* is a trivial step. The centering of the sample on the other hand is a very important step. Due to the limited lateral movement ability of *3View* it is important to place the sample in the middle in order to have access over the whole sample area. To simplify this task a stereo microscope with a target in the ocular is available.

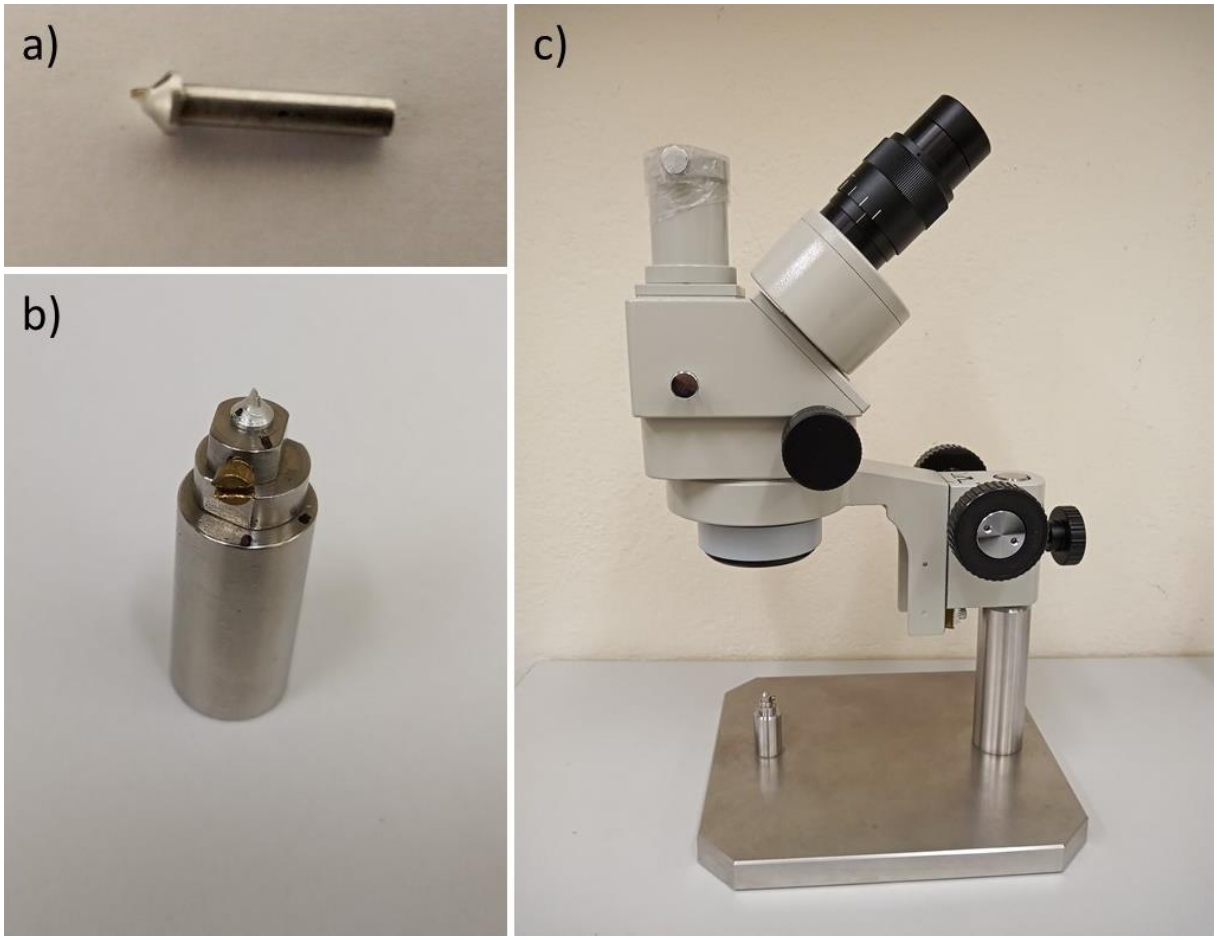

Figure 19: *3View* adjustment: (a) sample glued onto a rivet, (b) *3View* sample holder with rivet, (c) stereo microscope for the centering of the sample and for other alignment steps

In *3View* the sample holder also needs an adjustment. It is important that the edge of the sample which is near the knife is parallel to the edge of the diamond knife (rotational alignment). For help during the adjustment a stereo microscope can be mounted on the *3View* door with a special holder. After the position adjustment the sample holder gets loosely locked

with a screw (to prevent rotation but allow upward movement). The knife position itself is also an important parameter of a successful *3View* investigation. Due to the limited movability of the knife (1,200 µm) it is important that the sample gets completely cut before the end of the knife movability (the cut should be completed at a knife position of 700-800 µm). The knife position can be manually altered in *DigitalMicrograph* (software for controlling *3View* from *Gatan*). Before the adjustment the knife gets cleaned with polystyrene sticks which are purged with ethanol. Before the next step the accessibility of all positions on the block-face of the sample is tested by imaging in the SEM due to the limited lateral movability of *3View*. In this step the illumination of the stereo microscope could be improved by using a ring light (Figure 20a).

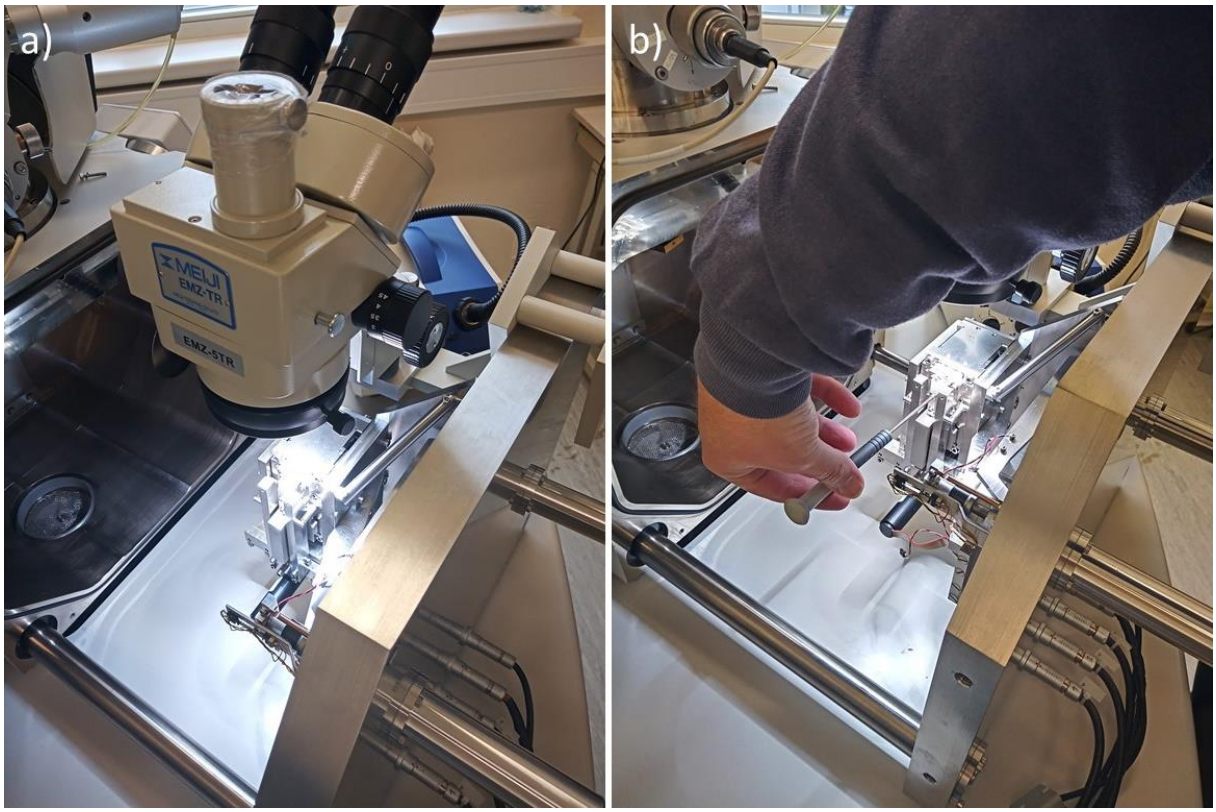

Figure 20: *3View* adjustment: (a) rotational adjustment of the sample, (b) locking of the rotational adjustment

The most time-consuming step of sample adjustment in *3View* is the manual height approach of the sample block-face to the edge of the knife. In this step it is crucial to toggle the option *stroke up* in *DigitalMicrograph* before starting with this step (stroke up brings the sample in cutting position which is ~30 µm higher than the imaging height) in order to perform the adjustment in the highest possible sample position. If the sample is too high before a cut or touches the knife during moving up, the knife can be significantly damaged. To adjust the height a screw below the fixation screw (see Figure 20b) is used. In a first step the approach is done by eye (a visible distance between sample and knife should remain). After the approach by eye a 45° mirror (polished aluminum) and the stereo microscope is used to get a magnified view of the distance between sample and diamond knife. For illumination the ring-light delivers better results than the previously used point light source (flashlight). For better results a wider mirror out of technical aluminum should be manufactured and polished. After the approach with the mirror the stereo microscope gets moved in a tilted position and the

sample/knife area get illuminated from behind with a flashlight. In the right position a linear gloss parallel to the knife's edge is visible. With *stroke up* and *stroke down* it is checked if the gloss originates from the sample. If so, the gloss is used for a final manual approach. After this step the fixating screw is tightened.

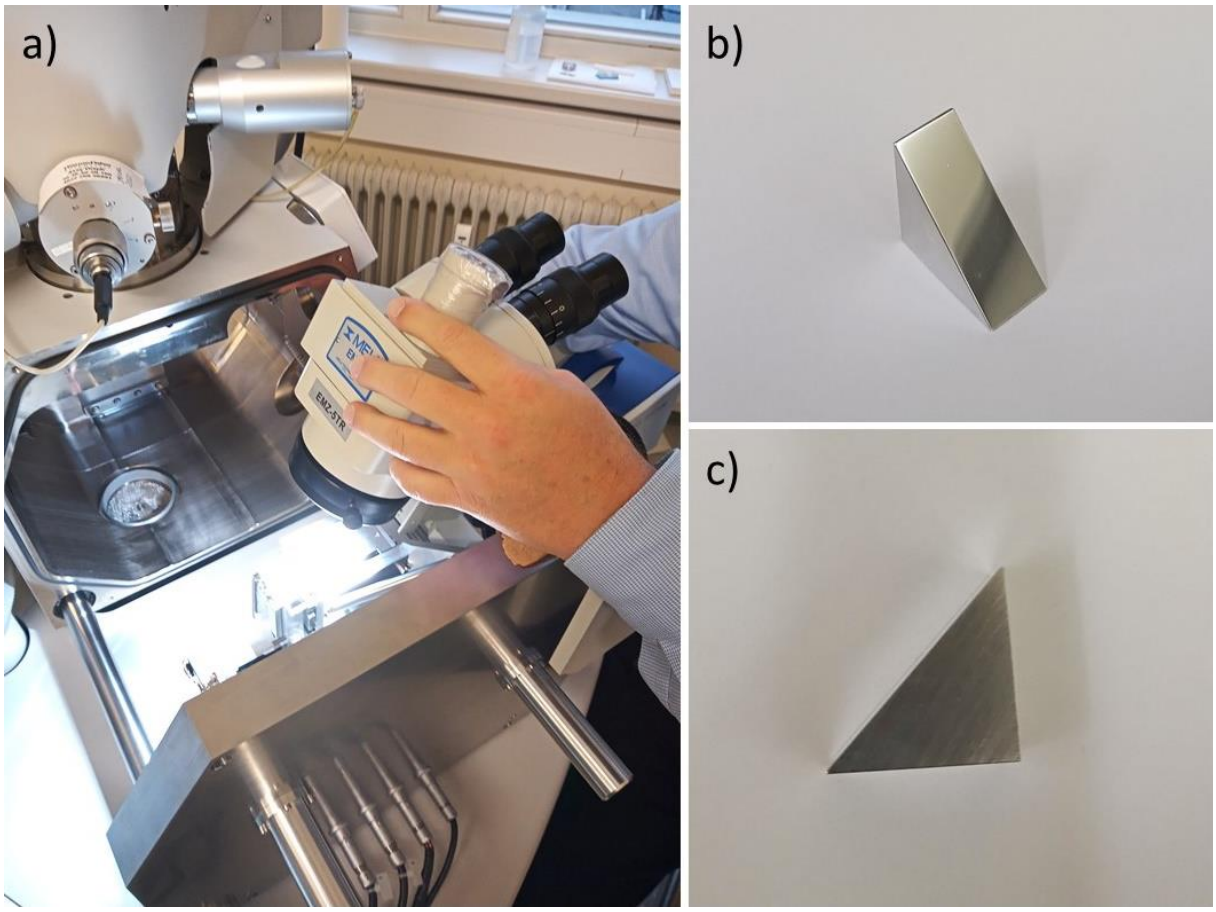

Figure 21: *3View* adjustment: (a) stereo microscope in tilted position, (b) and (c) 45° aluminum mirror (polished)

The rest of the approach is performed with the operation of *3View* with an open chamber. In the approach mode (only cutting) the option for cutting 200 nm thick slices is used to move the sample up in a safe manner. This process is observed with the stereo microscope. The cutting is performed until the first small sample part is cut. The cutting process itself is not visible, but after a cut small particles which are on the knife have an altered position or new particles are on the knife. In this step the usage of the ring light improves the observation of the process.

The first successful cut does not mean that a slice from the whole sample is removed. Due to minor misalignments in angle, the sample block-face and the cutting plane of the knife are not perfectly parallel to each other. For a perfect parallelism between both a small number of cuts (100 nm thick) is needed. These cuts are performed with SEM imaging (*slice and view*) with low magnification to monitor the progress. After changes are visible on the whole imaged area the adjustment of the sample is finished. In a further step a ROI is defined and the actual investigation is performed.

5 Combining *3View* with EDX – *3D Elemental Mapping*

A conventional serial block-face SEM (like *3View*) is limited to imaging (in most cases BSE are used). In general, already images deliver a fair amount of information about the sample (an example is the volume morphology of a specimen). In some cases, on the other hand, standard imaging does not provide the information to fully understand a material. An example for such a case are different precipitates in an aluminum alloy. With imaging alone, it is not possible to distinguish the precipitates and to get information about the composition. Here additional EDX measurements would be helpful.

5.1 *3D elemental mapping* – Introduction

The main aim of combining EDX with a 3D investigation using *3View* is the possibility to get insight into the composition of the material. There are two possibilities to implement an EDX measurement into this process: manual measurements (spot or mapping measurements) at slices of interest or an EDX mapping on each slice. The first possibility is fairly simple to implement. The *3View* experiment needs to be stopped at a slice of interest and then the desired measurements are performed. The second approach is called *3D elemental mapping* with the aim to generate a data set which contains an EDX spectrum for each voxel (one could say an EDX spectrum imaging in three dimensions). This approach was first implemented by (Zankel et al., 2011).

An alternative method to slice samples for a 3D reconstruction is dual beam focused ion beam microscopy (FIB). With such a device *3D elemental mapping* was first developed by (Schaffer et al., 2007). A dual beam FIB is an SEM with an additional ion beam, which can be used for removing layers of the sample (analog to the cutting of the sample with *3View*). The interaction of the electron beam with the sample generates the characteristic X-rays which are recorded as EDX spectrum images.

The basic workflow of *3D elemental mapping* is fairly easy. Figure 22 shows the schematic workflow of 3D elemental mapping which was used for this thesis. Obviously, the starting point of such an investigation is the selection of a ROI. The first step of the *3D elemental mapping* cycle is the image acquisition with the EDX software. Then the spectrum image is acquired. After the recording one cut with *3View* in the approach mode (in this mode only a cut is performed, and no image is recorded) is performed. This cycle is repeated for the desired number of slices. The controlling software of *3View* *DigitalMicrograph* is capable of recording EDX spectrum images, but in our case the software was not compatible with the used detector. If the EDX acquisition could be implemented into *DigitalMicrograph* the automatization of this process is very easy. In a setup with the EDX software and *DigitalMicrograph* an automatization is possible using a program which can control GUIs.

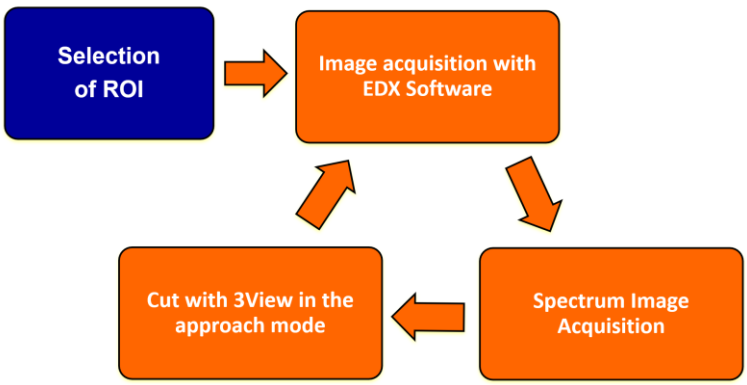

Figure 22: Sketched workflow of *3D elemental mapping*

The main obstacle of this method is the acquisition of the spectrum images. Recording EDX spectra with a suitable number of counts requires pixel dwell times which are magnitudes longer than dwell times needed for standard imaging. EDX spectra with too few counts do not provide a SNR which is good enough for elemental identification and in a further step quantification of the spectrum. Quantification is a very important step to determine the phases (two phases of a sample can contain the same elements in a different composition) of the sample. The parameters of the EDX measurement must therefore be selected that the spectrum image can be recorded in a reasonable time. For a good workflow the time needed for each slice should be under 10 minutes. To achieve this comparatively fast spectrum image acquisition high count-rates are needed. To enable these high count-rates a large electron current of the primary beam (high electron doses can harm the sample and cause beam damage) and an EDX detector with large detector area and high throughput are needed. A downside of high count-rates is peak broadening which lowers the resolution of the spectrum.

The bigger problem of EDX analysis is the significantly lower depth resolution compared to imaging (see Figure 1 for the size of the interaction volume where characteristic X-rays are generated). To prove this point Monte Carlo simulations with *CASINO* (Drouin et al., 2007) of the generation depth of characteristic X-rays were performed for an aluminum sample (with *3View* only soft metals like aluminum or magnesium are sliceable) for several typically used high voltages. The results of these simulations are shown in Figure 23.

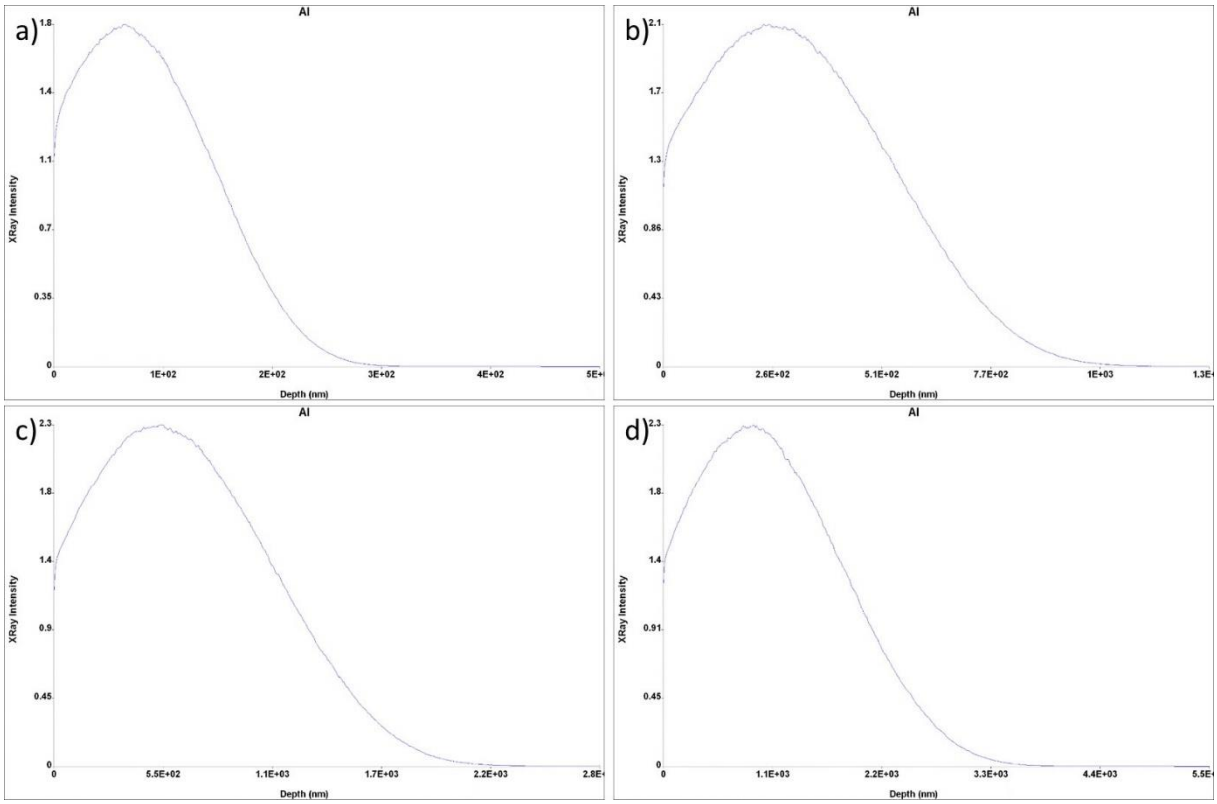

Figure 23: Monte Carlo simulations of the X-ray generation depth in aluminum for different high voltages: (a) HV = 5 kV, (b) HV = 10 kV, (c) HV = 15 kV, (d) HV = 20 kV

For each simulation the trajectories and interactions with the sample were calculated for 100,000 electrons in order to get reasonable results. In the case of a high voltage of 5 kV most of the characteristic X-ray intensity (K-line of aluminum) is generated in a depth within 100 nm. But also, for this low beam energy a significant number of X-rays is generated beyond 100 nm. For higher energies the generation depth of the peak intensity gets larger. In the case of 20 kV most of the characteristic X-rays are generated in a depth within 1 µm. The best strategy for a good depth resolution is the usage of beam energies as low as possible (in most cases 5 keV is a practical boarder, because for this electron energy most elements are detectable by K, L or M lines).

5.2 Motivation, Sample and Instrumentation

The concept of *3D elemental mapping* was already successfully tested by the FELMI-ZFE with a borrowed EDX system. For this thesis it was decided to repeat the experiment, because a new EDX detector is available on the microscope (the first test was performed with a borrowed detector).

To test *3D elemental mapping* the aluminum alloy AW-2024 T351 (an Al-Cu alloy) was chosen as sample. The typical composition of this alloy is shown in Table 1. It is a common alloy used for aerospace and automotive applications.

%	Si	Fe	Cu	Mn	Mg	Cr	Zn	Ti
min	-	-	3.80	0.30	1.20	-	-	-
max	0.50	0.50	4.90	0.90	1.80	0.25	0.15	0.15

Table 1: Composition of the alloy AW-2024 T351 (Aluminium Batz + Burgel, 2019)

The sample preparation in this case is different from standard *3View* samples. The aluminum sample got turned into a rivet shape by the institute's workshop. With glass knives then a block (rectangular shape on the top) is carved out from the top of the rivet. This block can then be cut with a conventional ultramicrotome to produce a block-face. In Figure 24 a photograph of the prepared sample is shown.

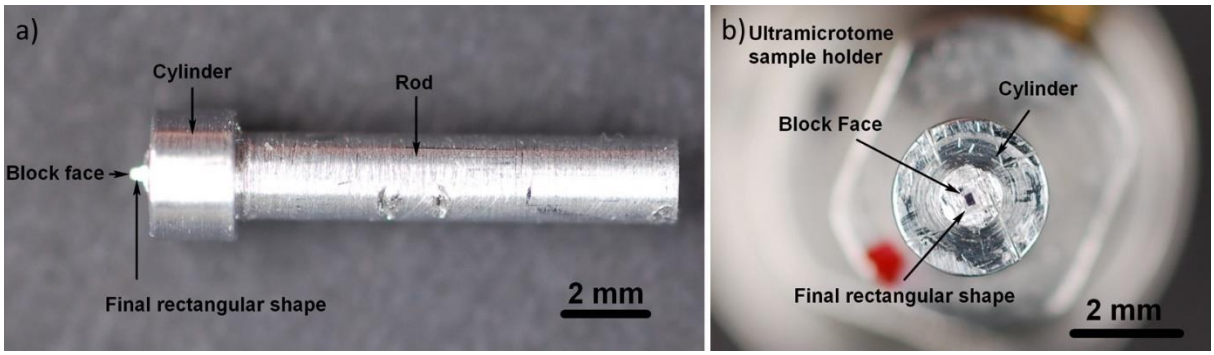

Figure 24: Al sample for *3D elemental mapping*: (a) view from the side, (b) view from the top (paper draft by Herbert Reingruber 2011 – not published)

The rivet shaped sample can then be mounted and adjusted in *3View*. Figure 25 shows a BSE image of the block-face of the sample. Within the aluminum matrix (gray) there are several precipitates with various sizes. The irregularities in the matrix (horizontal stripe like shapes) are created by channeling contrast (the surface of the sample is very flat and different grains of the aluminum matrix produce different contrast). For such a sample not only the morphology of the precipitates (several different size classes) is of interest, but also the composition of each precipitate.

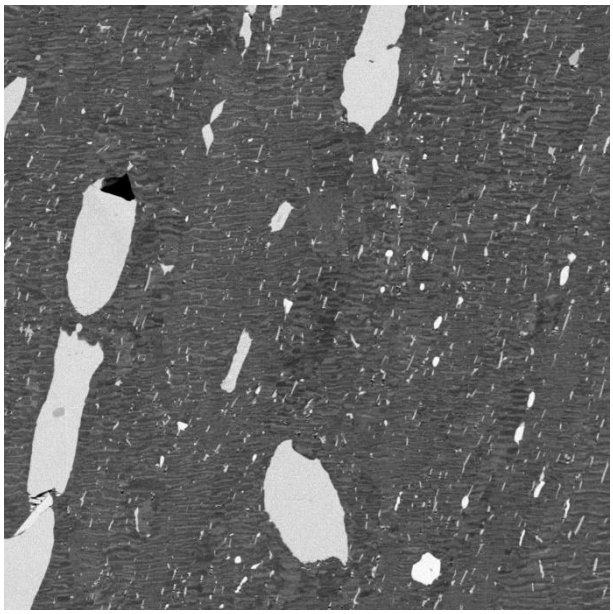

Figure 25: BSE image of the block-face of the aluminum sample (image width: 31.3 µm)

For the acquisition of the EDX spectrum images an *EDAX Element* detector with the *APEX 1.0* software from the company *EDAX, Inc*. (Mahwah, NJ, USA) was used. The EDX detector has an area of 30 mm^2 which is medium sized. In preliminary tests an intersection distance (optimal working distance for the detector to operate) of 9 mm was obtained (the result of this measurement is shown in Figure 87 in the Appendix). This working distance (WD) cannot be realized, because the WD for *3View* investigations is fixed at about 7 mm. At this WD it is therefore challenging to get a high enough count rate. Another problem arose because both available BSE detectors shadow the EDX signal during *3View* investigations.

5.2.1 BSE Detector Holder

Due to the shadowing problem the BSE signal cannot be used during the *3D elemental mapping* process. Alternatively with the Everhart-Thornley detector it is possible to record images with BSE contrast (by applying a negative voltage to the grid all SEs are repelled and only BSE can enter the detector), but the signal is noisier. To have a BSE signal during the measurement the idea arose to mount the semiconductor detector on the side of the column with a special holder. Due to the angular distribution of BSE this idea has a physical fundament (Goldstein et al., 2017). The dependence of the BSE emission coefficient η of the angle φ is given by:

$$\eta(\varphi) \propto \cos(\varphi)$$

To illustrate this formula the angular distribution of BSE is sketched in Figure 26.

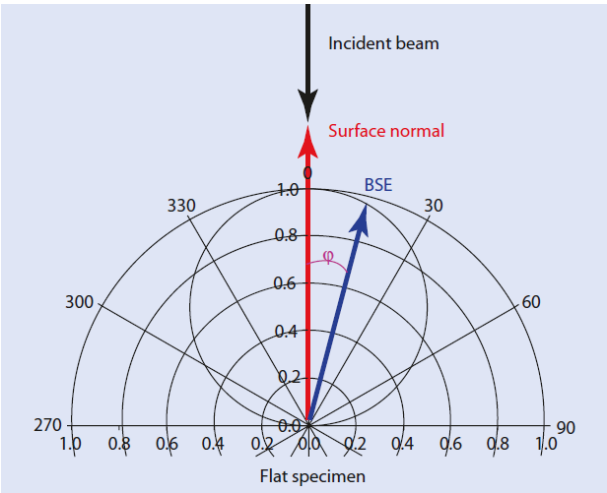

Figure 26: Illustration of the BSE emission coefficient η in dependence of the angle φ (Goldstein et al., 2017)

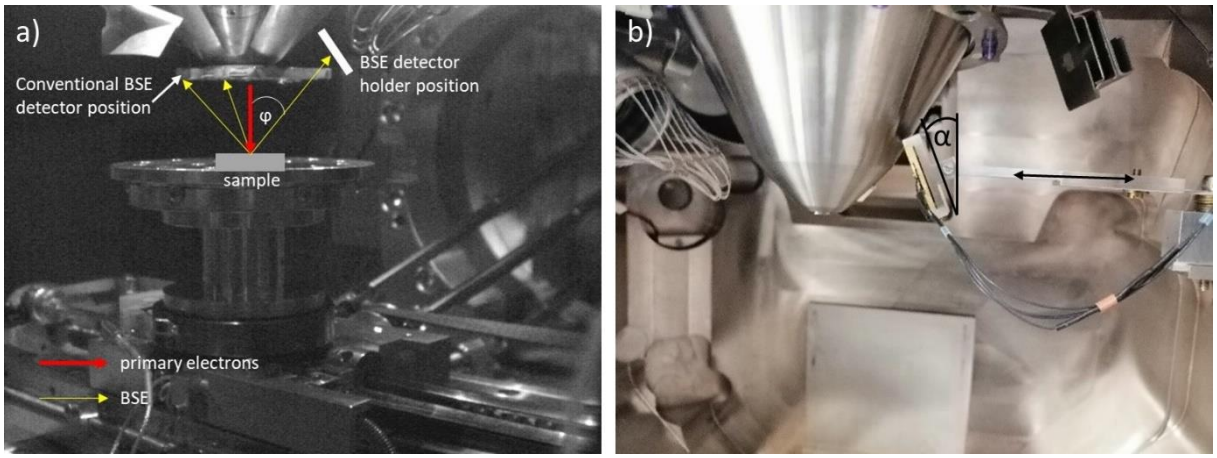

Figure 27: Implementation of the BSE detector holder: (a) a photograph of the chamber with the sketched position of the BSE detector, (b) actual implementation of the BSE detector holder

In Figure 27a a photograph of the chamber with the mounted BSE detector (standard position) is shown. The sketched additions illustrate the idea of moving the detector to the side of the column. Figure 27b shows the actual implementation of the holder with marked adjustment possibilities. The holder is mounted on a side-flange of the microscope.

For testing the holder, the angle α is varied over the whole range from 0° to 90°. The length adjustment is used to position the holder directly beside the column. The measurement of the angle was performed with printed photographs of the holder and manual angle measurement with a square (a sketch of the measurement is shown in Figure 88 in the Appendix). Because a two segment BSE detector is used for each tested angle a conventional BSE image (A+B – both segments are added) and a topographic BSE image (A-B – segment B is subtracted) were recorded. At ideal angle both segments detect approximately the same number of backscattered electrons and therefore the A-B image should show the least details. In Figure 28 the results of this measurement series for 5 angles are shown. The A-B image for α ≈ 8° in this experiment (Figure 28d) shows almost no contrast which indicates that this is the optimal angle (within a range of a few degrees due to measurement uncertainties).

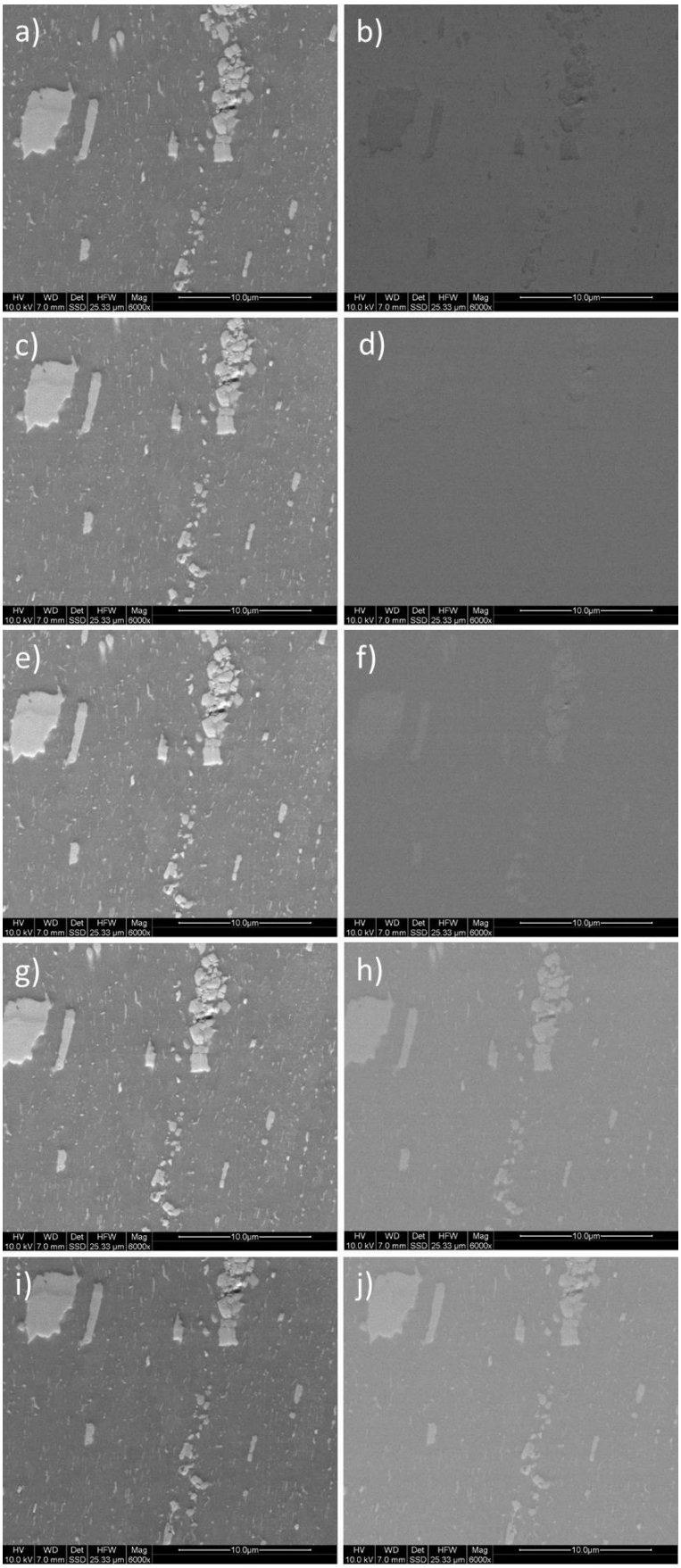

Figure 28: Results of the BSE detector holder test at different angles: (a) A+B image for α ≈ 0°, (b) A-B image for α ≈ 0°, (c) A+B image for α ≈ 8°, (d) A-B image for α ≈ 8°, (e) A+B image for α ≈ 15°, (f) A-B image for α ≈ 15°,(g) A+B image for α ≈ 35°, (h) A-B image for α ≈ 35°, (i) A+B image for α ≈ 55°, (j) A-B image for α ≈ 55°

In Figure 29 BSE images of the aluminum sample after the determination of the appropriate angle α are shown. The left image was recorded with the BSE detector in the standard position, the right image was recorded with the BSE detector in the special holder at the ideal angle α. Unfortunately, both images are not from the same sample area, but they are regardless comparable. The main difference is that the image which was recorded with the BSE holder is noisier (a fewer number of electrons reach the detector due to the angular distribution) and the image shows a three-dimensional impression (asymmetric position of the detector). An interesting observation was that best images were recorded at small angles α. The two segments of the BSE detector are the most probable explanation of this behavior, because more BSE are present near the column. A steeply mounted BSE detector counters the imbalance of the BSE by lowering the effective area (less BSE can hit the detector segment) of the upper segment.

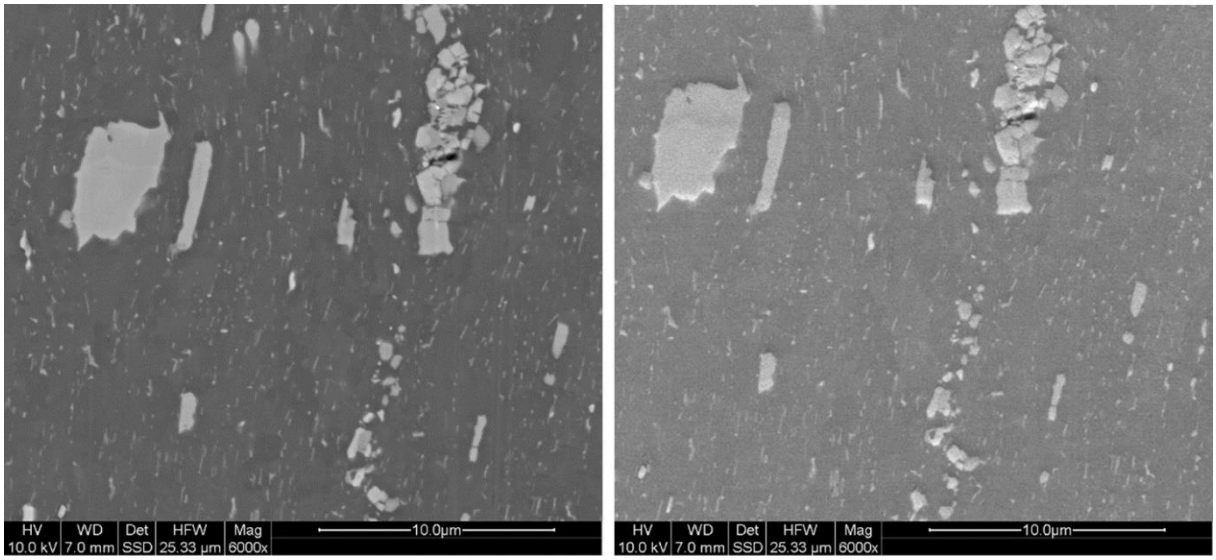

Figure 29: BSE images of the aluminum sample. Left: BSE detector in the standard position below the column, right: BSE detector in the special holder for α ≈ 8°

5.3 Morphological 3D Investigation of the Sample

Before *3D elemental mapping* a morphological reconstruction of the sample was performed to get insight into the precipitate sizes and distribution. On the previous images of the sample (Figure 25 and Figure 29) a large distribution of precipitate sizes is visible. To have the highest possible resolution in depth a slice thickness of 50 nm was chosen. Slice thickness is one side of a good depth resolution. It is also important to choose a high voltage with a maximum BSE generation depth in the range of the slice thickness (otherwise the depth resolution would be compromised by information of a larger depth than the slice thickness).

To choose the appropriate high voltage Monte Carlo simulations for different high voltages were performed with *CASINO* (Drouin et al., 2007). The results of these simulations are shown in Figure 30. For the simulations the interaction of 100,000 primary electrons with the sample was calculated for different high voltages. Due to the imaging with backscattered electrons the maximum generation depth of BSE is important which can leave the sample surface. For a high voltage of 2 kV the maximum depth would be about 30 nm, for 3 kV the maximum depth

is in the range of 60 nm (most of the generation happens below 50 nm). Higher accelerating voltages have a much larger generation depth. In terms of depth resolution, imaging with 2 kV would be ideal, but with such a low beam energy it was not possible to acquire BSE images. With 3 kV fast imaging is possible and this high voltage was therefore chosen for the 3D investigation.

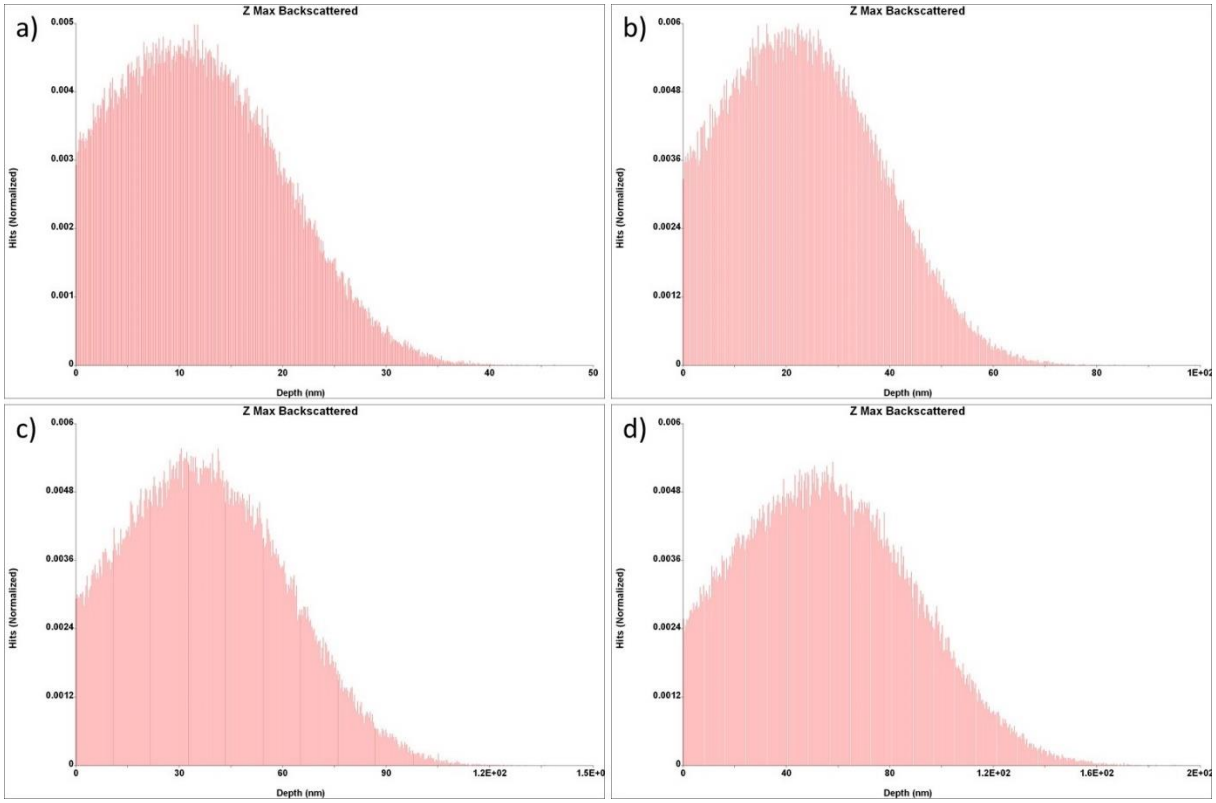

Figure 30: Monte Carlo simulation of the BSE generation depth in aluminum. (a) HV = 2 kV, (b) HV = 3 kV, (c) HV = 4 kV, (d) HV = 5 kV

For the 3D investigation 1000 slices of the sample were recorded with optimized imaging parameters. The recording was performed with the BSE detector from *Gatan* in conventional position. The imaging parameters were:

- Lateral resolution: 31 nm/px
- High voltage: 3 kV
- Pixel dwell time: 30 µs
- WD: 7.1 mm
- Pixel resolution: 1000x1000 px

Because aluminum is conductive the investigation can be performed in high vacuum (most SBFSEM samples are non-conductive and can only be imaged in low vacuum), which eliminates imaging instabilities of the low vacuum mode. In total a volume of 31x31x50 μm^3 was investigated. The cutting process worked smoothly (after 800 cuts small debris accumulated on the surface, which made the evaluation impossible). In terms of sliceable materials aluminum is not the first material which comes into mind but cutting with a diamond knife is possible. The material gets chipped away like turning on a lathe in a workshop. Figure 31

shows an overview of the situation in *3View*. The carved-out sample block is in the middle with aluminum rolls (they got chipped away during cutting) around it.

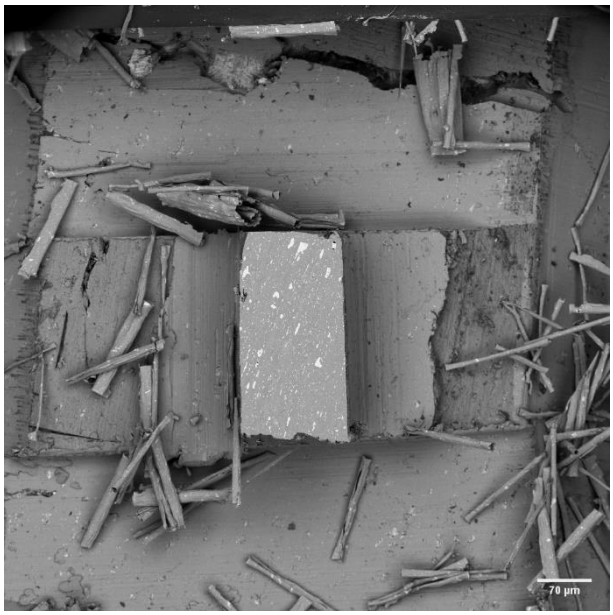

Figure 31: Overview image of the sample block with the block-face in the middle and aluminum rolls around, which got chipped away during cutting

For data evaluation the image enhancement and segmentation described in chapter 3 was applied (in this case simple threshold segmentation). In Figure 32 the recorded data (left) and the segmented images (right) are represented with the function *ortho slice* of the 3D visualization and analysis software *Avizo 9.0* from *FEI*. *Ortho slice* is a way to visualize a 3D image data set (image stack). It can plot several images of an image stack in different planes (x-y, x-z, y-z). In the ortho slice representation of the raw images a sharp contrast change is visible (both parts need to be segmented separately).

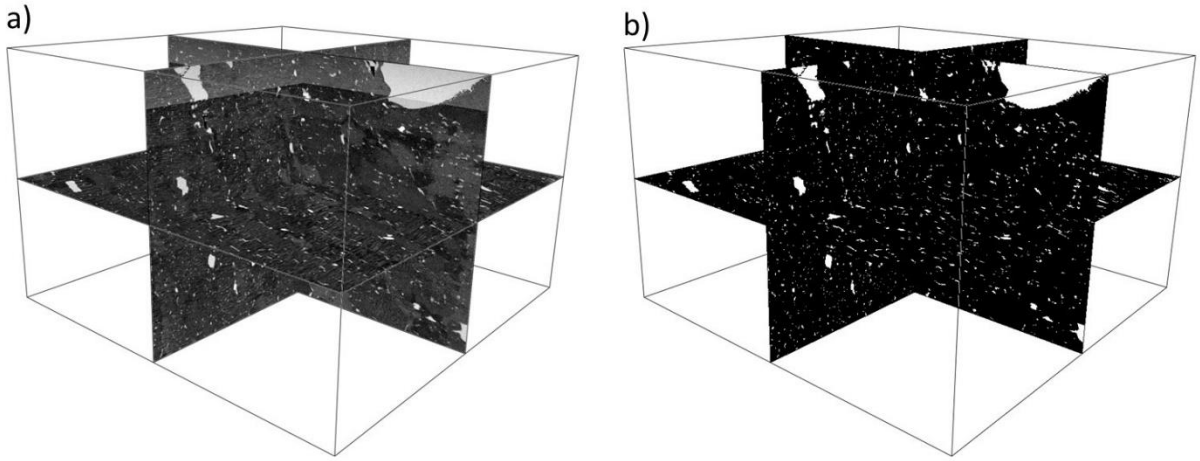

Figure 32: Visualization of the data with *ortho slice*: (a) BSE images as recorded, (b) fully segmented images. (box size: 31x31x20 µm^3)

With the segmented images a 3D reconstruction of the precipitates was rendered with *Avizo 9.0*. The rendered volume is shown in Figure 33. For this reconstruction only 400 slices (which results in a volume of 31x31x20 µm^3) were used, because a larger number of slices

makes the 3D reconstruction overloaded with small features. With this figure the different sizes of the precipitates are well visualized. An educated guess is that the composition of the very large precipitates differs from the composition of the small dispersed ones. To prove this assumption *3D elemental mapping* (or at least EDX analysis at some slices) is needed.

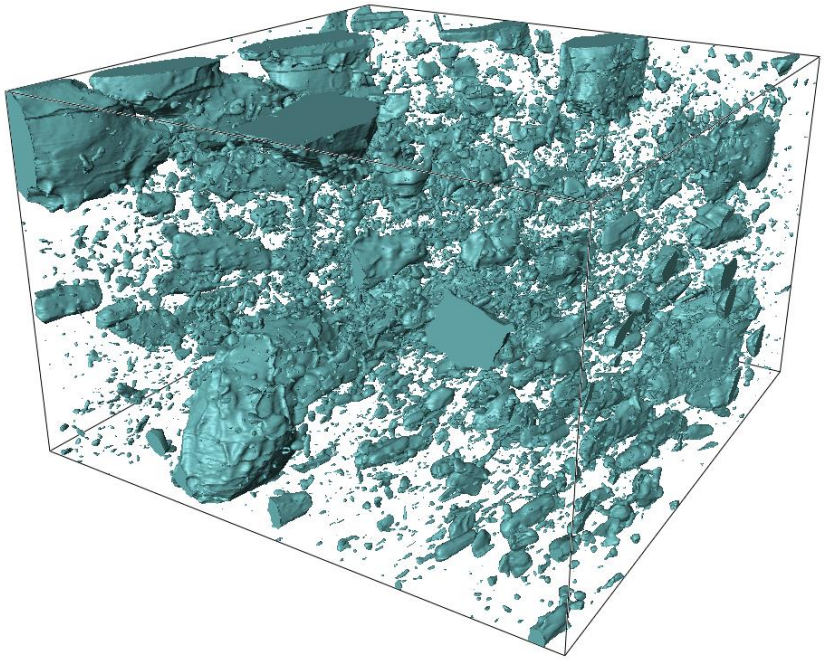

Figure 33: 3D reconstruction of the precipitates in aluminum (box size: 31x31x20 µm^3)

With a software like *Avizo 9.0* it is possible to further evaluate the 3D data. An example is the visual separation of large precipitates from small precipitates. Since the scope of this thesis is in the methodic part these further evaluations were not performed.

5.4 *3D Elemental Mapping* – Results

Before the actual experiment several tests were performed for determining the best parameters for spectrum imaging acquisition. As mentioned in the instrumentation section the working distance needed for a *3View* investigation is not optimal for EDX measurements with the new detector. A high enough count rate was achieved by using large apertures (for increasing the electron current) and by tuning the electron beam (performing a lens alignment for the investigation voltage and usage of a high spot size) to increase the beam current even more. For the actual measurement a 100 µm aperture was used. With the tuning of the electron beam a count rate of 100,000 counts per second (cps) could be achieved. This count rate enables spectrum image acquisition in 10 minutes. The drawback of the large apertures and the high spot size is a bad image quality, because a sufficient astigmatism correction is not possible anymore. Figure 34 shows a BSE image (acquired with the special BSE detector holder during the experiment) of the sample with the mapping parameters (100 µm aperture, spot size 5.9, HV = 5 kV). The contrast between matrix and precipitates is good, but the details and borders are rather blurry.

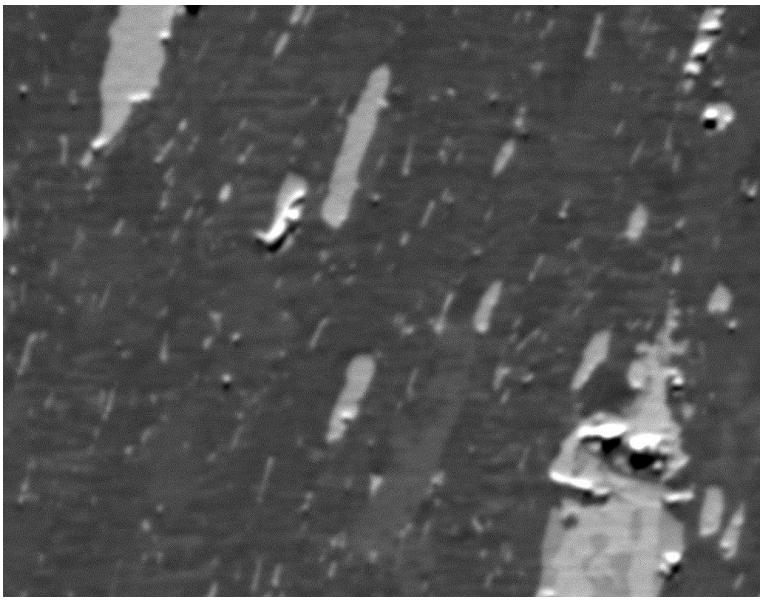

Figure 34: BSE image of the aluminum sample with mapping parameters (HV = 5 kV, image width = 20 µm, special BSE detector holder)

Images with this quality are not directly usable for a morphological 3D reconstruction, but they can help to evaluate the spectrum images (the positions of precipitates are determined). After the pretesting the acquisition parameters for the spectrum images were specified to:

- Lateral resolution: 70 nm/px
- High voltage: 5 kV
- Dwell time: 2 ms/px (for each spectrum image 5 frames were recorded and summed up)
- WD: 7.1 mm
- Pixel resolution: 256x200 px
- 100 µm aperture and spot size 5.9 (adjusted to reach a count rate of ~100,000 cps)
- Preselected elements: Mg, Al, Si, Mn, Fe, Cu

Due to the X-ray generation depth (see Figure 23a) at the used high voltage a slice thickness of 100 nm (this is the largest slice thickness of *3View*) was chosen for the measurement. This leads to a voxel size of 70x70x100 nm^3. The experiment in this thesis was performed manually. This means every cut, BSE imaging and spectrum image acquisition needed manual input. In Figure 35 pixel spectra of several positions within the block-face of the first slice are shown (pixel spectra are saved in the spectrum image). All spectra show a significant SNR for distinguishing the peaks from the background. Problematic is the small energy difference of the Fe L line (705 eV) and the Mn L line (637 eV). A clear peak separation for those lines is not possible, but different pixel spectra of the large precipitate (contains Fe and Mn) on the right show a changed shape of the summed Mn-Fe peaks (the maximum value of the peak is shifted in energy). This precipitate shows also an internal material contrast (see Figure 34) which indicates that it is composed of two different phases.

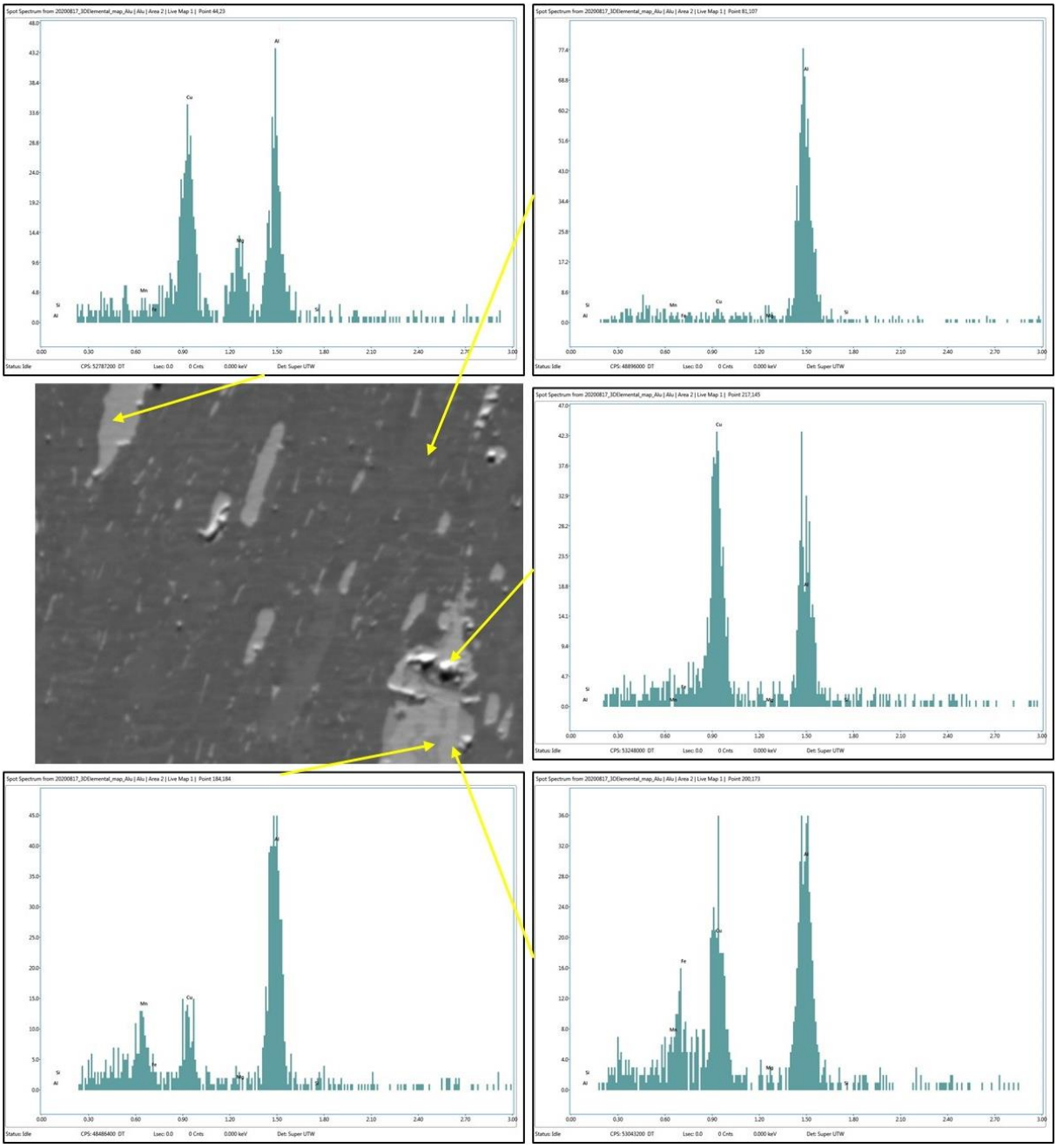

Figure 35: Some selected point spectra of the block-face after the first slice (image width = 20 µm)

Due to the comparatively long recording time of 10 minutes and the necessity to perform all actions manually only the block-faces of 100 slices were recorded. The overall investigated volume was 20x20x10 µm^3. For further evaluation a quantification of the spectrum images was needed. During this process problems arose which are described in the next section.

5.4.1 Quantification Problem Using the L lines

During the preliminary testing the problems of the quantification process were discovered. With the *APEX 1.0* software from *EDAX* there are errors in terms of L line quantification. For some elements the quantification result is far too low compared to the nominal ones (this was tested with EDX standard samples). For K lines the quantification works reliably. Additionally, there was a software bug, which made iron L line quantification impossible (the result was

every time 0% even for standard samples with a large percentage of iron). This bug could be fixed with an update of the software to version 1.5.

For the quantification of spectrum images, the *APEX* software provides ZAF correction. The results of the quantification in atomic percent for each element are shown in Figure 36.

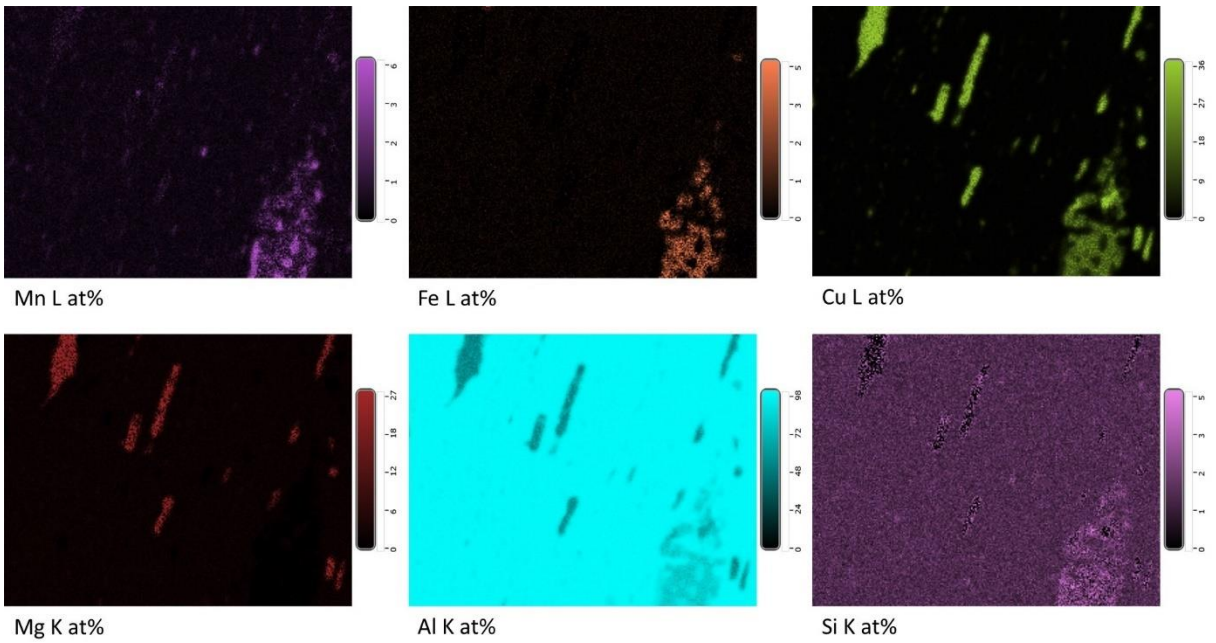

Figure 36: Results of the quantification (ZAF correction) of the spectrum image (block-face after slice 1) in atomic percent

In Al 2024 several different precipitates form (this can be verified by the different EDX spectra at different spots). In literature (Shabestari et al., 2014) the following possible precipitates are listed: $Al_{15}(CuFeMn)_3Si_2$, $Al_{20}Cu_2Mn_3$ (the so-called T-phase), Al_2Cu, Mg_2Si, Al_2CuMg, $Al_{12}(FeMn)_3Si_2$, Al_7Cu_2Fe and $Al_6(FeCu)$. Important to note is that it will be not possible to detect all possible precipitates with SEM EDX, because the lateral resolution is limited, and some precipitates are very small (~50 nm). By comparing the theoretic atomic percents with the measured ones, it becomes clear that the results for manganese and iron are too low (around a factor of 2). The lowest stoichiometric (in the precipitate phases given above) atomic percent of iron is 10 at% compared to measured 5 at%. In the case of manganese the situation is the same. The most probable explanation for this behavior are the quantification problems of the software with L-lines.

To test the quality of the spectrum images they were also quantified in the EDAX Genesis software. The *EDAX Genesis* software is an older EDX acquisition and analysis software from *EDAX*. It is possible to load spectrum images recorded with the *EDAX APEX* software into the *EDAX Genesis* software without losing information (both programs use the same file format). Even, in this software the quantification results of the spectrum images were deviating from the nominal values. Especially the results for manganese and iron were far too low.

One feature of spectrum images is the possibility to sum all pixel spectra of a defined region into one spectrum (areal spectrum) to improve the signal to noise ratio. This procedure was used to generate areal spectra of all visible phases. With the *EDAX Genesis* software it was

possible to quantify the areal spectra (with the *APEX software* this task did lead to results which were strongly deviating from the nominal ones). The results are shown in Figure 37. These results deviate a little bit from the nominal ones, but this can be explained by the interaction volume which is unfortunately larger than the voxel size.

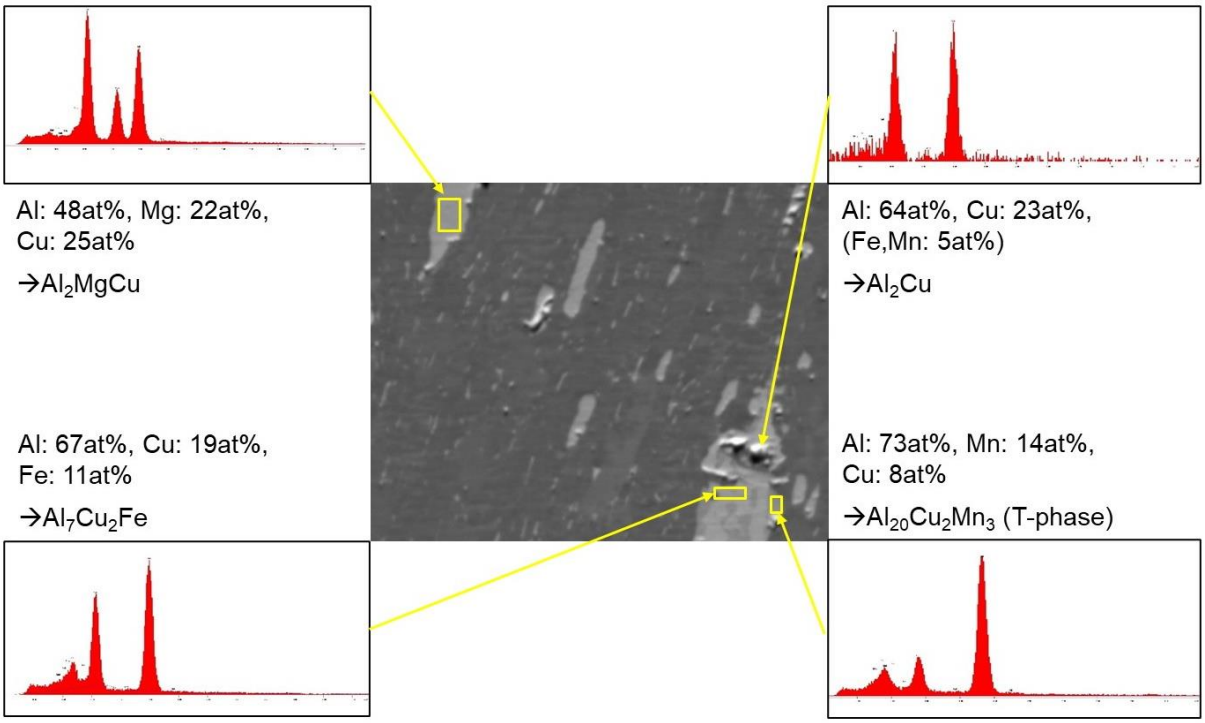

Figure 37: Quantification results of the areal spectra (performed with *EDAX Genesis*)

Longer measurement times did not improve the quantification of the spectrum images. Concentration values for iron and manganese were still far too low.

5.4.2 3D Reconstruction of the Spectrum Images

The evaluation of the quantified maps was performed in *MATLAB*. With simple concentration ranges the precipitate type (or Al matrix) can be calculated in each pixel. Therefore, logical operations were applied on the concentration matrices of each element (the csv file generated by *EDAX APEX* is imported as matrix). Then concentration ranges of all known precipitates are applied on the concentration matrices and connected with logical operations. For the Al_2Cu precipitate for example a concentration range of 64-70 at% for Al and 30-36 at% for Cu are used. These ranges are applied on the concentration matrix for Al and Cu to generate a logical array for each element (*true* if the concentration value in one pixel lies in the defined range). The two logical arrays for Al and Cu are then connected by a logical conjunction (*and*) to generate a logical array for the Al_2Cu precipitate. To prepare the results for 3D reconstruction each precipitate is given a value and a matrix with all values is generated (the matrices for each precipitate are summed into one matrix). This matrix is then transformed and saved as grayscale image.

Due to the bad results in the quantification process (see the preceding section) it was only possible to detect two precipitate phases definitely and a region with a mixture of several precipitate phases. The Al_2MgCu precipitate phase (it is the only phase which contains

magnesium and aluminum) and the Al_2Cu phase could be identified definitely. The manganese and iron containing pixels could only be mapped in a region with mixed precipitates. Figure 38 shows such a grayscale image. The image quality is not that good, but the noise can be reduced with *Avizo 9* before rendering of the precipitate volumes.

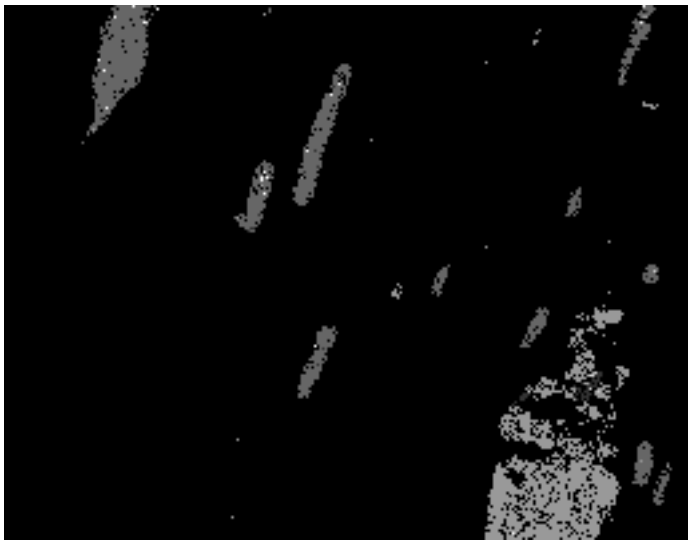

Figure 38: Grayscale image of the precipitate type and position (image width: 20 µm)

With such grayscale images, the 3D reconstruction was performed in *Avizo 9*. Figure 39 shows the result of the reconstruction in two angles. The morphology of the Al_2MgCu phase is well presented, the Al_2Cu phase was found in one spot and for the remaining detected precipitate phases (Al_7Cu_2Fe and $Al_{20}Cu_2Mn_3$) little information could be derived. It was not possible to separate those phases. Therefore a combined volume of the two precipitate volume is shown.

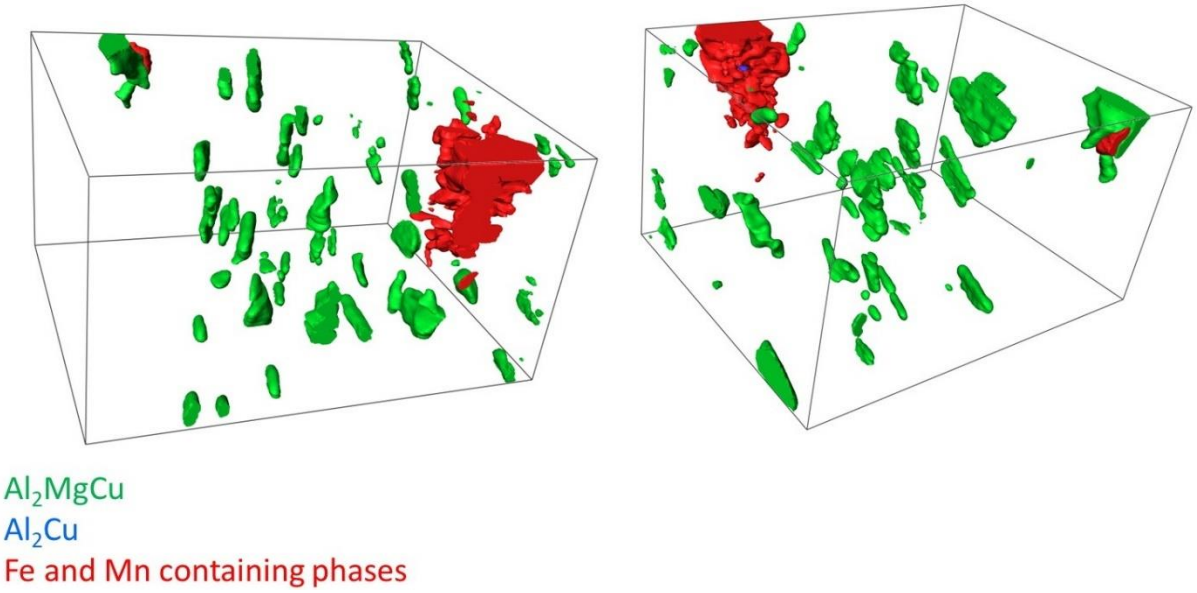

Figure 39: 3D reconstruction of the precipitate phases shown from two angles. (box size: 19x15x10 µm³)

5.5 *3D Elemental Mapping* – Conclusion

The previous sections show very clearly that *3D elemental mapping* works only to a limited extent with the available instrumentation. It is possible to record elemental maps, but the quantification results are very poor. Very problematic is the high electron current in order to achieve sufficient count rates due to the unfavorable working distance of *3View* investigations. With a high electron current during *3D elemental mapping* the image quality is bad, because the large used aperture prevents a proper alignment of the electron optics (the image is affected by strong astigmatism). Another problem which needs a solution is the shadowing of the EDX by the BSE detectors. For recording of BSE images during the experiments a special holder for one of the BSE detectors was developed. Automation of the process is possible with tools like *AutoIt* but was not applied.

In comparison to the results of the *3D elemental mapping* in (Zankel et al., 2011), which was performed with the same microscope and sample (Al 2024), but with a different EDX detector (*X-Max* Silicon Drift Detector (SDD) from *Oxford Instruments* with an 80 mm^2 detector area) the results are worse, because of the not functionating software routine for quantifying L-lines. Most of the precipitate phases, which were found in the previously test, could not be reconstructed with this test. Figure 40 shows the result of the previous performed experiment. It is obvious that more precipitate phases could be successfully identified and reconstructed. Only for the major phase the results were similar. Important to note is, that the volume of the first test is even larger.

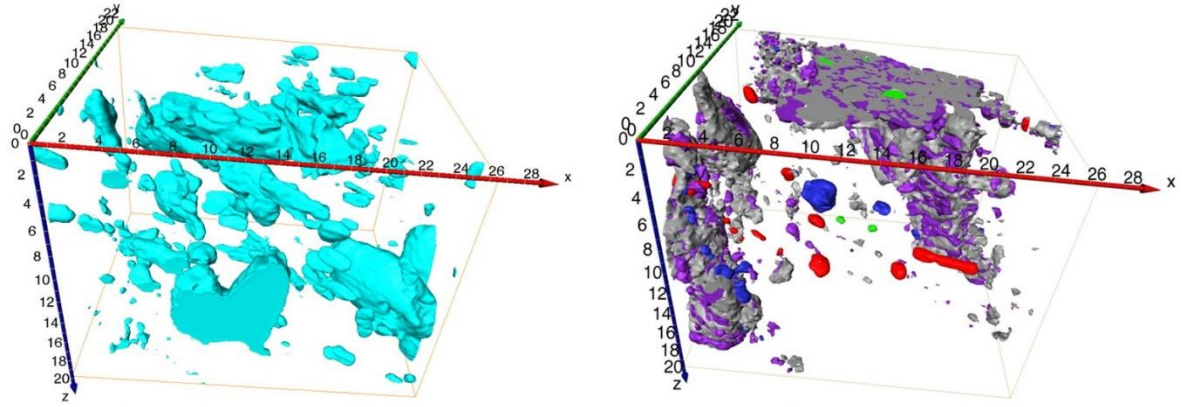

Figure 40: Reconstruction of the precipitate phases of the aluminum sample from (Zankel et al., 2011)

6 Combining *3View* with Raman Spectroscopy

Raman spectroscopy is a commonly used technique to get deeper insight into the chemistry of a material. A simple example for such a material, where Raman spectroscopy can be a good addition to conventional SEM investigations, are polymer composites. In many cases the BSE contrast of two polymers is similar (they are not distinguishable by conventional imaging). Standard contrasting of soft matter samples is performed by so-called staining. For this procedure the sample is saturated with a contrast agent (e.g. heavy metal solutions). Different parts of the sample absorb the contrasting agent to a different degree and therefore a contrast via the heavy metals is established.

In recent years the combination of Raman spectroscopy/microscopy and SEM (correlative microscopy) becomes more used. This correlative method is already well established for samples where only one surface is investigated. In the case of 3D investigations also the composition of materials is from interest. The possibility to use Raman spectroscopy during such an investigation would allow new experiments. For a sample with changing composition (e.g. a complex polymer composite) it would be possible to qualitatively assign all phase for fixed numbers of slices. Another possibility would be the determination of a newly appeared phase during a 3D investigation. In this case the cutting could be stopped to perform Raman measurements and subsequently the 3D investigation could be continued. Therefore in this thesis a combination of 3View and Raman microscopy was tested.

6.1 Combining *3View* with Raman Spectroscopy – Measurement Procedure

The main problem (or obstacle) of combining *3View* with Raman spectroscopy is the need for two separate devices. Therefore, a possibility for moving the sample from one device to the other and back has to be found. During this transition it is important, that the ROI is easily findable in both systems. In Figure 41 the workflow of such an investigation is shown.

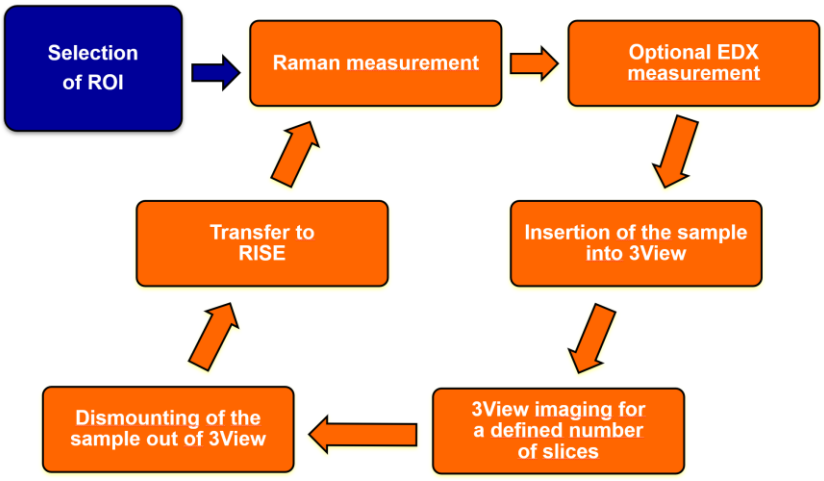

Figure 41: Sketched workflow of the combination of *3View* and Raman

Before starting with the selection of the ROI the first and second step of sample adjustment in *3View* (see chapter 4) has to be performed. Before the switch to the *RISE* system (Raman

imaging and scanning electron microscopy) for the Raman measurement the rotational position of the *3View* holder has to be marked (the marks are highlighted with yellow arrows in Figure 42).

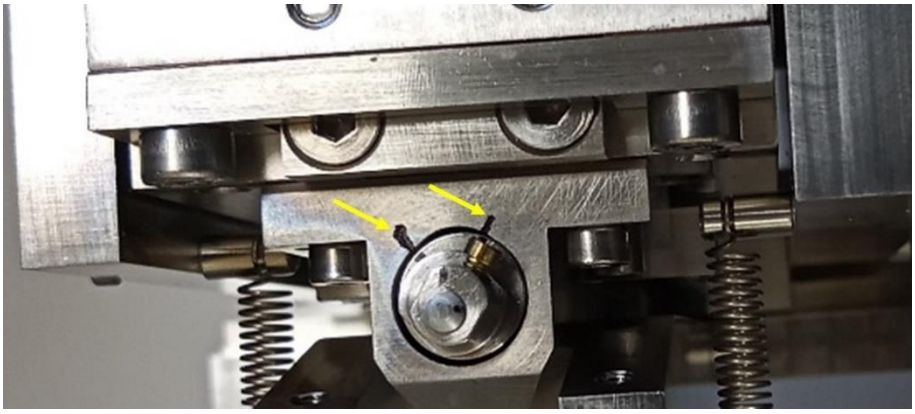

Figure 42: Inserted *3View* sample holder with marks for the rotational adjustment

After selecting the ROI, the sample is transferred to the *RISE* system (a detailed description is in the next section) and first Raman measurements are performed. It is possible to make a Raman mapping or only spot measurements. For positioning the *3View* sample holder (for the transfer the sample needs to stay inserted in the *3View* sample holder in order to preserve the adjustment) in the *RISE* system an aluminum cylinder, where the caliber of an inner cylinder matches with the external diameter of the sample holder, is used. In Figure 43 the *3View* sample holder stabilized with the aluminum cylinder within the *RISE* system is shown.

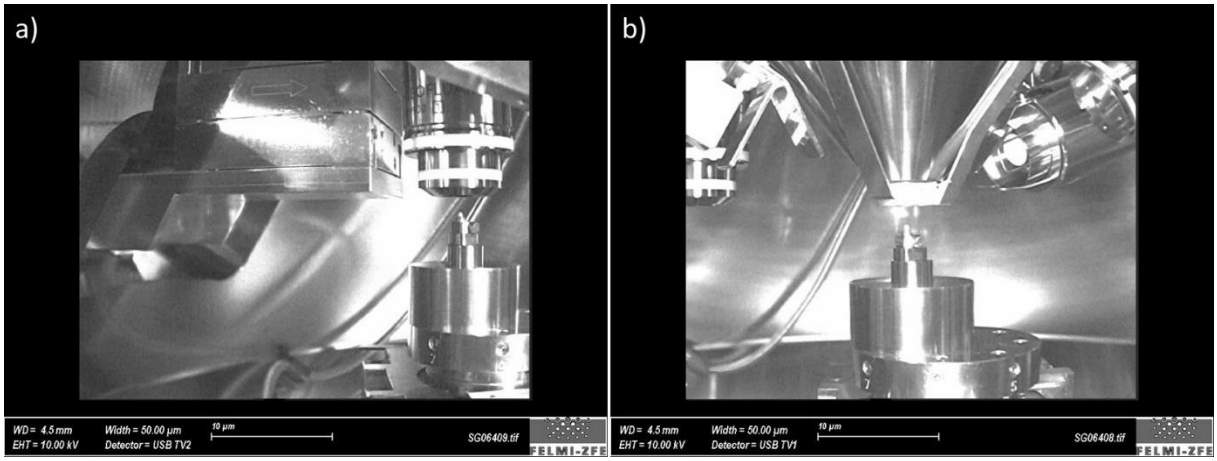

Figure 43: *3View* sample holder with a stabilizing aluminum cylinder in the *RISE* system: (a) Raman position, (b) SEM position

The additional performing of an EDX measurement after the Raman measurements is possible. Due to the need for uncoated samples during Raman measurements the EDX measurements can only be performed in low vacuum (with all complications described in section 2.3.3). Then the sample is moved back to *3View* and the full adjustment procedure is performed again (see chapter 4). The long adjusting times for a sample in 3View are the main drawbacks of this method. After finishing the adjustment, a conventional image series with *3View* is obtained for a desired number of slices. In the next step the sample is dismounted and the circle in the workflow starts again with the transfer to the *RISE* system and the next Raman measurements.

The use of the *RISE* system is important, because the SEM imaging provides a simple retrieval of the ROI. In most cases it would be more difficult to find the ROI with the light microscopic image of a Raman microscope, because SEM images and light microscopic images have commonly very different appearance.

6.1.1 Introduction to the System *RISE*

The combination of Raman microscopy and SEM in the same measurement device is not trivial, because of the different probe types which are used (SEM uses electrons, Raman uses light). This means that such a device needs an electron optical system and a light optical system. *Raman Imaging and Scanning Electron microscopy (RISE)* is a combination of a *Zeiss SEM Sigma 300 VP* from *Carl Zeiss AG* (Oberkochen, Germany) and a Raman microscope from *WITec GmbH* (Ulm, Germany). The basic working principle is sketched in Figure 44.

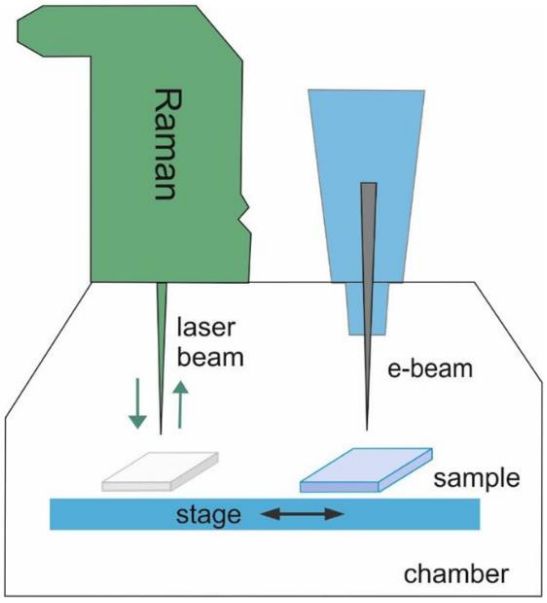

Figure 44: Schematic working principle of the *RISE* system (Schmidt et al., 2019)

The objective of the Raman microscope and the electron optics are located at different positions in the chamber. For investigation and selection of a ROI all standard signals of an SEM can be used. After this step the stage moves the sample in an automated manner below the objective of the Raman microscope (the stage needs to be very precise) and the Raman measurements can be performed. Then the stage can be moved back to the SEM position to perform EDX measurements or acquire additional images.

6.2 Combining *3View* with Raman Spectroscopy – Sample

A suitable test sample for the combination of *3View* and *RISE* needs some specific properties: in SEM the sample should have intrinsic material contrast, there should be different materials of Raman interest and the sample needs to be sliceable. In a first test two paper samples with a chitosan layer on the surface were investigated (one with recycled paper). Unfortunately, the layer was not visible in the SEM (no contrast). Even, with Raman measurements the chitosan layer was not detectable. In a second test a special high-quality paper with an internal

layered structure was investigated. The BSE image of the sample is shown in Figure 45. In this image several interesting regions are marked. The arrows 1 mark two regions with a similar grayscale (the Z-contrast in these regions is more or less the same). One can argue that due to the different morphological appearance two different materials are present. With Raman spectroscopy this can be validated.

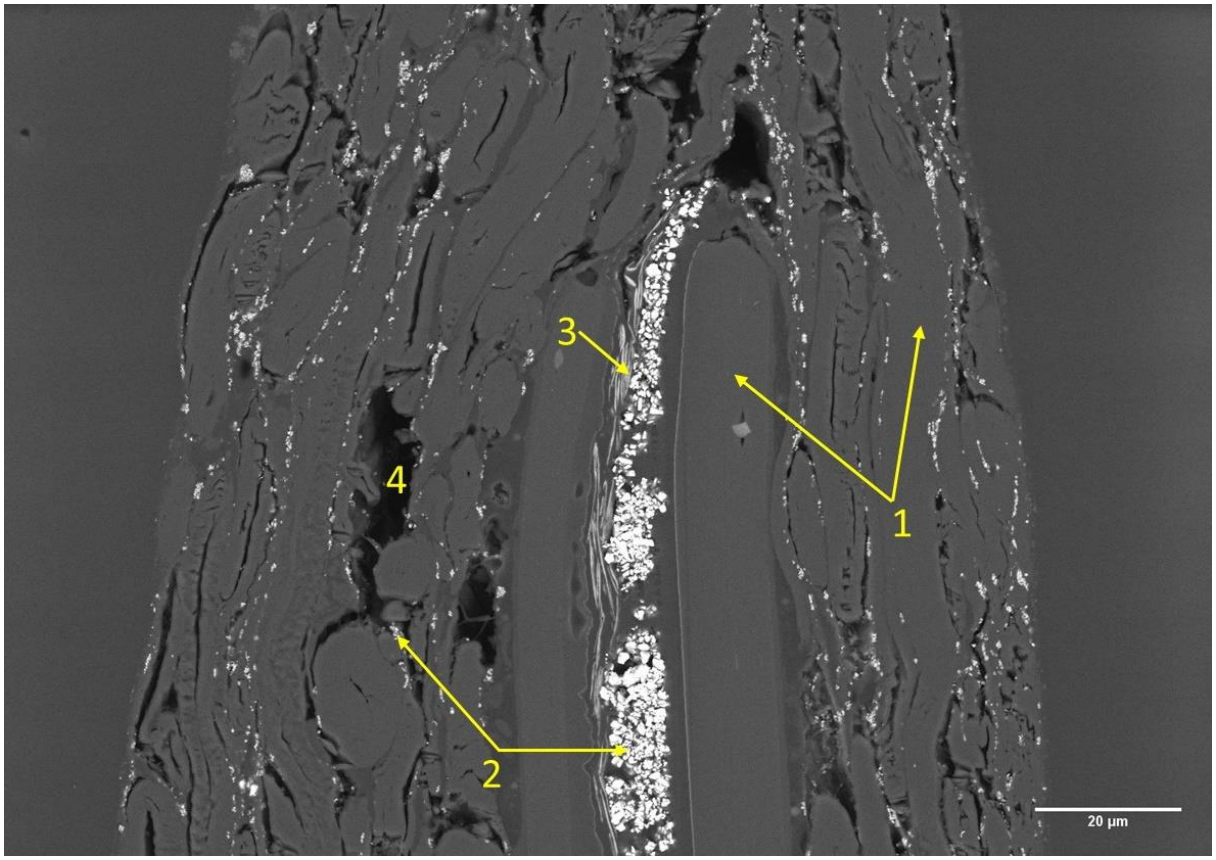

Figure 45: BSE image of the special paper sample (digitally enhanced contrast)

There are two different types of filler materials marked with arrows 2. The filler material in the middle has larger grains and is brighter (higher Z). With Raman spectroscopy it would be possible to determine the material. The arrow at position 3 marks a special phase composed of small features and position 4 marks a void within the sample.

With this sample all three requirements are fulfilled. The sample has intrinsic contrast in the SEM, is sliceable and there are different phases, which can be identified by Raman measurements.

6.3 Combining *3View* with Raman Spectroscopy – Results

For this test the measurement procedure explained in section 6.1 was applied. The Raman measurements were performed before serial sectioning and then repeated every 200 slices (with a slice thickness of 100 nm). For this test experiment only Raman spot measurements on several different phases were conducted. In total the measurement cycle (see Figure 41) for combining *3View* and Raman spectroscopy was performed five times. This means on total

1000 slices were cut and the adjustment process of a sample into *3View* had to be performed six times. For better visualization of the experiment process, a schematic is shown in Figure 46.

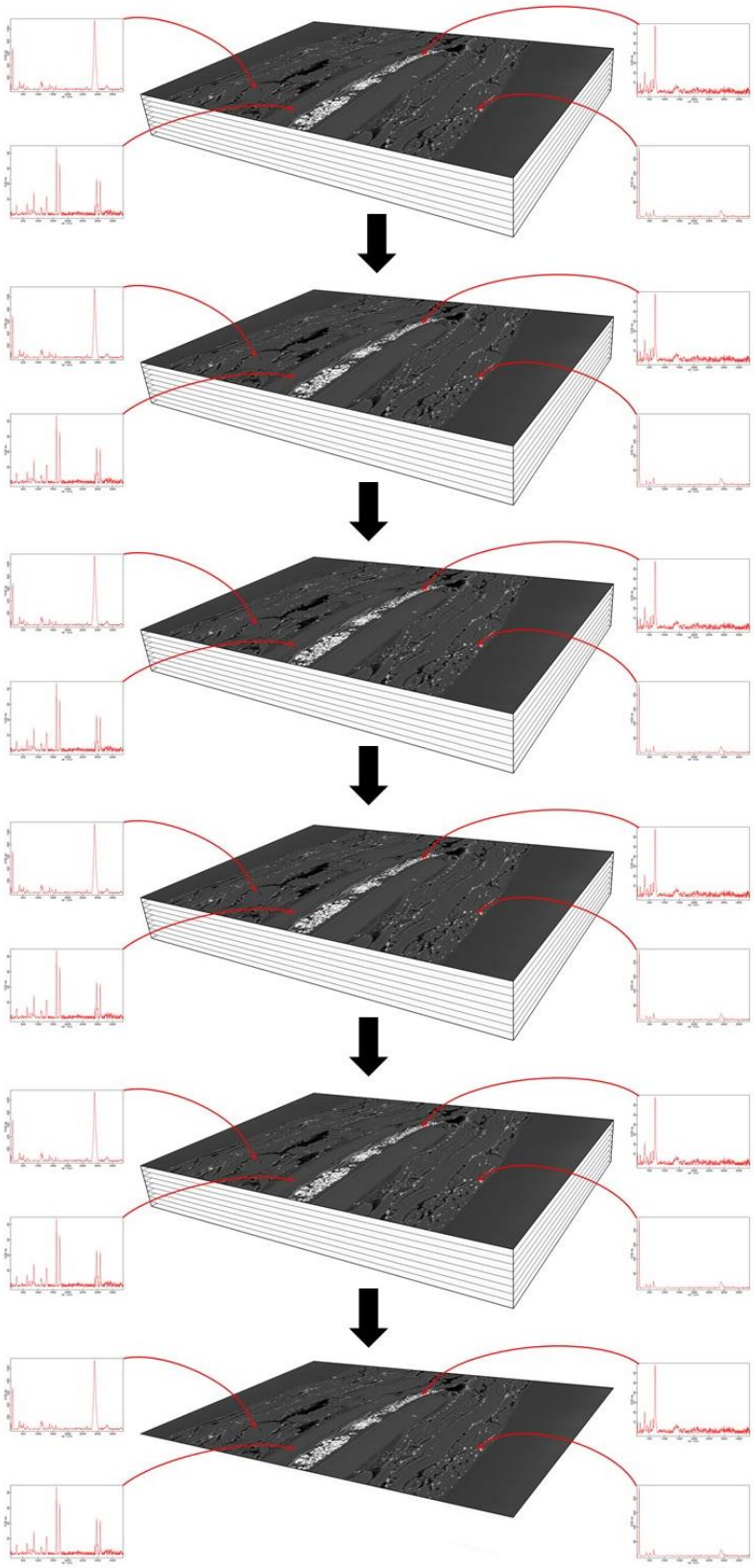

Figure 46: Schematic of the experiment process: each block represents 200 slices performed with *3View* (image and the spectra are symbolic)

The used imaging parameters in *3View* were:

- Lateral resolution: 100 nm/px
- High voltage: 10 kV
- Pixel dwell time: 30 µs
- WD: 7.2 mm
- Chamber pressure: 80 Pa (imaging gas: H_2O)
- Pixel resolution: 1700x1200 px

In total a sample volume of 170x120x100 μm^3 was investigated. The transfer from *3View* to *RISE* and back and the rotational adjustment with the marks worked well. During the sectioning of the sample breakouts of cellulose fibers have occurred in some places. In Figure 47 this artifact is shown for two following slices. These breakouts can be problematic for sample stability.

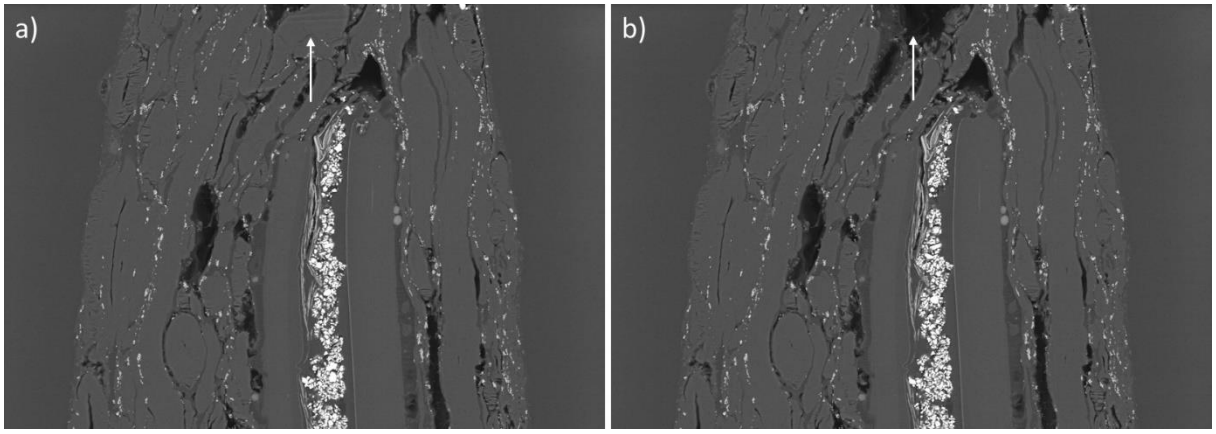

Figure 47: Breakout of cellulose fibers (position marked with the white arrow): (a) slice 102, (b) slice 103. (image width: 170 µm, BSE detector)

Before the first serial sectioning, Raman spot measurements on the sample were performed. Some parts of the sample, especially the filler material in the middle, were relatively sensitive to beam damage induced by the laser of the Raman microscope. In Figure 48 the stitched LIMI image of the ROI is shown. This image is stitched (composed of several individual images) in order to enlarge the field of view, because the objective of the Raman microscope has a much smaller field of view. For the stitching process it can be moved by the help of a piezo crystal.

By comparing it to the BSE image of the SEM (Figure 45) it is clear, that the materials marked with arrows 1 in Figure 45 are different. The same observation can be made for the materials marked with arrows 2.

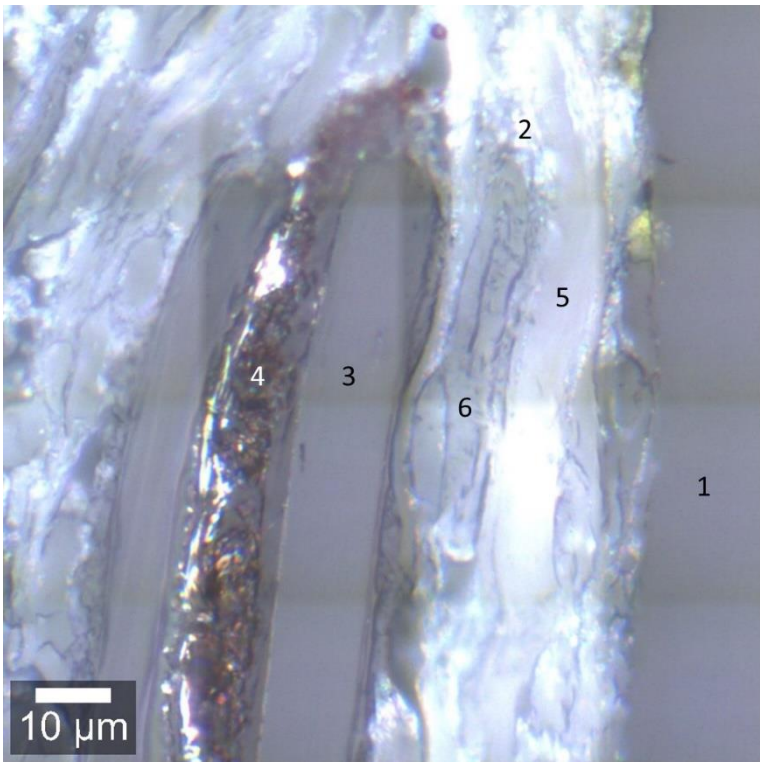

Figure 48: Stitched LIMI image of the sample block face before the Raman measurements before the first serial sectioning. The numbers mark the positions where the Raman spot measurements were performed.

The according spectra (on all spectra a smoothening and a background subtraction was applied) to the marked spots are shown in Figure 49. The according spectrum for the embedding resin was found on position 1. The very bright parts in the LIMI image of the sample (position 2) could be determined as anatase (TiO_2). The long layer marked with 3 was identified as PET. With Raman spectroscopy the brown layer in the middle (position 4) was most likely identified as an iron oxide. For further clarification additional EDX measurements on this phase were performed (Figure 50). Cellulose in this paper has a bright and a darker appearance (position 5 and 6). Raman measurements on the phase (small features marked with arrow 3 in Figure 45) left to the iron oxide were unfortunately not successful (beam damage occurred or no signal was detected). For the qualitative identification of the Raman spectra the *KnowItAll* software from *Wiley Science Solutions* was used.

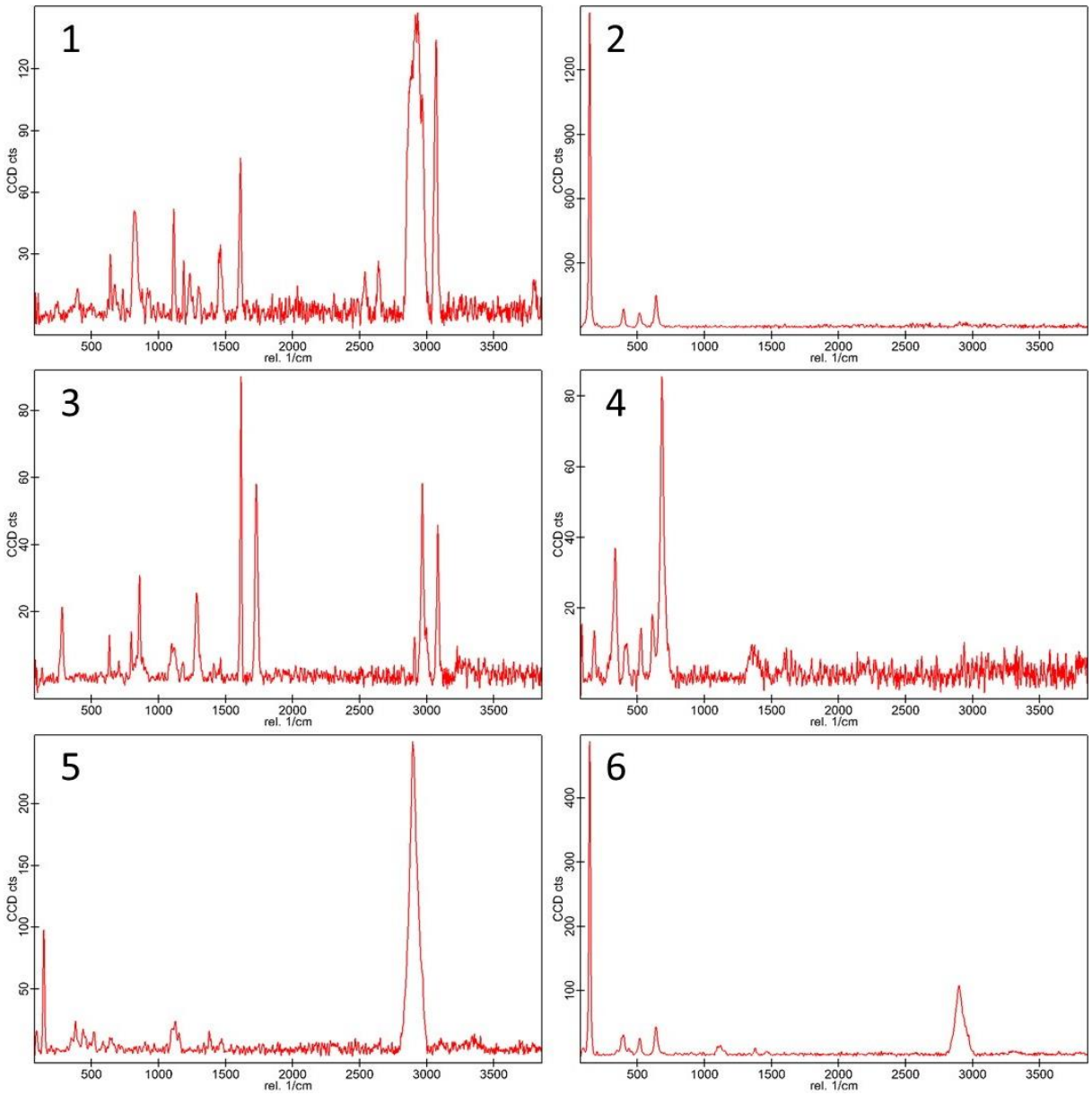

Figure 49: Raman spectra of the marked spots in Figure 48: (1) resin, (2) TiO_2 – anatase, (3) PET, (4) iron oxide (5) cellulose, (6) cellulose

Figure 50 shows the EDX spectrum of the phase at position 4. It is important to note that the measurement was performed in low vacuum (60 Pa) and therefore the skirt effect (see section 2.3.3) has influences the recorded spectrum. In the spectrum the iron, oxygen and carbon peaks are most prominent. Additionally, there are minor peaks of aluminum, titanium and strontium. The aluminum and titanium peaks can be explained by the skirt effect. To explain the strontium peak further experiments are needed. After a quantification of the spectrum iron oxide is the most likely composition of this phase (combined with the information of Raman spectroscopy). The results of this quantification can only give an indication for the real composition, because in low vacuum corrections to the EDX quantification routines (Gauvin, 1999) have to be performed.

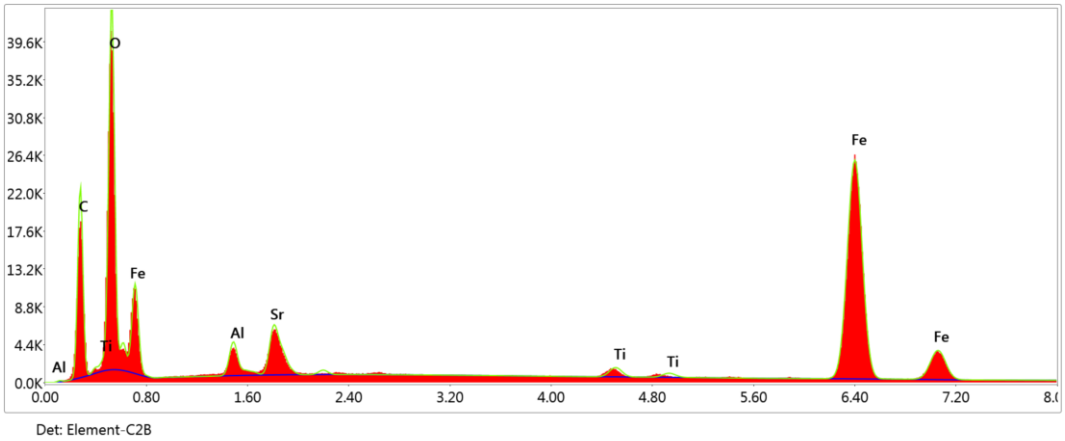

Figure 50: EDX spectrum of the phase at position 4 (Recorded in low vacuum at p = 60 Pa)

The Raman measurements performed after 200 slices show the same materials/phases (there is no significant change in sample morphology). In Figure 51 the stitched LIMI image of the sample after 200 slices is shown. Compared to the LIMI image before cutting most phases are the same (the arrangement is slightly different). The numbers mark again the positions of the Raman spot measurements.

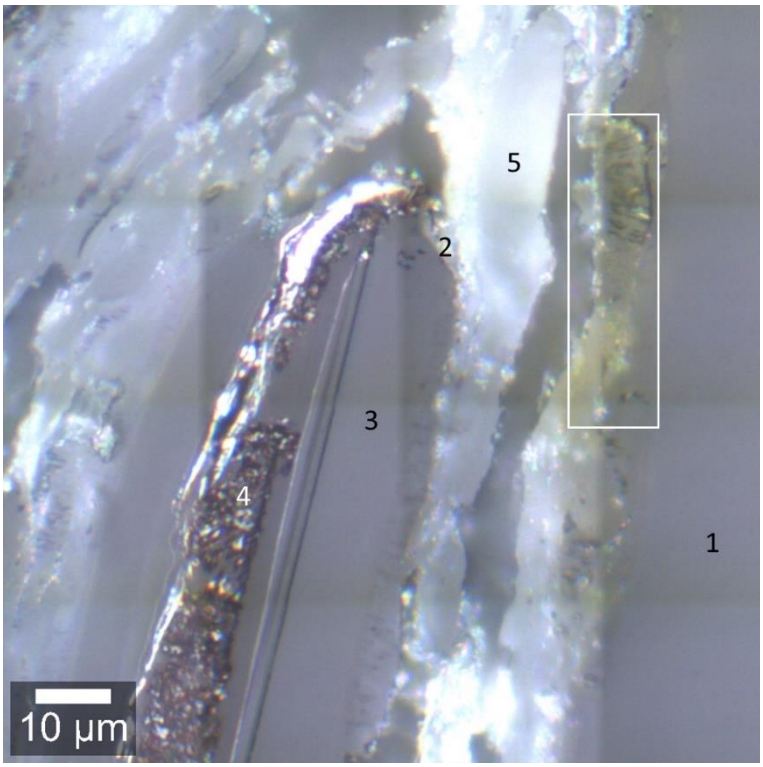

Figure 51: Stitched LIMI image of the sample block-face for the Raman measurements after slice 200. The numbers mark the positions where the spot measurements were performed.

The according spectra are shown in Figure 52. Compared to the spectra before the first serial sectioning all phases could be found again. For the inner filler material, the Raman signal at this spot measurement was much weaker (the peaks are less prominent). For the green area on the right side of the sample (marked with the white rectangle) no spectrum could be acquired, because of fluorescence (at the *RISE* system a 532 nm laser is used). If the energy of the laser photons is in the same range as the electronic states of the investigated materials

(molecules) light gets absorbed. Most of the absorbed light is then emitted with a small wavelength difference (in the range of the wavelength difference of Raman scattering). The probability of fluorescence is much higher than the probability of Raman scattering and therefore the Raman signal is masked by the fluorescence signal.

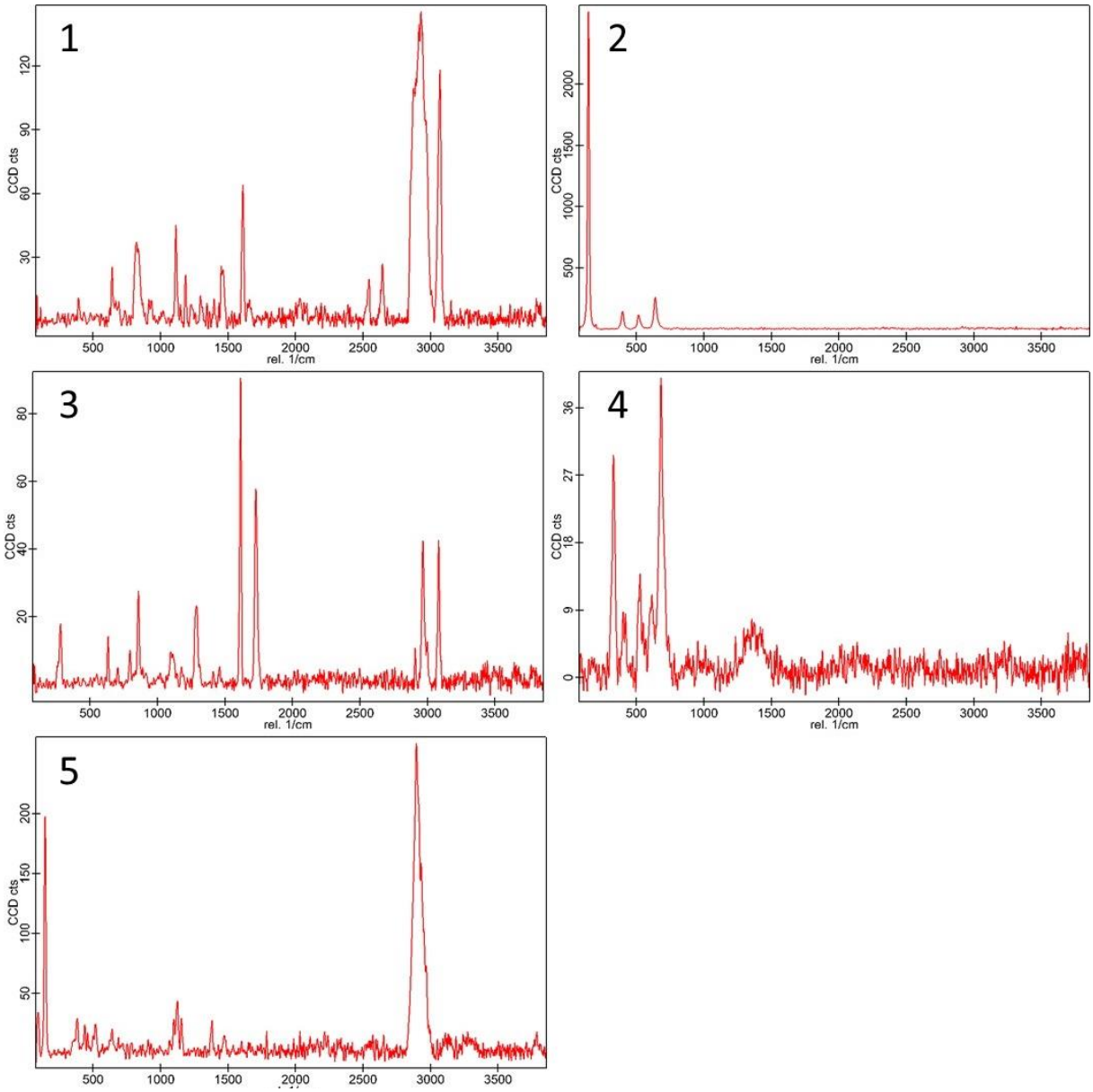

Figure 52: Raman spectra of the marked spots in Figure 51: (1) resin, (2) TiO_2 – anatase, (3) PET, (4) iron oxide (5) cellulose

Due to the same appearance of the sample over the whole depth, the remaining results of the Raman measurements after slice 400, 600, 800 and 1000 are shown in the Appendix (Figure 89-Figure 96). During the Raman measurements only seldomly strong beam damage occurred. In these cases beam damage was extensive and reached a few microns into the sample. Figure 53 shows the extent of beam damage over 55 slices (5.5 µm). For the evaluation of the images such areas with beam damage are an obstacle, but image enhancement can correct these artefacts.

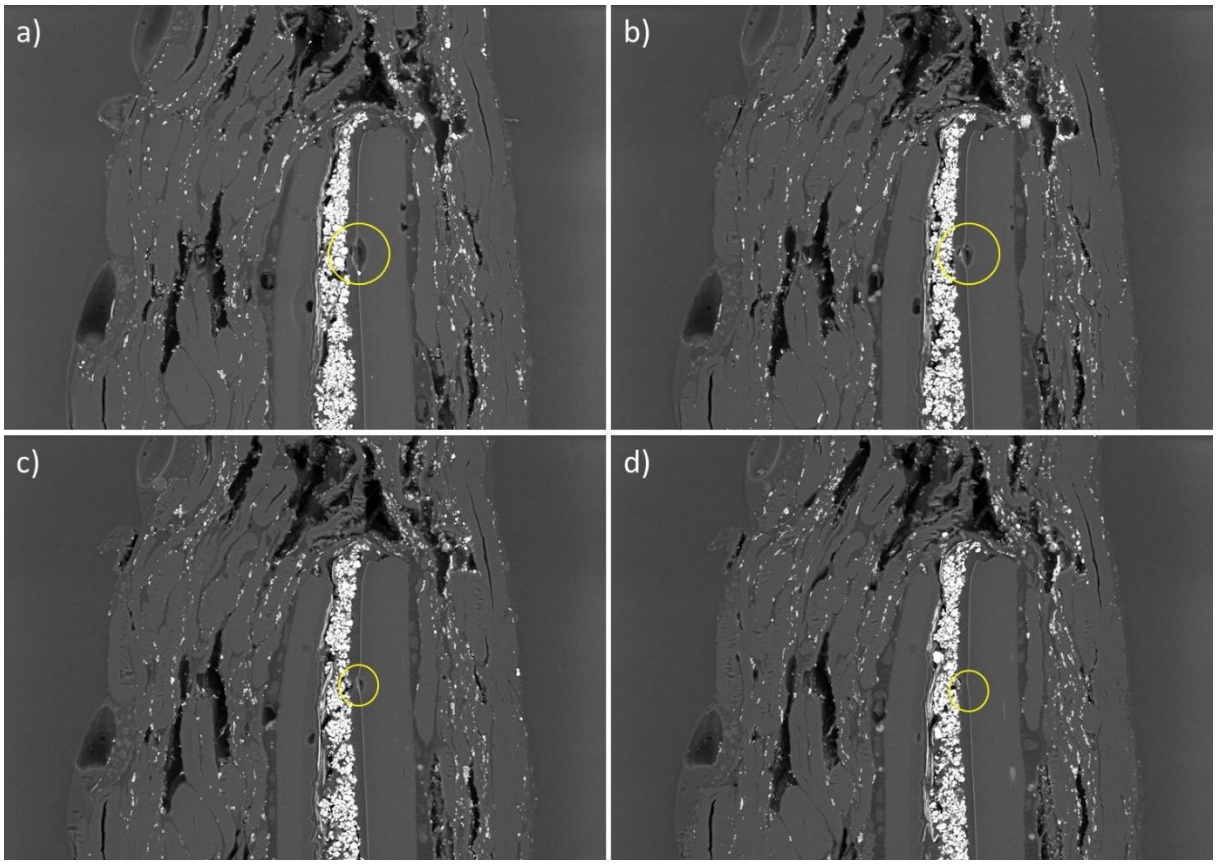

Figure 53: Beam damage after a Raman measurement (marked with yellow circles): (a) slice 201, (b) slice 220, (c) slice 240, slice 255 (contrast and brightness were digitally adjusted for better visibility of the damaged area, image width: 170 µm, BSE detector)

6.3.1 Morphological 3D Reconstruction of the Sample

In Figure 54 a series of BSE images over the whole depth (every 100 slices) is shown. In the images no significant change in the morphology is visible. The sandwich layer of the two PET layers (see the Raman measurements in the previous section), the iron oxide and the uncharacterized phase show only a small change at the top of each image. Most changes occur due to the breakout of cellulose fibers (as described above), but this behavior is an artifact of the cutting process and no interesting morphological feature of the sample. For the evaluation of the images the image enhancement and processing described in chapter 3 was used. The image segmentation of these images in *ilastik* (Berg et al., 2019) delivered results which needed manual improvement. Due to the fact that the volume morphology of the sample is not changing over the depth, it was decided to evaluate only the first 200 slices.

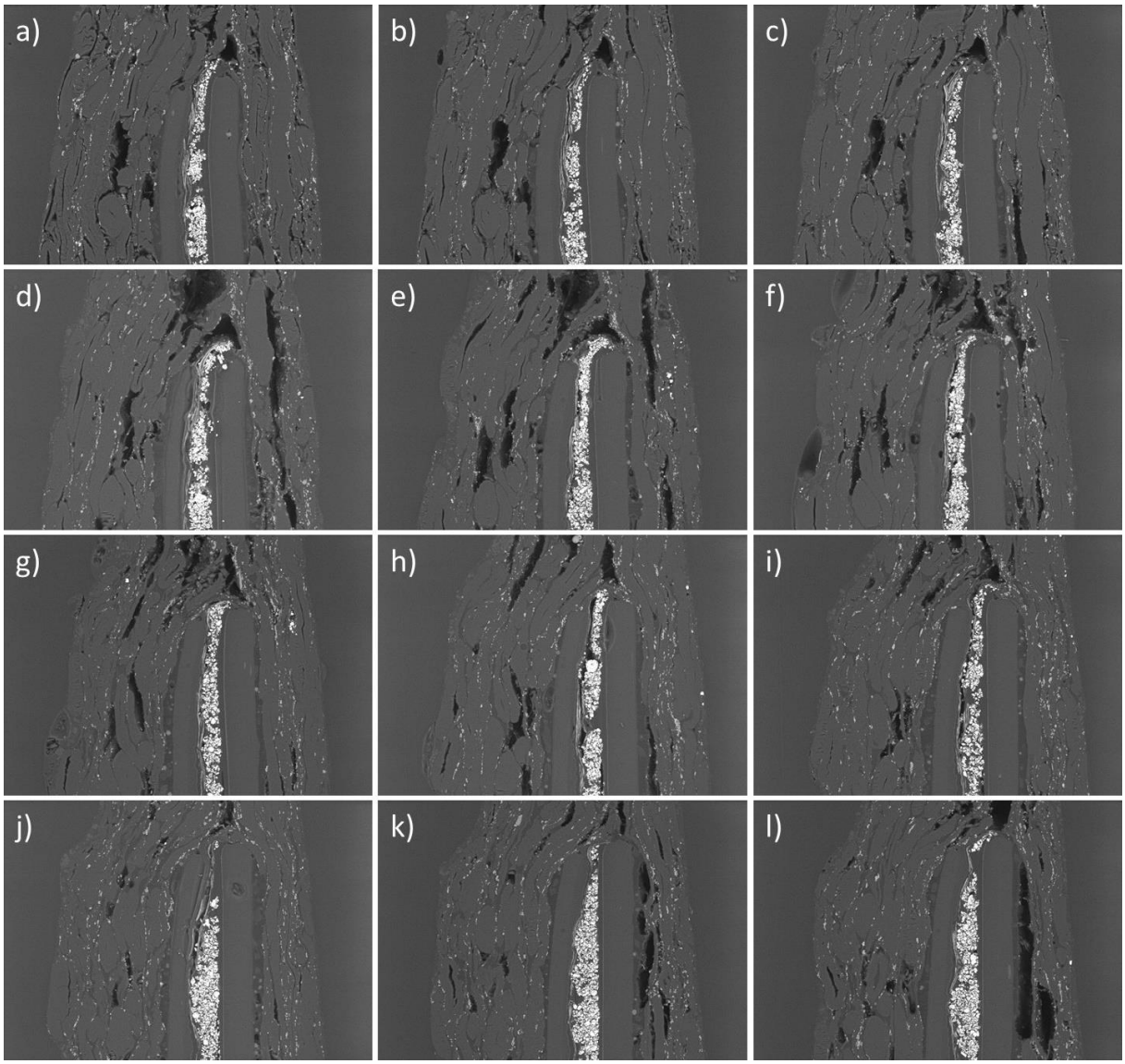

Figure 54: BSE images of the sample at different slice numbers: (a) slice 1, (b) slice 50, (c) slice 100, (d) slice 200, (e) slice 300, (f) slice 400, (g) slice 500, (h) slice 600, (i) slice 700, (j) slice 800, (k) slice 900, (l) slice 1000 (image width: 170 µm, contrast and brightness digitally enhanced)

For faster image segmentation only a smaller region of the recorded images was evaluated for the 3D reconstruction (less pixels mean faster computation time in *ilastik*). The evaluated region is shown in Figure 55.

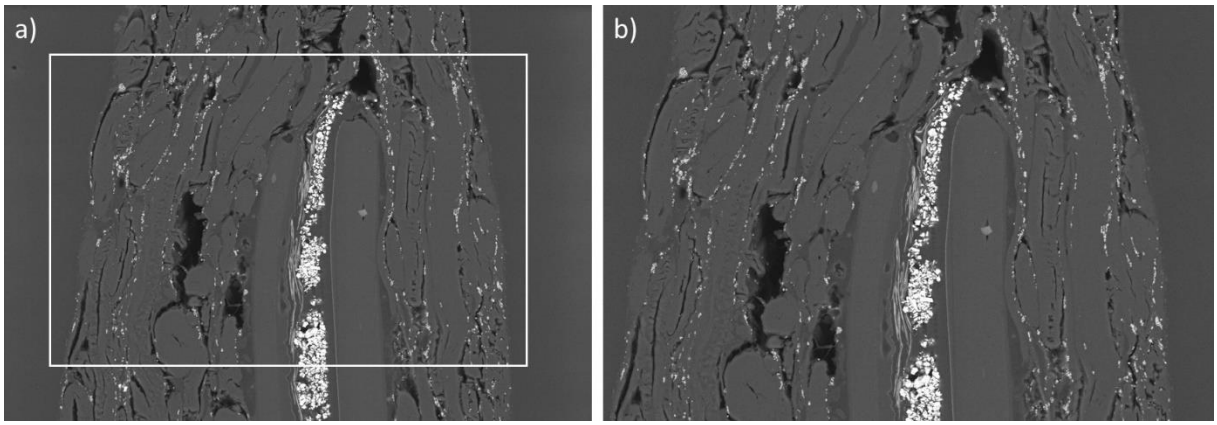

Figure 55: Selected area for image evaluation: (a) whole image (image width: 170 µm) with the marked region, (b) evaluated region (image width: 140 µm)

With image segmentation it was only possible to assign the phases cellulose, filler material, the bright layer in the middle (iron oxide), voids and resin. It was not possible to separate the PET layers from cellulose in *ilastik* (the gray level and shape of both phases are similar). Also, the second layer left to the iron oxide in the middle of the PET layers was not separable from the filler material (TiO_2) during image segmentation. After segmentation with *ilastik* some falsely assigned areas needed to be corrected. Some corrections were performed manually, some with the help of *MATLAB*. The grayscale images after image segmentation are loaded as matrix. For defined regions in the matrix falsely assigned pixel values are changed to the correct ones. After the correction process the improved matrices are saved as grayscale images. For better visualization *ortho slice* images (see Figure 56) of the raw data and the segmentation were generated with *Avizo 9*.

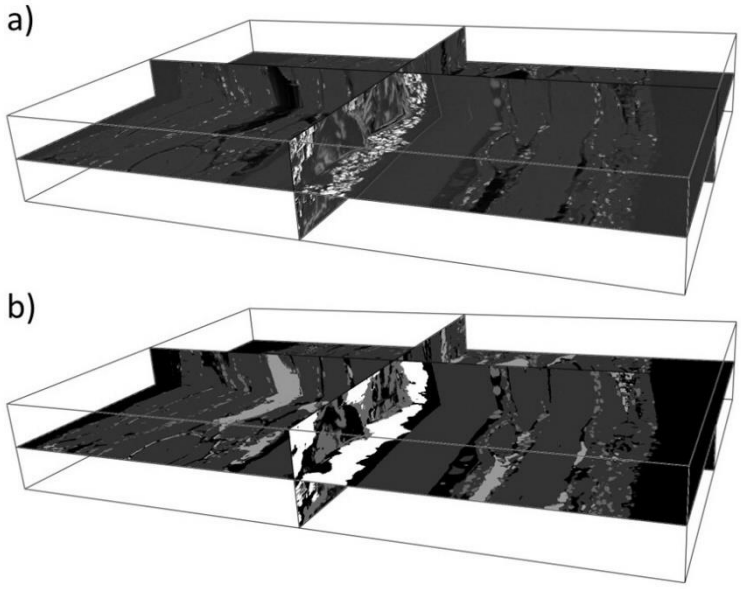

Figure 56: Visualization of the data with *ortho slice*: (a) BSE images as recorded, (b) fully segmented images (box size: 140x95x20 µm³)

In Figure 57 the 3D reconstructions of all phases, which could be segmented, are shown. The renderings were generated with the software *Avizo 9*. In the 3D reconstruction of cellulose, the two PET layers are marked. In the 3D volume the morphological difference of cellulose and the PET layers is much more prominent than in the 2D BSE images. During image

segmentation the phase left to the iron oxide layer and the TiO_2 particles could not be separated. In the 3D representation also, these phases show a morphological difference.

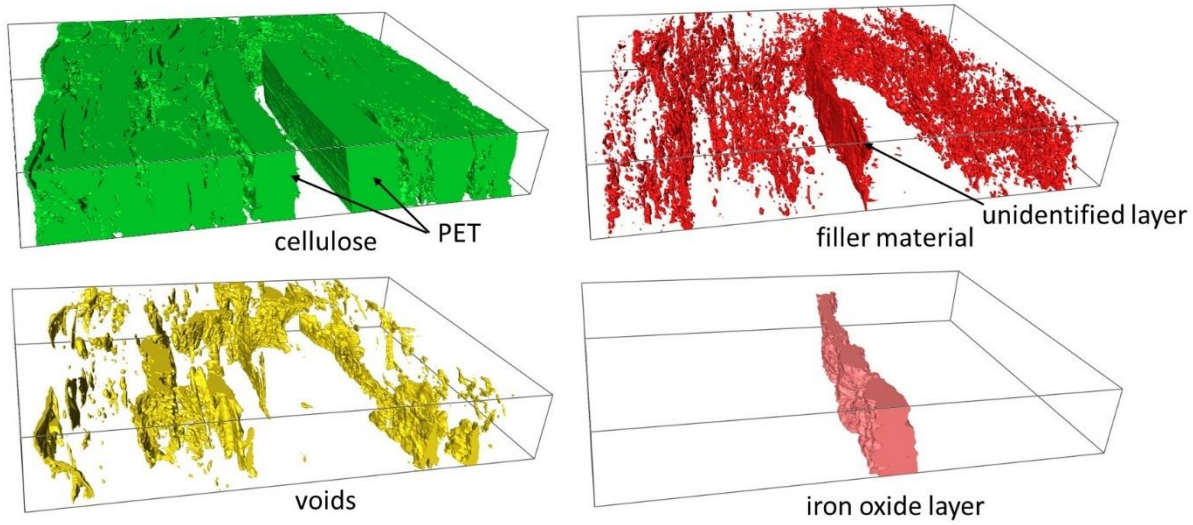

Figure 57: 3D reconstruction of the segmented phases of the sample

6.3.2 Alignment of two Stacks after a Raman Measurement

Due to the need of transferring the sample to another microscope, image stacks before and after the transfer are not already aligned for 3D reconstruction. In a conventional *3View* investigation the images are already aligned after the measurement. The main problem of the alignment of two stacks after the Raman measurements is a small rotation of the following image stack compared to the previous image stack. The offset due to image shift can be easily corrected. The rotational and lateral corrections were made with *FIJI* (Schindelin et al., 2012).

In order to align two consecutive image stacks after a Raman measurement, transformation parameters for one stack have to be determined. For defining these parameters, the function of an overlay can be used in *FIJI*. With this function one image is made semitransparent and used as overlay over the other image (the last image of the image stack before the Raman measurement and the first image of the image stack after the Raman measurement are used). Then only the overlay is moved in x and y direction until both images align. Before the correction of the offset a potential rotational misalignment has to be corrected. To determine the transformation angle iterative testing has to be applied. After determining the parameters, the whole following image stack can be transformed and both stacks align. Until now this process has to be performed manually.

In Figure 58 this procedure is shown. One of two following images is placed (semitransparent) upon the other one and then the alignment procedure was performed. The left white arrow highlights the loss of usable image area due to the rotational alignment (after the rotation the background gets enlarged by the program). The white rectangle marks the usable image area after angle alignment.

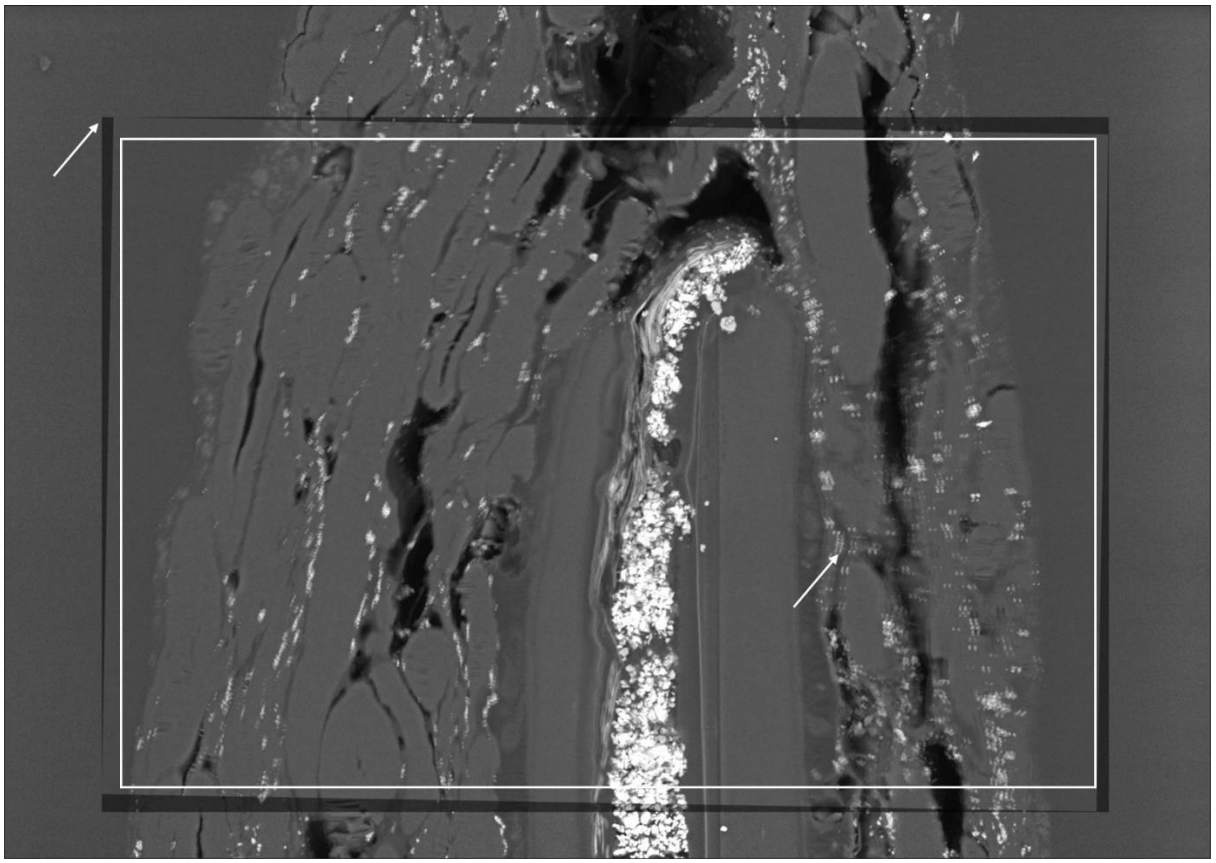

Figure 58: Alignment of two following images (digitally enhanced image, image width: 140 µm)

For this sample it was not possible to align two following stacks perfectly (the right arrow in the image shows an area where the alignment was not perfect). This can be the case due to instabilities during cutting (break out of cellulose).

In general, a better rotational alignment of the sample within *3View* would be preferable to minimize the areas which cannot be used for data evaluation. On the *3View* sample holder a permanent and accurate angle scale could help to find the exact previously used angle after a Raman measurement.

6.3.3 Manual Enhancement of the Image Segmentation

With image segmentation it was not possible to separate the PET layers from cellulose and the fiber layer next to the iron oxide layer between PET layers from the filler material (TiO_2). With the Raman measurements during the 3D investigation with *3View* the different materials could be certainly identified. This information can be used to improve the results of the image segmentation to show the real 3D structure of the sample phases. With *MATLAB* and with manual correction the image segmentation can be modified to include the additional phases in the 3D reconstruction. The grayscale images after image segmentation are imported as matrix into *MATLAB*. Then pixel values of a falsely assigned phase in defined regions are changed to new pixel values. After this process the matrix is saved as grayscale image. All falsely changed pixel values need manual correction. This process was performed to correct 25 slices for demonstration purposes. Figure 59 shows the image segmentation after the application of the *ilastik* software and the corrected version in false color images.

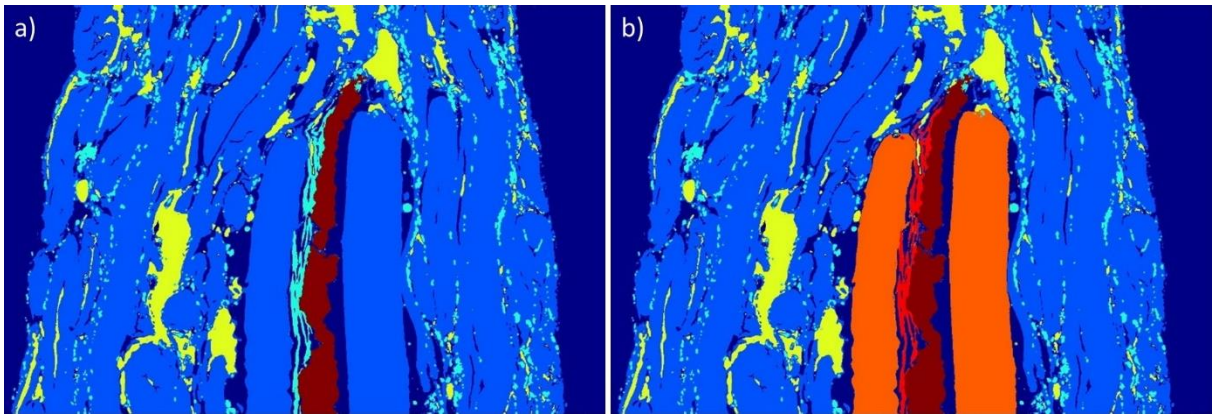

Figure 59: Correction of the image segmentation: (a) image segmentation after the application of the *ilastik* software, (b) image segmentation with the corrections by using the Raman information. (image width: 140 µm)

With the corrected image segmentation data, a new 3D reconstruction was generated in *Avizo 9*. The results are shown in Figure 60.

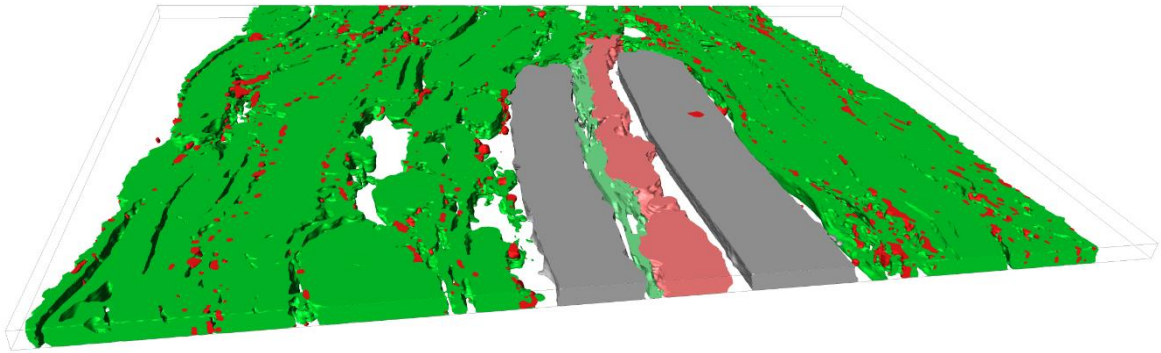

Figure 60: 3D reconstruction of the special paper sample after the correction of the image segmentation. (box size: 140x95x2.5 µm^3)

6.4 Combining *3View* with Raman Spectroscopy – Conclusion

It was possible to establish the first (as to our current knowledge) combination of 3View and Raman spectroscopy. To test this correlative approach firstly an optimization of the sample adjustment in *3View* was performed. The transfer from one microscope to the other one was possible without a large alignment mismatch.

For testing this new combination, a special high-quality paper with an internal layered structure was chosen as sample. In this sample several phases could be identified with Raman spectroscopy. The additional Raman information was used to differentiate between phases which have a similar appearance in the SEM micrographs (a clear differentiation with only the SEM images would not be possible). The Raman measurements after each stack of 200 slices did not provide new information about the sample (the morphology of the sample was not changing much in z-direction), but they proved that it is possible to transfer a sample successfully from *3View* to the *RISE* system and back, which was the aim of this part of the thesis.

A big drawback of this method are the long adjustment times of a sample in *3View*. In order to realize Raman measurements for a larger number of slices the adjustment process needs to be further optimized for a better workflow. Another problem which can occur are samples which are not perfectly stable if they are transferred from vacuum to ambient pressure and back. In this case small changes of the sample dimensions can happen.

The repetition of the experiment with a sample, which has a structure of 3D Raman interest, is planned by the SEM group of the institute. A possible sample with 3D Raman interest needs intrinsic SEM contrast and must be sliceable. Ideally the sample would offer the possibility of Raman mapping (a strong Raman signal would be needed) in a reasonable time.

7 Test of *ATUMtome* and *Atlas 5* for Materials Science Samples

Automated tape-collecting ultramicrotomy is a relatively new technique for 3D investigations within the SEM. In literature this method was only used for the investigation of biological samples. To test the ability of the method in a materials science point of view was the main aim of this part. The possibility to test an *ATUMtome* device and an SEM with the imaging software *Atlas 5* was enabled by the Medical University of Graz.

7.1 Sample

As sample for this test a paper label (beer bottle label) was chosen. The sample was first prepared for conventional ultramicrotomy (the sample gets embedded in resin and is cut to size). A label is in general a paper with a paint layer on one side. In primary examinations the block-face of the ultramicrotomy sample was imaged with SEM to investigate its structure. Figure 61 shows a BSE micrograph imaged in the low vacuum mode (65 Pa). There are three main phases visible on the image: the bright part marked with number 1 is the filler material, the light gray part marked with number 2 is cellulose and the dark gray part marked with number 3 is embedding resin. On the left side a very thin layer (marked with a white arrow) is visible, which is separated from the sample. Most probably this is the paint layer, which got detached during sample preparation. Paper is an ideal sample for SEM investigations because of its intrinsic compositional contrast. Many other sliceable samples need additional staining (contrast enhancement commonly performed with heavy elements) in order to make the different phases visible in the SEM.

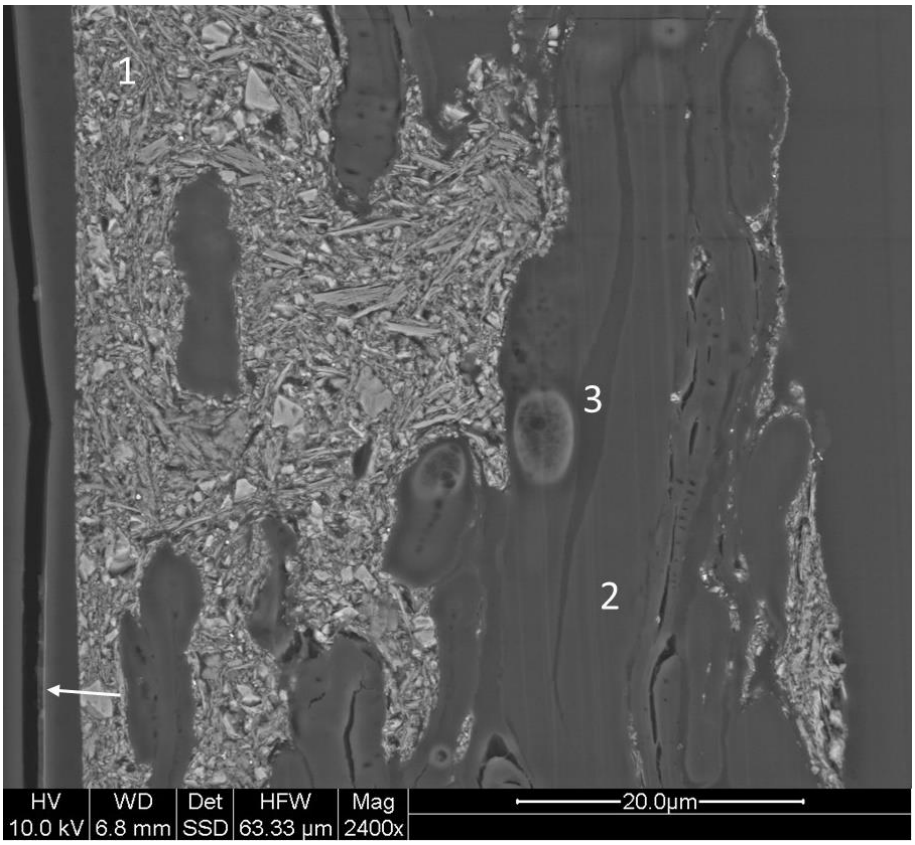

Figure 61: BSE micrograph of the paper label (low vacuum mode p = 65 Pal, imaging gas: H_2O)

This paper sample has a strong similarity to the paper sample presented in (Zankel et al., 2009) which was used for a successful 3D reconstruction with *3View*. The already successful investigation of a similar sample in *3View* makes this sample ideal to test the combination of *ATUMtome* and *Atlas 5* in a materials science point of view.

7.2 Cutting of the Sample with *ATUMtome*

The *ATUMtome* process starts similar to conventional microtomic sample preparation with the insertion of the sample into the microtome. Before the first cutting tests the sample was trimmed to reduce the size of the individual sections (the paper sample has more or less the same structure over the whole length). The cutting surface after trimming was a long rectangle (Figure 62a). Then the actual cutting process could be started. Firstly conventional cuts with the used knife are performed to make the block-face perfectly parallel to the cutting plane. Afterwards the automated tape collecting device is mounted and adjusted with a *Kapton* tape and put into the right position for collecting the sections. For good performance the right adjustment of the tape tension and the right speed of the tape have to be chosen. This adjustment procedure is time consuming, but eliminates problems during the cutting and collecting process.

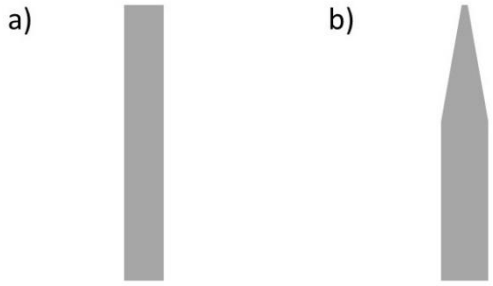

Figure 62: Block-face shapes of the sample used for cutting with *ATUMtome*

A slice thickness of 100 nm was chosen for the first section set. During the collection of this section set it was not possible to run *ATUMtome* automatically (which should be possible in order to collect large section sets). The main problem, which led to a stop after only a few sections, was that some sections did not get collected automatically by the tape (manual manipulation was needed). Manual manipulation in order to collect the sections can introduce damage to some sections and it is also possible to lose some slices. Another problem is the rotation of the sections before collecting on the tape. With the chosen block-face shape it is very hard to align subsequent sections because it is not clear where the top/bottom of the slice is.

Before a second cutting run the block-face geometry was modified to the shape shown in Figure 62b and the tape parameters of *ATUMtome* were slightly altered. With this alteration it was possible to run *ATUMtome* fully automatically for at least 400 sections. The behavior during the cutting process was similar to the manner (up to 4 sections form small ribbons) of trapezoids described in (Baena et al., 2019). After finishing the cutting process, the tape with the sections gets glued onto a silicon wafer (a carbon adhesion tape is used). This wafer is then used for electron microscopical investigations.

The cutting of the sample with *ATUMtome* was performed at the Medical University of Graz. Figure 63 shows some impressions of the *ATUMtome* sessions.

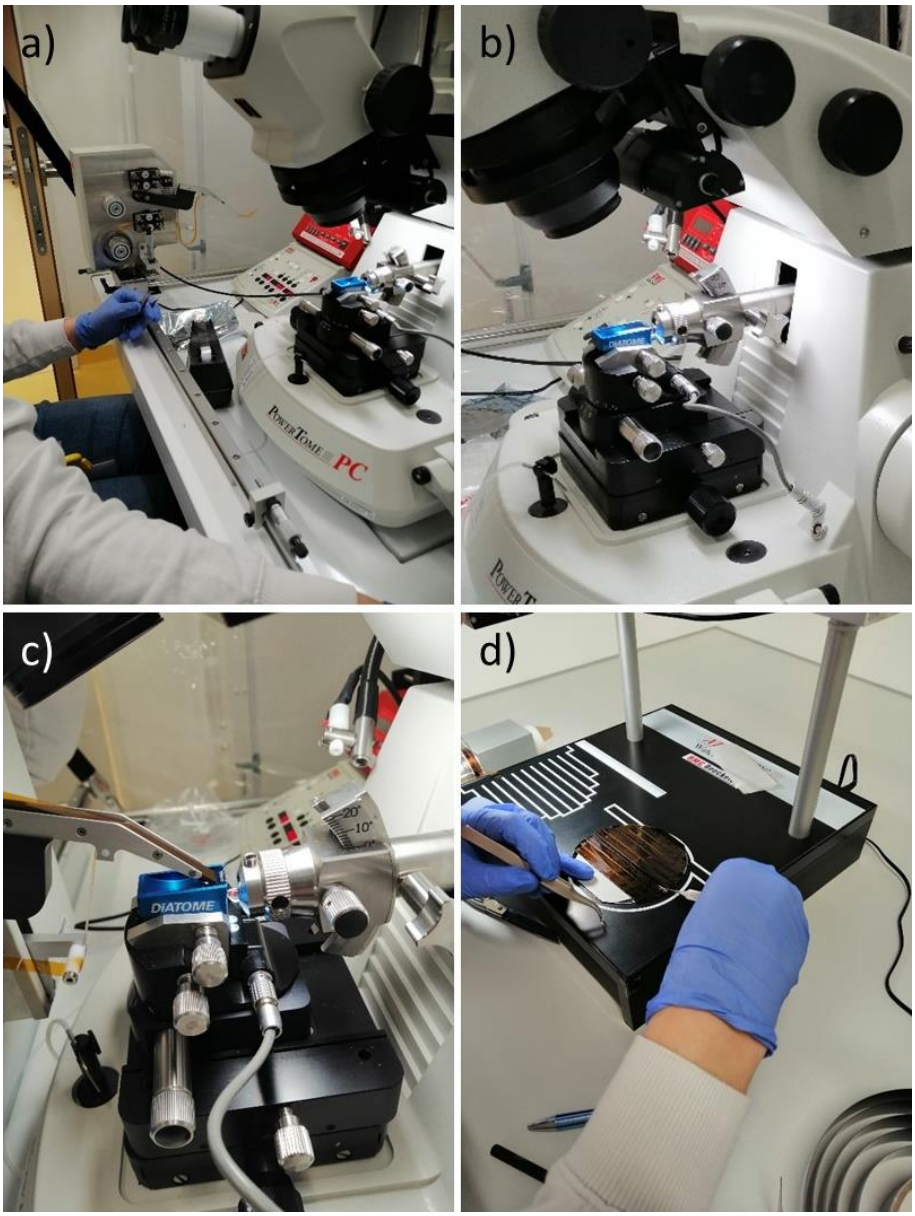

Figure 63: Impressions from the *ATUMtome* sectioning at the Medical University of Graz: (a) setup of the ATUM device, (b) trimming of the sample, (c) tip of the ATUM device lowered in the collecting position, (d) mounting of the tapes on the wafer

7.3 Recording of the Sections with *Atlas 5*

The whole process of imaging the wafer is performed with the program *Atlas 5* from *ZEISS*. This program enables large area imaging (LAI) and large area mapping (LAM), if an EDX detector is available. It controls the scan generator and the stage movement of the SEM. For the following measurements a *ZEISS Sigma 500 VP* with *Atlas 5* at the Medical University of Graz was used.

Before electron microscopic investigation of the sections carbon coating (high vacuum imaging) is applied to the wafer. Additionally to the samples 3 TEM grids are positioned on the wafer to enable the alignment of *Atlas 5* with the microscope. For the alignment a photograph of the wafer with the TEM grids is taken. Then the positions of the grids are approached in the SEM and the coordinates are saved (different mesh sizes or shapes of the grids allow a

definitive assignment of the positions). The photograph of the wafer is loaded into *Atlas 5* and the grids get imaged with the SEM in *Atlas 5* (the saved coordinates are used to locate the grids). With the images of the grids the photograph is aligned to the real position of the wafer within the SEM. After this step the photograph in *Atlas 5* shows the location of the wafer and can be used for navigation on it. In the next step a BSE image with low pixel resolution of the complete wafer (the scanning area has to be selected) is recorded. This area is then separated into individual tiles by the software (there is an upper limit for the real size and pixel size, which can be recorded with the SEM). Then the program scans tile after tile and automatically stitches them together into a large image. For this recording a resolution of 2 µm/px was chosen. Such an overview image enables the selection of the scan area for the individual sections. The overview image is shown in Figure 64 with enlarged regions.

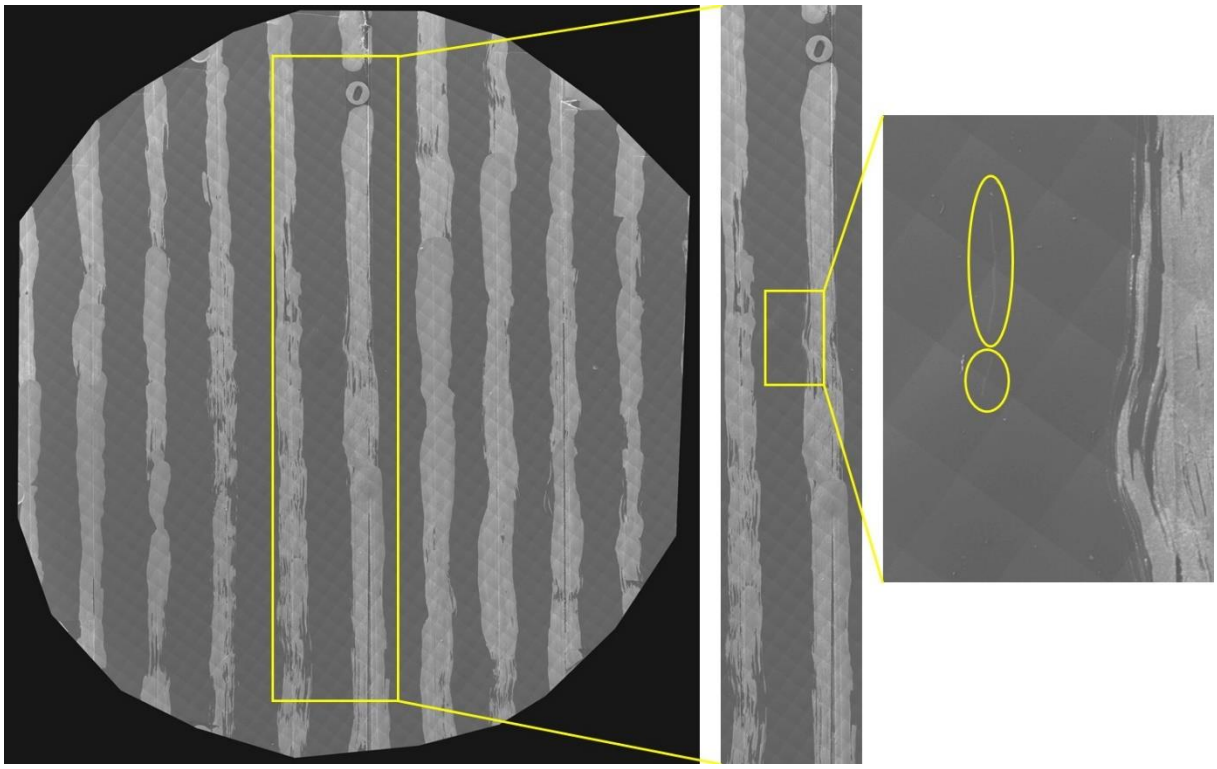

Figure 64: Overview image of the wafer with two enlarged regions. The brighter areas are conducting silver. (image width of the left image: ~10 cm)

In the right image of Figure 64 one can see the individual sections (marked with yellow ovals). It is important to know that the real position of the sections on the wafer can differ from the position on the image due to stitching errors. Therefore, it is important to control the positions of some sections manually to get sure, that the selected area for scanning covers the full area of each section. In the right of Figure 64 image it is visible, that the sections come in packs of connected slices like stated in (Baena et al., 2019). With *Atlas 5* it is possible to record all sections in one operation. That means that the imaging area is specified for all sections before starting the recording. Due to the different rotation of the slices on the wafer the selection window has to be altered for each slice. After defining the recording area, the imaging parameters have to be chosen (see below). Directly before the recording starts it is possible to adjust the focus for each individual section (this is necessary because not every position of

the wafer has the exact same height). For imagining of the sections, the BSE detector (HDAsB) was used. The imaging parameters were:

- Lateral resolution: 25 nm/px
- High voltage: 10 kV
- Pixel dwell time: 7 µs
- WD: 6.7 mm

The selected area for scanning was approximately half of the sections. After gathering of the images, a manual correction to the automatic stitching process was needed (see part 7.3.1). In Figure 65 a BSE image of a section is shown. Due to the size of the selected area only few details are visible.

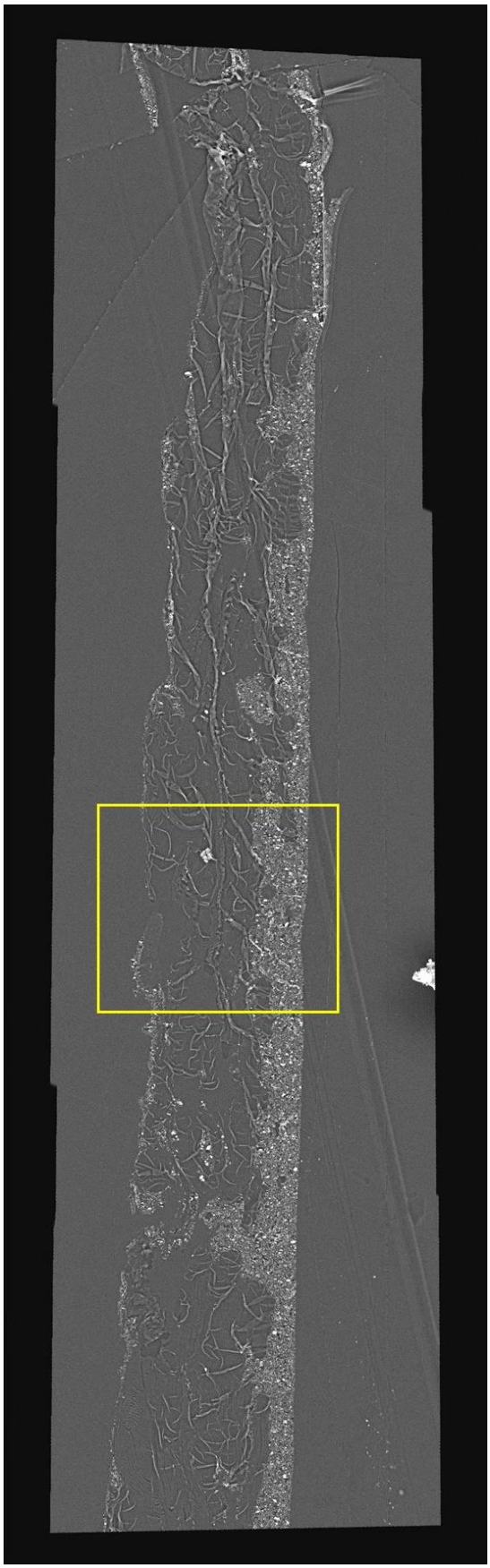

Figure 65: BSE image of the scanned area of a section (image size: ~460x140 µm², digitally enhanced contrast)

For a better examination of the image, the yellow marked rectangle is enlarged in Figure 66.

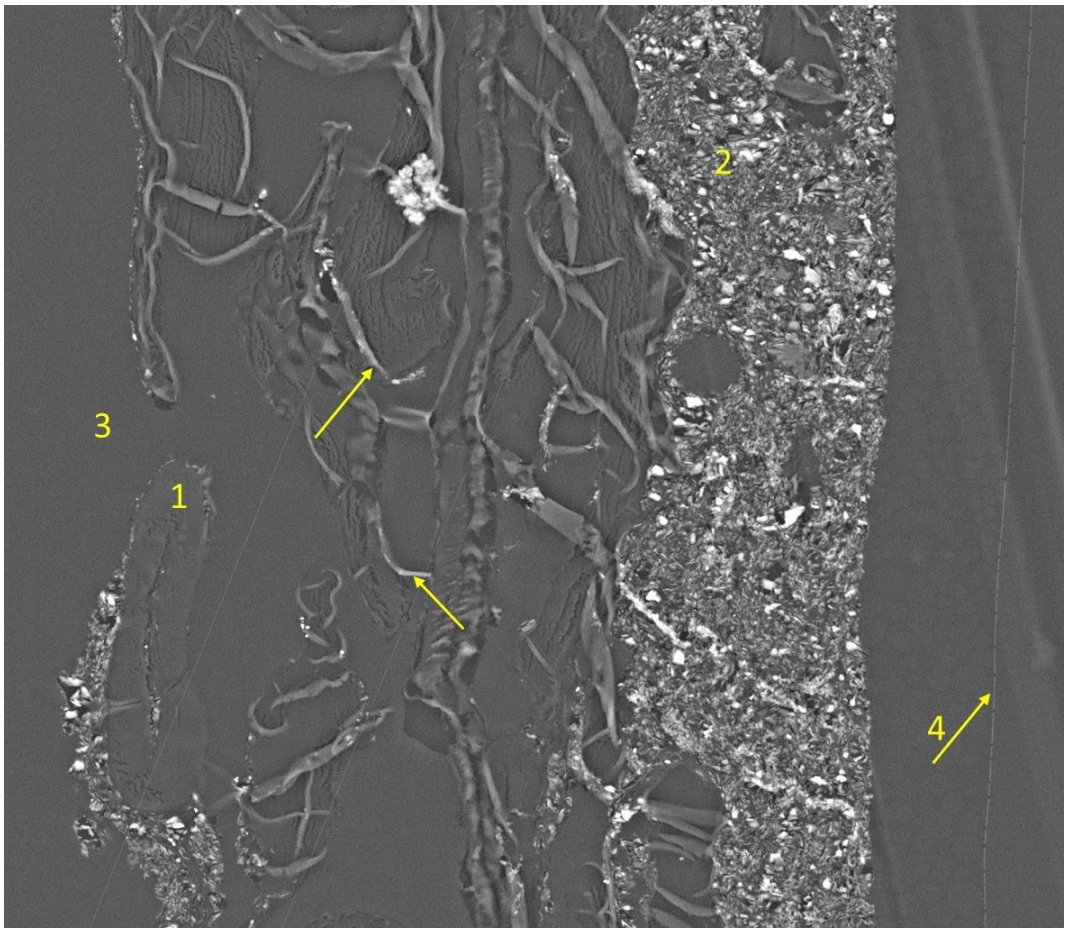

Figure 66: Zoom into the BSE image of the full section: (1) cellulose fiber, (2) filler material, (3) embedding resin. The unnumbered arrows mark regions with wrinkles. Arrow 4 marks the detached paint layer. (image width: ~65 µm, digitally enhanced contrast)

In Figure 66 several different regions are marked. Region 1 is most probably a cellulose fiber, because this feature is slightly brighter than the surrounding and has a well-known morphology like the cellulose in (Zankel et al., 2009). The bright regions marked with number 2 are filler material. The resin (matrix), which was used for embedding, is marked with number 3. Over the whole section there are comparatively bright features (two are marked representatively with yellow arrows). These features are most probably wrinkles, which were introduced during the preparation process. The wrinkles lower the image quality significantly and hinder the evaluation process, which will be discussed in the next parts of the thesis, and make it impossible to see cellulose (only a few single fibers are visible). From previous examinations it is known that cellulose is present at the whole area of the block-face. Near the right edge of Figure 66 a small bright line is visible (marked with arrow 4). This is most probably the paint layer, which got detached during embedding.

A very interesting discovery was the minimal amount of beam damage after recording all sections. Typically soft matter samples are very prone to beam damage which can make investigations complicated. One possible explanation for the minimal amount of beam damage is the thinness of the sections (100 nm). Most of the interaction of the electrons happens below the sections in the tape. To prove this assumption, a simulation of the electron-sample interaction with the Monte Carlo software *CASINO* (Drouin et al., 2007) was performed. For the simulation of the sample Kapton was used as substrate with a 100 nm thin

layer of cellulose on the top. In the simulation the trajectories of 10,000 electrons with a primary energy of 10 keV were calculated. The result is shown in Figure 67. Most of the electrons pass the cellulose layer with little scattering (similar to TEM) and lose most of their energy in the Kapton layer (size of the interaction volume).

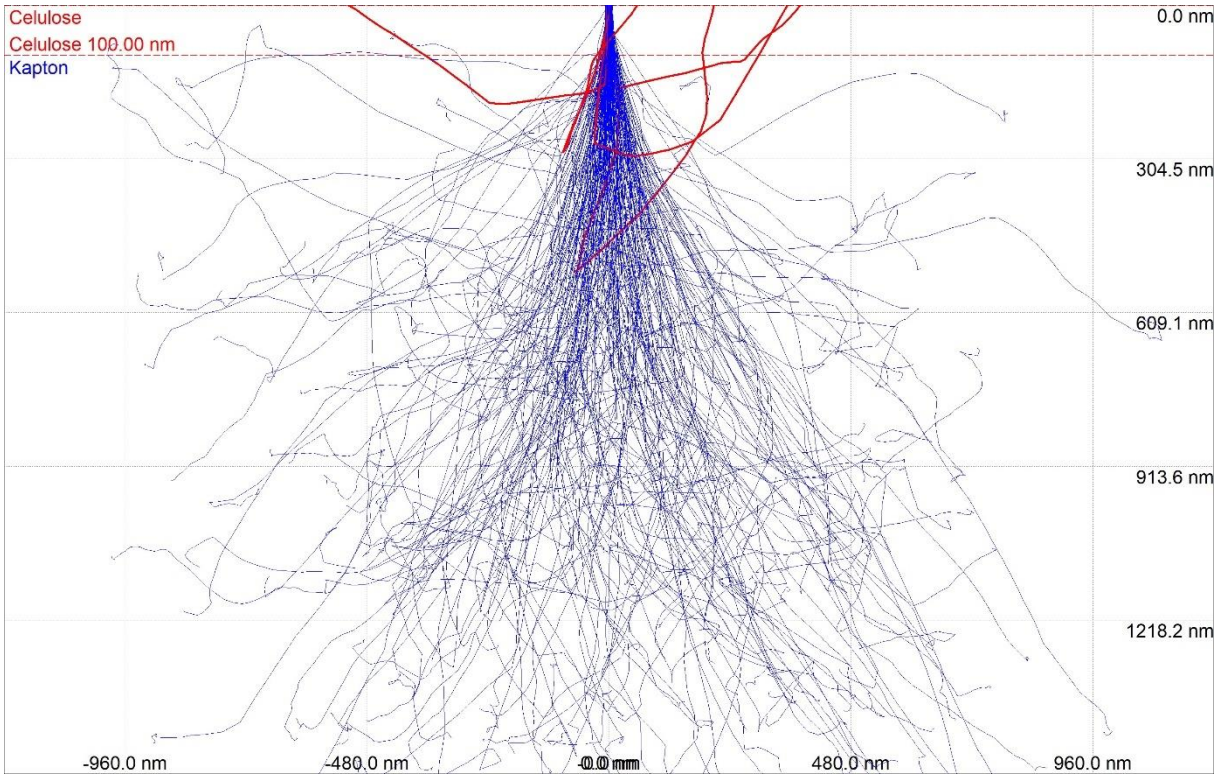

Figure 67: Monte Carlo simulation of the electron-sample interaction. Blue lines are trajectories of primary electrons, red lines are trajectories of backscattered electrons. Simulation was performed with *CASINO* (Drouin et al., 2007)

7.3.1 Stitching of Tiles in *Atlas 5*

Due to the large areas of images it is not possible to scan the whole region in one single image. With the program *Atlas 5* the area is segmented into a mosaic to cover the region with equally sized tiles (a tile gets partially recorded if only a part of it is located in the ROI). The tile size can be adjusted by the user like the other imaging parameters. Because the stage movement is not 100% accurate the tiles are scanned with a specified overlay (standard value is 10%) to make stitching possible.

Despite the relatively good result of the automatically stitched mosaic there are stitching errors which means that neighboring tiles are not perfectly aligned. In order to correct these stitching errors *Atlas 5* offers an inbuilt software procedure. The UI of *Atlas 5* with the *stitch mosaic feature* is shown in Figure 68.

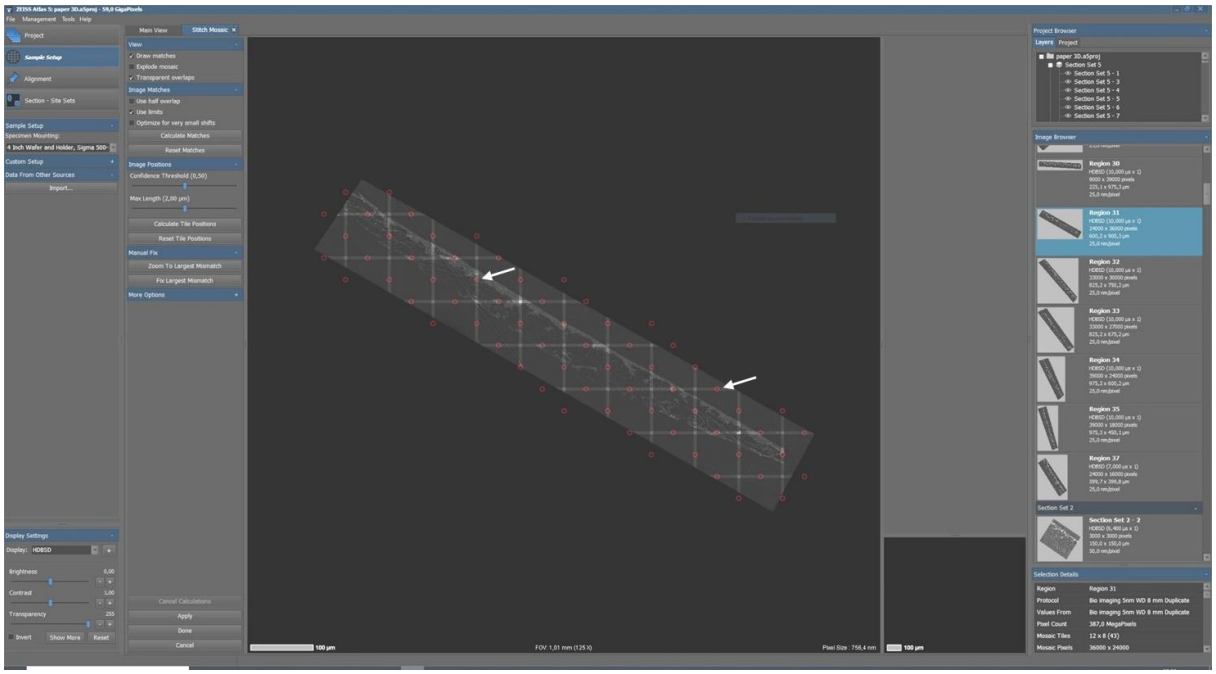

Figure 68: UI of *Atlas 5* with the *stitch mosaic feature*. The tile borders are marked with red circles (two are additionally marked with white arrows).

In the UI shown in Figure 68 every tile border can be realigned by clicking on a red circle (two are additionally marked with white arrows). This opens a separate window, where the two tiles can be aligned with the help of complementary colors. The left image in Figure 69 shows a tile border after the automatic stitching procedure from *Atlas 5*. The result is not poor but it is clear that the positioning of the right tile (magenta) is a little bit too high compared to the left tile (green). The corrected stitching of the tile border is shown in the right image of Figure 69. To achieve this result one of the tiles (green or magenta) is moved until the features within the tile border zone align and the color changes to white. By applying this procedure to all tile borders of the mosaic the stitching errors can be compensated.

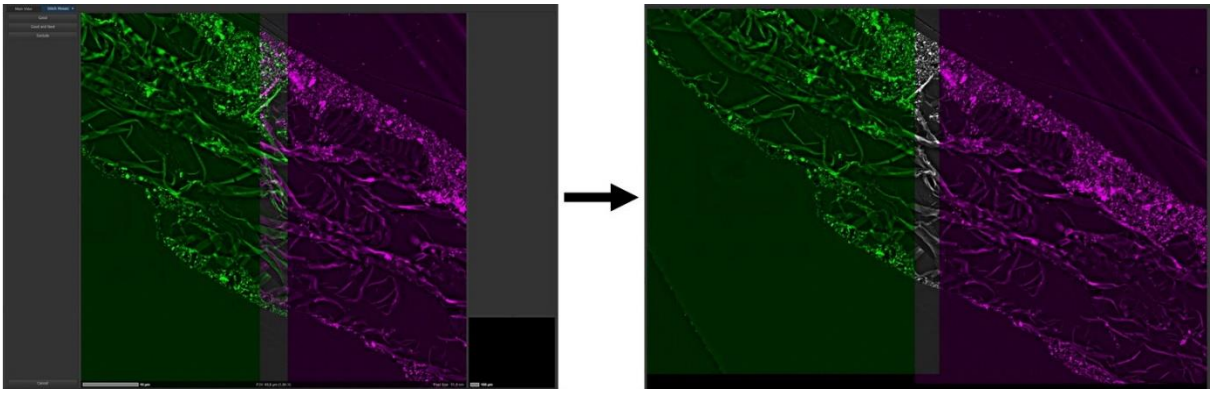

Figure 69: Correcting the stitching of a tile border: left is the automatically stitched result; right is the manually corrected tile border

The correction process for the stitching of the mosaic can be time consuming. To save time it is best to use large tiles to minimize the amount of tile borders. The resolution limits the tile size, because the microscope has a finite image width. If the resolution is to low the aperture of the microscope becomes visible in the images. For lower resolutions therefore the image

width is the limiting parameter for the tile size. At high resolutions the tile size is in all cases smaller than the image width.

7.3.2 Large Area Imaging (LAI) with *Atlas 5*

During the work with the *Atlas 5* software a dedicated test of large area imaging was performed. In this case a macroscopic area was imaged with high resolution using conventional plotter paper with a 10 nm carbon coating as sample (Figure 70).

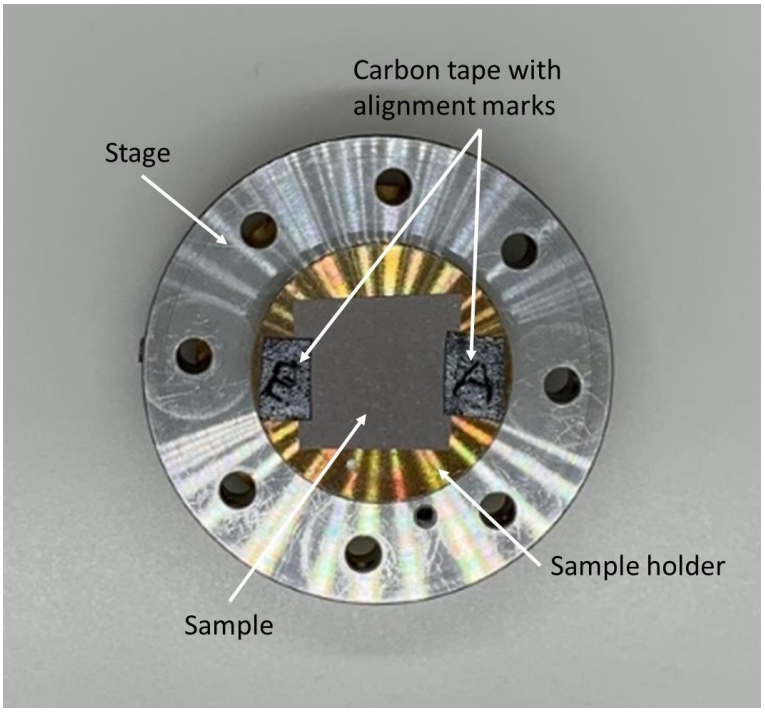

Figure 70: Paper sample with a conductive 10 nm carbon coating for large area imaging. The letters E and A scribed into the carbon tape are for aligning the sample in *Atlas 5*.

The same recording procedure like for the *ATUMtome* sections is used with the difference that only one area is imaged. First an overview image of the sample with low resolution was recorded (Figure 71a) for selecting the ROI. In the overview image the individual tiles are well visible. The enlarged part (Figure 71b) of this overview shows the overlapping corner of 4 tiles. The cause of the darker part (marked with a white arrow) are imaging artefacts, because the chosen field of view for the tile was too large.

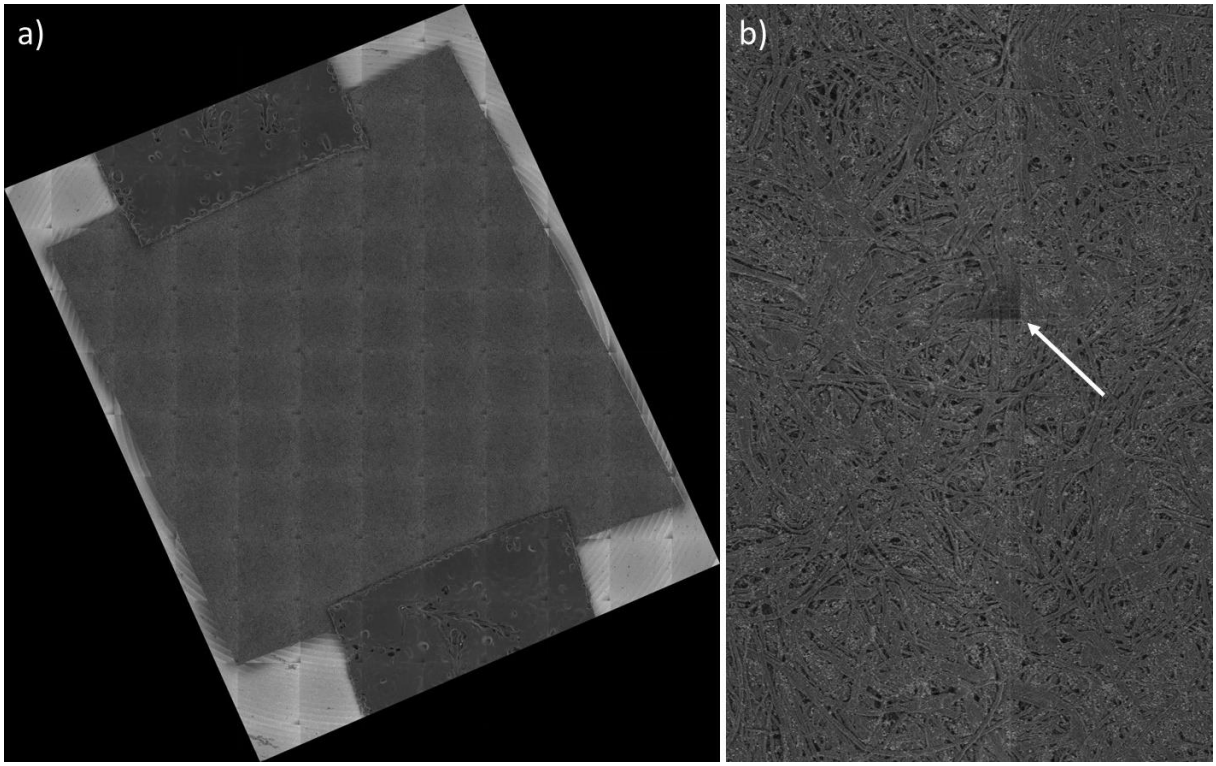

Figure 71: Overview scan of the paper sample: (a) the whole sample on the sample holder is visible(image width: 2.2 cm, BSE image), (b) enlarged part of the overview image

In the middle of the sample a 6.4x4.8 mm^2 area was chosen as ROI. For imagining the BSE detector (HDAsB) was used. The imaging parameters were:

- Lateral resolution: 50 nm/px
- High voltage: 10 kV
- Pixel dwell time: 7 µs
- WD: 4.2 mm
- Tile size: 1.6x1.6 mm^2 (32,000x32,000 px)

With these parameters the imaged area had a pixel size of 128,000x96,000 px (imaging time: ~22 . In Figure 72 the large area image is shown. Due to the size of the image it is not possible to store it in original pixel resolution (the stored image has a pixel resolution of 23,000x19,800 px).

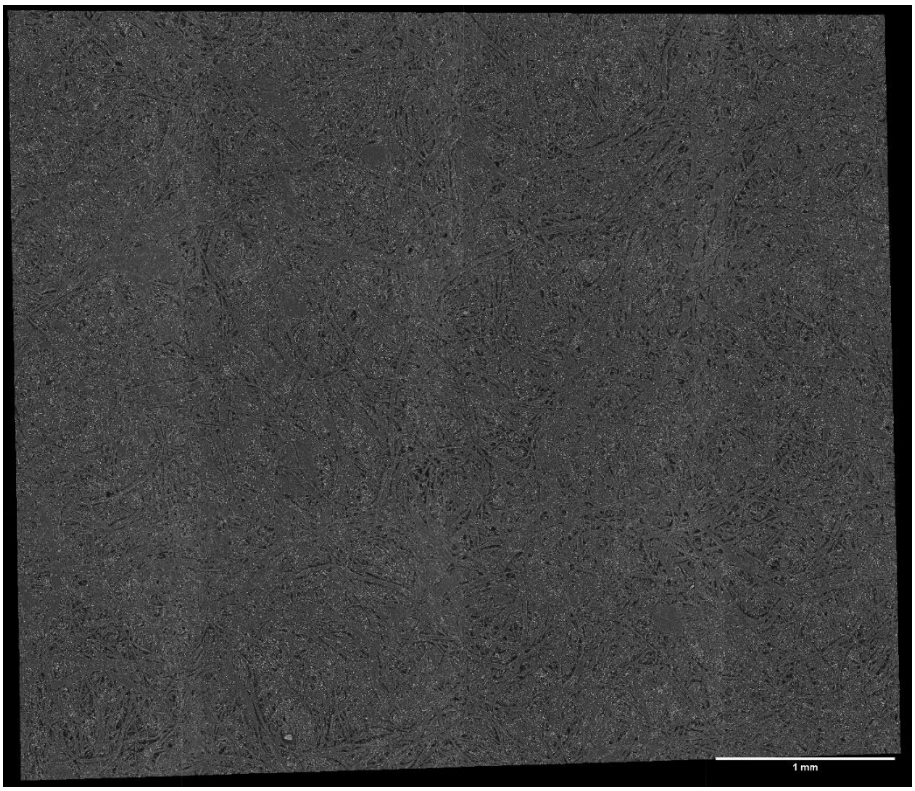

Figure 72: Stitched large area image of the paper sample

An export in original resolution is possible as raw image (the file size would be around 9 GB) or with TIFF tiles (with an individual pixel resolution of 2048x2048 px). In Figure 73 four stitched TIFF tiles show the original resolution of this image. Cellulose and filler material (also the small grains) are clearly distinguishable.

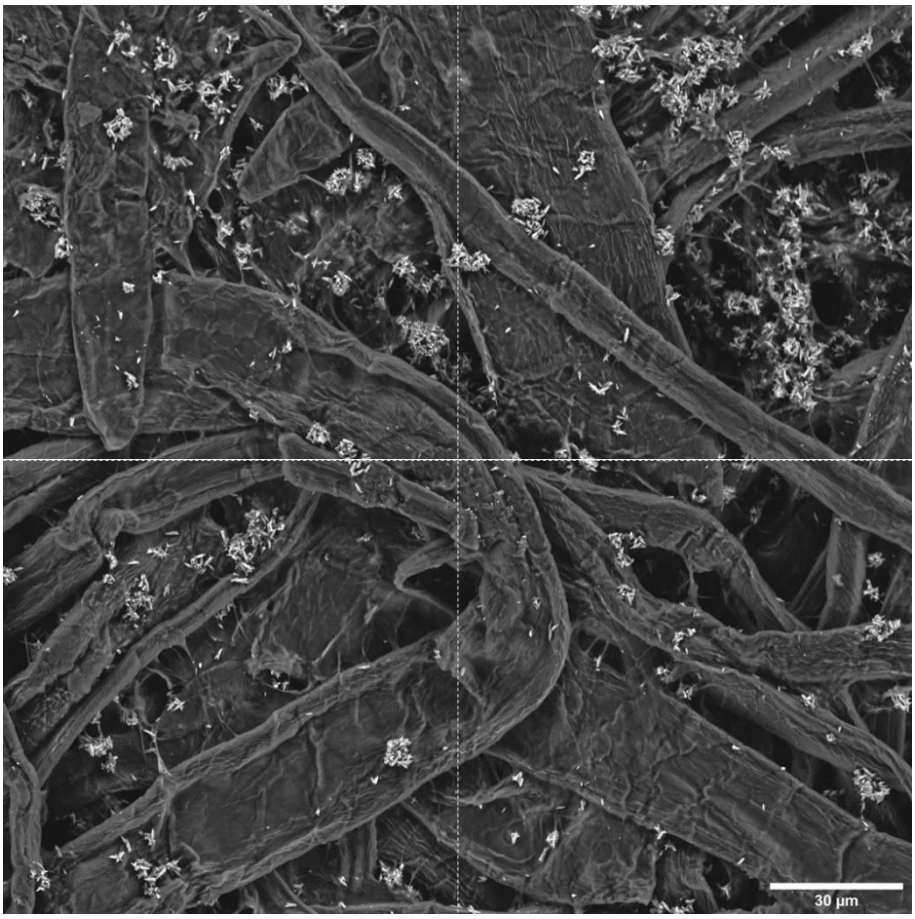

Figure 73: Part of the large area image in original resolution. This image consists of four TIFF tiles (the borders are marked with the dotted white lines).

With *Atlas 5* also dedicated large area imaging at high resolution is possible. The whole system (software/microscope) is stable enough during the large area imaging procedure with *Atlas 5*. The question which arises with such large images is a possible data evaluation. Images with this size are nearly impossible to be evaluated with programs like *ilastik*, because conventional computers cannot handle such large data files.

For comparison a large area imaging test (lateral resolution: 50 nm/px) on the same sample was performed with the *AZtec* software from *Oxford Instruments* (Abingdon, England). The quality of the recording is similar to *Atlas 5* and the automatic stitching feature works well (the results are shown in the Appendix from Figure 97 to Figure 99). An advantage of the *AZtec* software is the possibility to record an SE and a BSE image simultaneously. A major disadvantage compared to *Atlas 5* are limited export options (the size of an exported LAI is limited to ~8000x8000 px).

7.4 Evaluation of the Results

In most cases the main goal of a 3D investigation in the SEM is a volume reconstruction of the phases from interest. The obtained data are then used to answer scientific questions about the material and its structure. Unfortunately, the bad quality of the sections (wrinkles) indicates that a successful evaluation of the data will be very difficult or even impossible.

7.4.1 Segmentation of the Filler Material

For a 3D reconstruction a segmentation of the different phases of the sample is needed. In the case of the label sample it was decided to only try a segmentation for the filler particles and not for the cellulose. Because of the bad quality it is not possible to differentiate cellulose from the embedding resin. For the segmentation tests only a small part of the whole section (2500x2000 px) was used in order to lower the computation time to a reasonable value. The segmentation was carried out with the program *ilastik* (for a detailed explanation the reader is referred to section 3.2). In relation to the general bad quality of the images the segmentation worked quite well as shown in Figure 74.

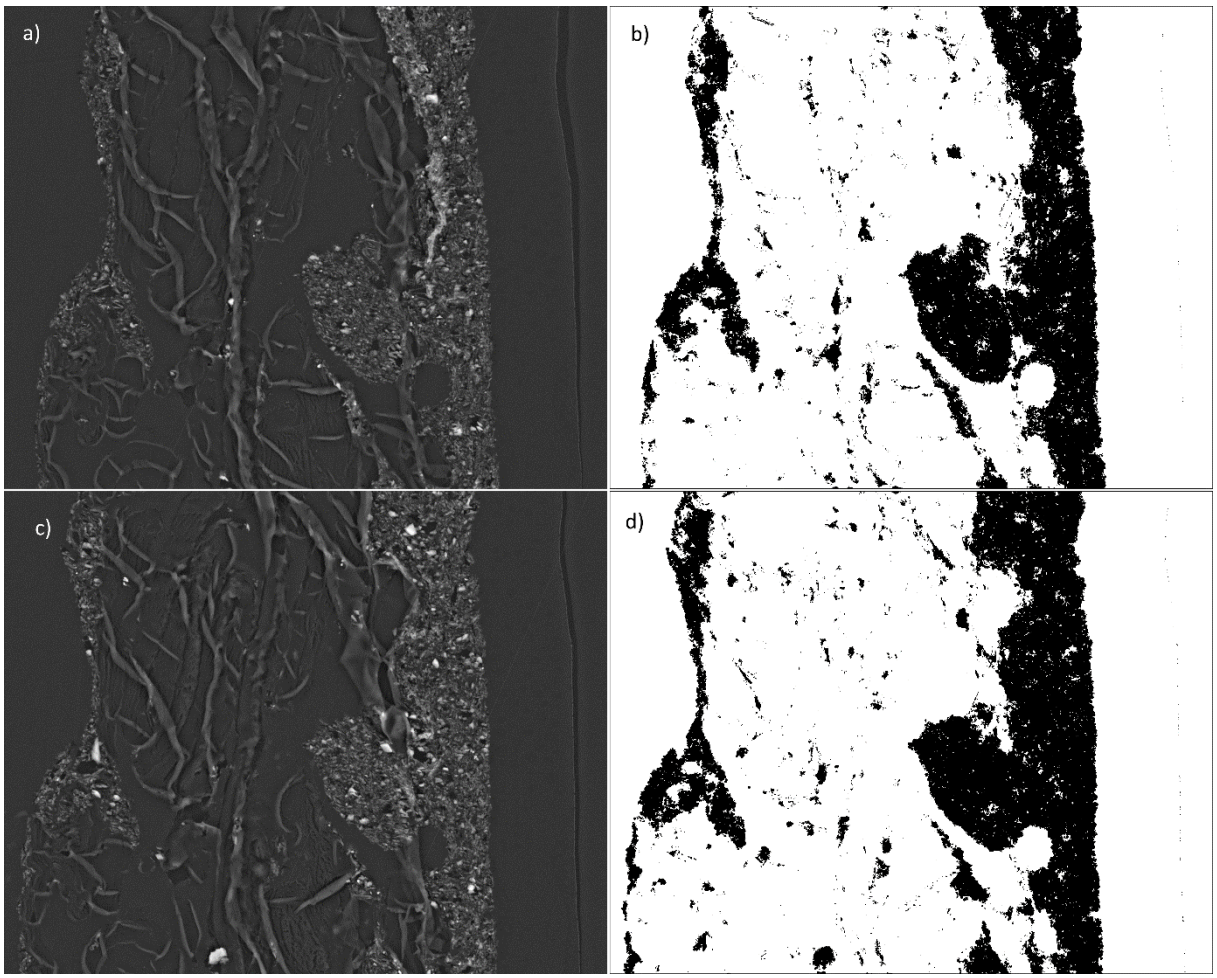

Figure 74: Attempt of an image segmentation of two consecutive sections: (a) BSE image of the preceding section; (b) image segmentation with *ilastik* of the preceding section; (c) BSE image of the subsequent section; (d) image segmentation with *ilastik* of the subsequent section. (image width for all images: 62.5 µm)

The wrinkles make the segmentation very problematic, because the grayscale of the wrinkles and the filler material is in the same range. Additionally, the wrinkles have no defined shape/edge (they are randomly distributed over the section), which reduces the efficiency of *ilastik* even more. Therefore, it is impossible for the program to separate them totally from the filler material. Additionally, in the areas of filler material there are parts which were not correctly assigned. In the case of thin sections the contrast difference of areas with filler and the remainder is not as strong as for the samples (Figure 61). The reason for the weaker

contrast could be the generation depth of BSEs (Figure 1). Most of the BSEs are generated beyond 100 nm and therefore below the sample.

After the evaluation with *ilastik* the segmentations are too noisy and cannot be used for a 3D reconstruction. An attempt to enhance the quality of the segmentations was manual correction. This process is very time consuming and therefore only done for a small number of sections. In Figure 75 the raw image segmentation with *ilastik* (left) vs. the enhanced image segmentation (right) of section 5 is shown.

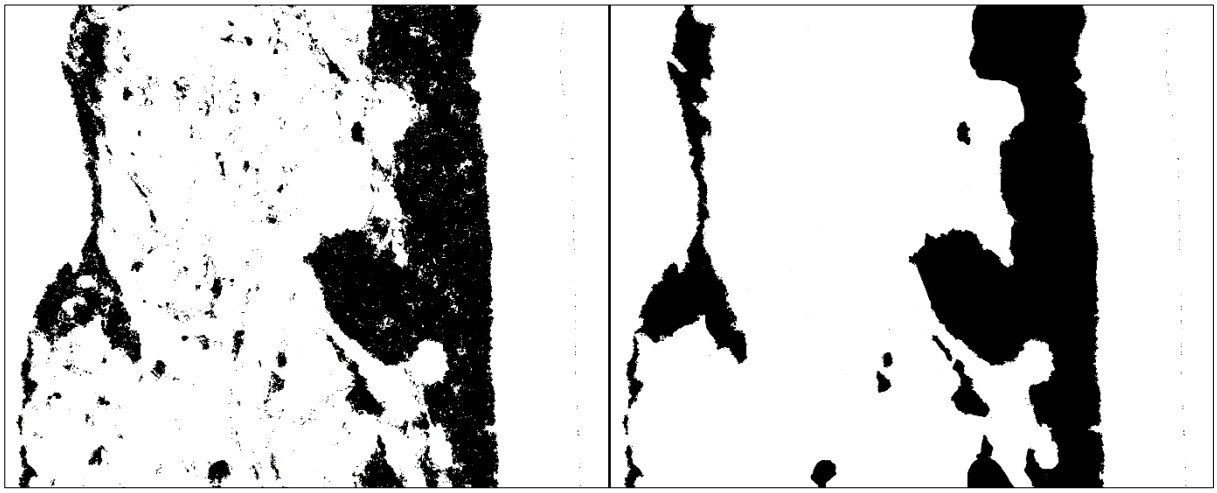

Figure 75: Result of the image segmentation with *ilastik* (left), manually enhanced result (right) of section 5

The quality difference between the raw and enhanced segmentation is large. With the quality of the enhanced segmentation a 3D reconstruction would be possible, but during the evaluation of the sections a fundamental problem arose. The width of the sections varies strongly. By overlaying segmentations of two following sections a width difference in the range of one micron was measured. In Figure 76 the overlay of the image segmentations of two following sections is shown.

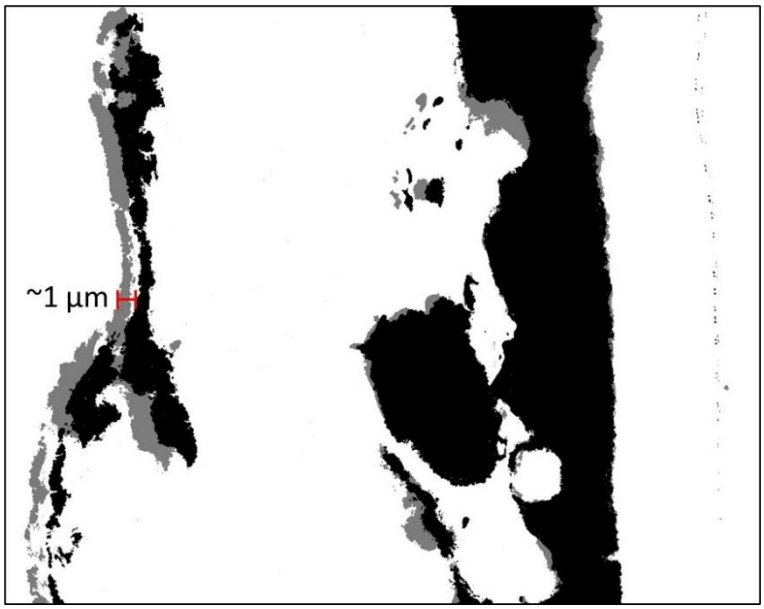

Figure 76: Overlay of the image segmentations of two following sections

In this overlay the segmentations are aligned at the right border of the filler material. It is obvious that the width of the sections differs strongly. The width change is most likely a consequence of the large number of wrinkles in the sections. For a definitive answer, additional electron microscopic investigations are needed. The results of the additional investigations are presented in the following section.

These width differences make it impossible to align the individual sections for a 3D reconstruction. In the overlay it is also visible that the shape of the two following sections changes much. Such a change in morphology within 100 nm is unlikely a sample property.

7.4.2 Investigations of Uncoated Sections in a VPSEM

With a VPSEM (*ESEM Quanta 600 FEG*) the origin of the wrinkles was investigated. The wrinkling of the sections has two possible sources: the cutting process (likely) and the carbon coating process (unlikely). In order to eliminate the coating process as origin for the wrinkles uncoated sections were investigated (only a part of the originally cut sections was transferred onto a wafer for investigationa in the SEM). The result of the investigation is shown in Figure 77 (left: SE image, right: BSE image).

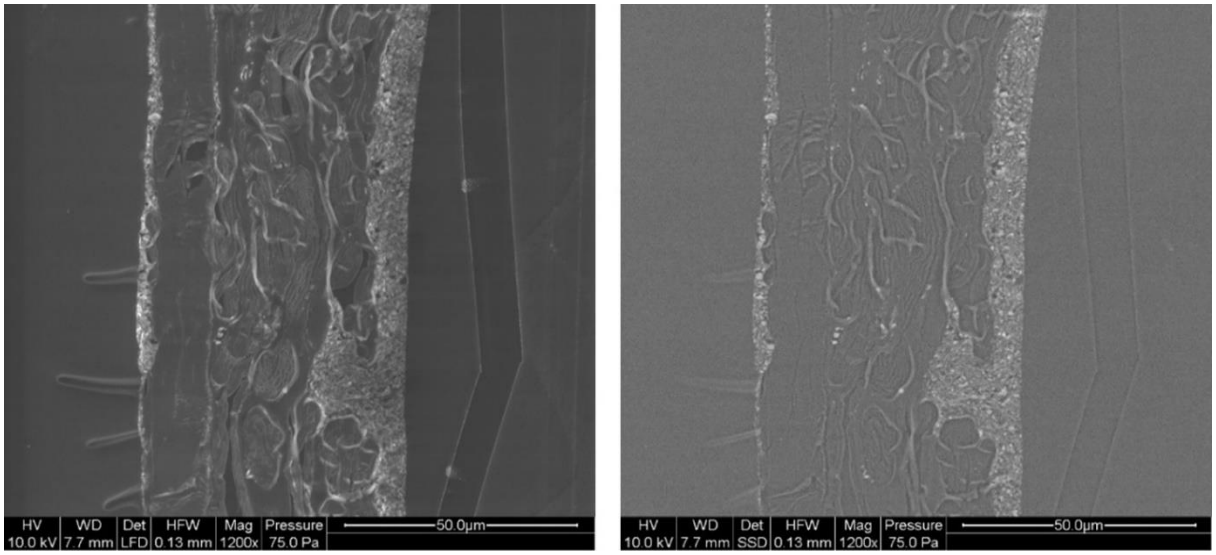

Figure 77: Uncoated section of the label: left SE, right BSE (low vacuum mode p = 65 Pa, imaging gas: H_2O)

The uncoated sections have a very similar appearance as the coated ones (the uncoated sections also have wrinkles). This leads to the conclusion that the wrinkles have to be artefacts of the cutting respectively of the whole *ATUMtome* process.

A likely explanation is the interaction of the sections with water during the cutting process. The cellulose fibers in the paper label swell and cause the thin sections to wrinkle. This behavior would be also an explanation for the different widths of two following sections, because the swelling process is not the same for each fiber.

7.5 Test of Additional Spectroscopic Measurements on the Sections – EDX and Raman

A very interesting idea is the usage of the *ATUMtome* sections for additional spectroscopic investigations. In comparison to an SBFSEM approach like *3View* the collected slices would enable examinations in different devices. For example, it would be possible to make Raman measurements in an *ex situ* Raman microscope and continue with EDX measurements and imaging in an SEM.

In the case of EDX analysis the main question is, whether the resulting X-ray signal from thin sections is high enough to deliver results in a reasonable time. In the case of soft matter samples (*ATUMtome* is limited to sliceable samples which means commonly soft matter materials) the interaction of beam and sample can lead to serious beam damage. As stated in section 7.3 the beam damage during imaging was not a big problem, but the recording times of EDX analysis are much longer than imaging. Commonly the pixel dwell times are several magnitudes longer than for imaging.

In a first test one part of a coated section (on the wafer) is used for an EDX analysis. The usage of coated samples enables the investigation in high vacuum to avoid the skirt effect (see section 2.3.3). Of course, it would be possible to try EDX analysis even on uncoated samples. For a first measurement spot spectra at four positions were collected (Figure 78 shows the positions of the spots). For these measurements a high voltage of 5 kV was used. The resulting spectra are shown in Figure 79.

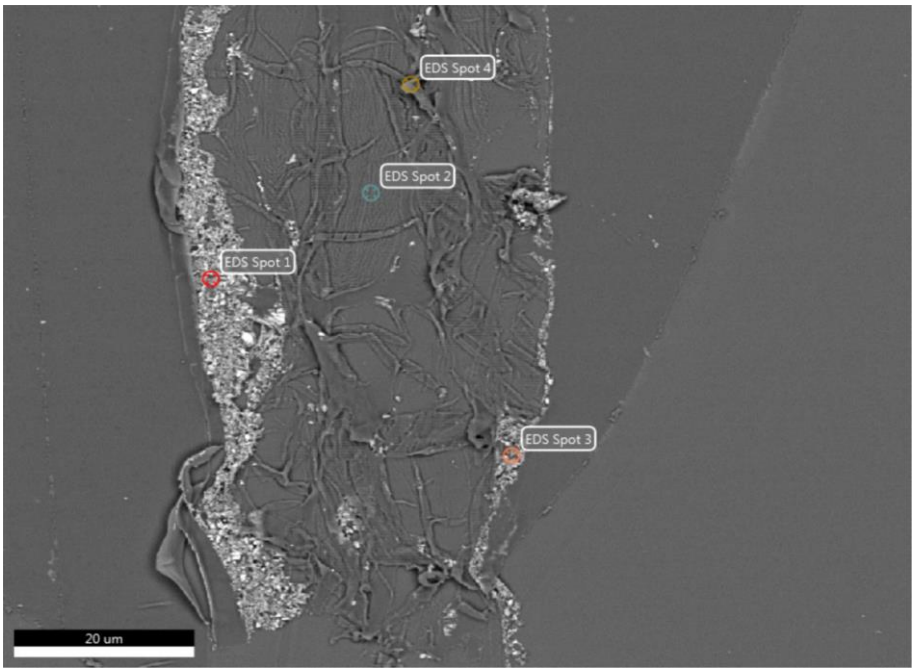

Figure 78: Positions of the EDX spot measurements of a coated section on the wafer

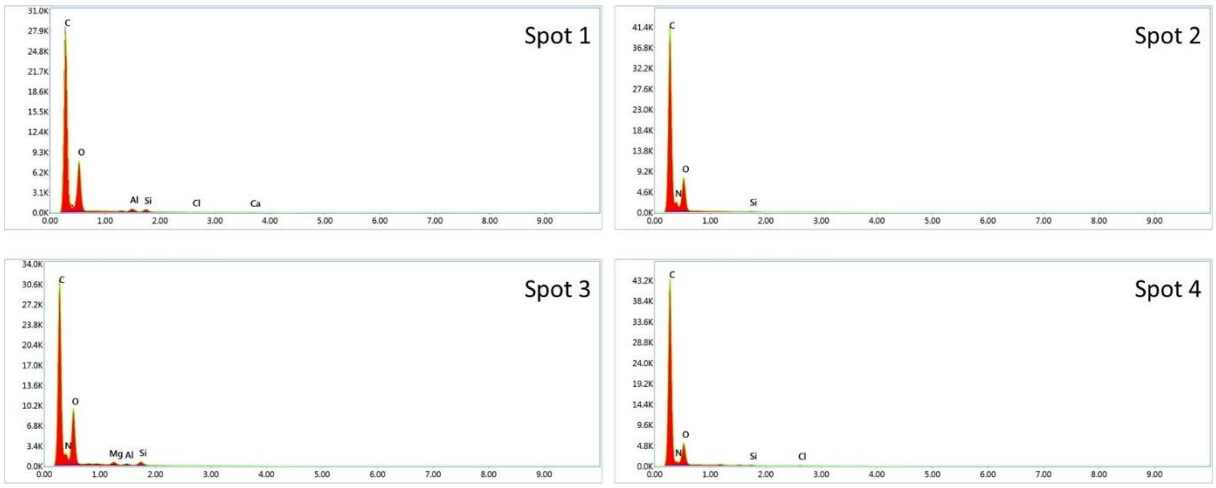

Figure 79: EDX spectra for the four spots of Figure 78 (high voltage: 5 kV)

The regions of the cellulose and the embedding polymer show mostly carbon, oxygen, and nitrogen. Also, small calcium and chlorine peaks were detectable. In the regions of the filler material additional peaks of magnesium, aluminum and silicon were detected. These results are not usable for quantification, but they show that the different materials are detectable. In a way the situation is comparable to TEM. The EDX signal is produced by a very thin sample. The main difference is that the electron energies are much lower in an SEM and the *Kapton* and adhesion tape deliver an additional signal. The measurement was repeated at 10 kV for a higher count rate and to clearly identify some peaks (the high voltage limits the possible EDX peaks). The higher count rate at 10 kV was used for a mapping test. For this map a pixel dwell time of 1500 µs/px was used and 8 frames were recorded. The total pixel dwell time is then 12 ms. Figure 80 shows the result of this test. The quality is not very useful, but also in this mapping the areas of filler are recognizable.

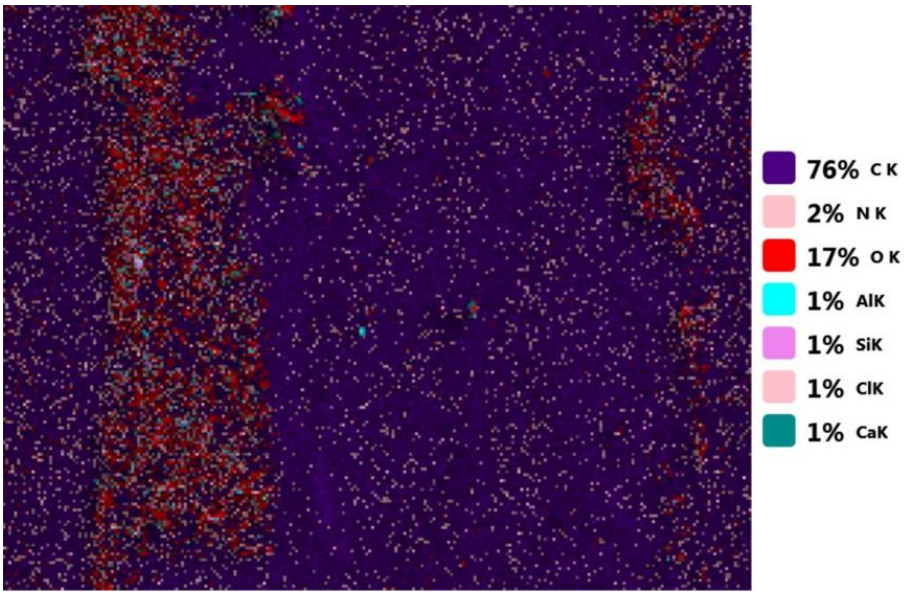

Figure 80: EDX mapping test of one section (high voltage: 10 kV)

All these tests were carried out with an *EDAX Element* detector (detector area: 30 mm^2). With a larger detector area better results should be possible. For samples with three-dimensional

EDX interest this technique would be a good addition to existing ones (*3D elemental mapping* with *3View* and FIB).

The second investigation technique which could be used in combination with *ATUMtome* is Raman spectroscopy. The distinction of different polymers would be one aspect, which would be enabled by Raman spectroscopy in the scope of 3D investigations within the SEM. In theory it should be possible to perform Raman spectroscopy on uncoated sections after the *ATUMtome* sample preparation. A question is, whether the polymer tape (*Kapton*) interferes strongly with the measurement. For the test several uncoated sections were investigated with the *RISE* system (see chapter 6.1.1). Figure 81a shows the BSE image of an uncoated section (low vacuum modus). The white rectangle marks the position of the stitched LIMI image (Figure 81b, 180° rotated in comparison to the BSE image) taken with the Raman microscope.

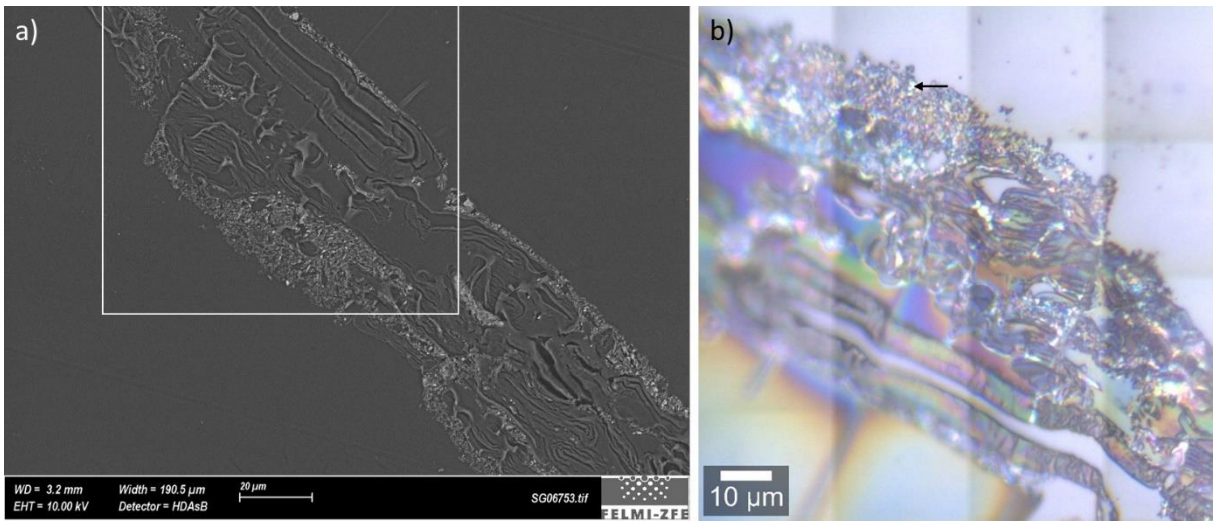

Figure 81: Section for the Raman test: (a) BSE image (low vacuum mode p = 40 Pa, imaging gas: nitrogen), (b) stitched LIMI image (the area marked with the white rectangle in the BSE image was recorded)

The acquisition of Raman spot spectra was tested in several regions of the sample. In nearly all cases only the Raman spectrum of Kapton (polyimide) could be recorded (Figure 82a). The spectrum of Kapton was recorded outside the section. Figure 82b shows the Raman spectrum of TiO_2 (anatase) which could be found in one region (marked with the black arrow in Figure 81b). For better visualization of the situation the spectra are not processed. Unfortunately, the recording of the spectra was not repeatable in other areas on the section. Although the Raman measurements were not repeatable the thin section has enough material to produce a detectable Raman signal (the first peak in the spectrum of TiO_2 is clearly visible).

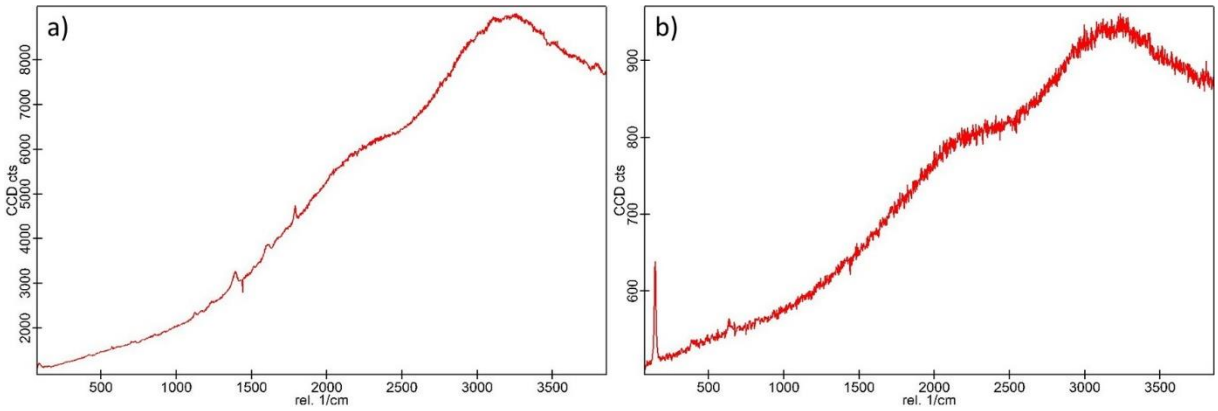

Figure 82: Raman spectra of the thin section: (a) spectrum of Kapton (polyimide) affected with fluorescence, (b) spectrum of TiO_2 (anatase) affected with fluorescence

The polymer tape causes a strong fluorescence which covers the Raman signals (in most cases) from the thin section (gathering of Raman spectra is not consistently reproducible). One possibility to overcome this obstacle is to use metallized polymer tapes to introduce an intermediate layer which is Raman neutral. This procedure was successfully applied in (Böhm et al., 2020).

7.6 3D Investigation of the Label Sample with *3View* (SBFSEM)

It was decided to make a complete 3D investigation of the label sample with the system *3View* to have a direct comparison to *ATUMtome* + *Atlas 5* with the same sample.

After sample preparation and the adjustment into 3View a standard 3D investigation was performed. For comparability the same slice thickness as in the *ATUMtome* experiment (100 nm) was chosen. The imaging parameters were:

- Lateral resolution: 50 nm/px
- High voltage: 7 kV
- Pixel dwell time: 40 µs
- WD: 7.1 mm
- Pixel resolution: 1300x1300 px
- Chamber pressure: 100 Pa (imaging gas: H_2O)

Due to the similarity of the sample over its whole length (Figure 65) only a smaller region was chosen for imaging. The lower high voltage compared to the recording with *Atlas 5* was used, because the BSE detector from *Gatan* is optimized for efficiency at lower electron energies. An example BSE image of the selected sample region is shown in Figure 83 (the image has an image width of 68.3 µm with a pixel resolution of 1300x1300 px). Compared to the recordings of the sections prepared with *ATUMtome*, all the phases (filler material, cellulose and resin) have different gray values and morphology (they can be distinguished). Even during the recording with *3View* some problems occurred: in the BSE image a big vertical stripe is visible. The cause of this stripe is a notch in the diamond knife (cutting artefact which cannot be omitted). Also some minor horizontal stripes occured (the origin of those stripes are most

likely instabilities in the chamber vacuum). There are also some areas with beam damage. As it was explained in chapter 3 it is possible to deal with these problems.

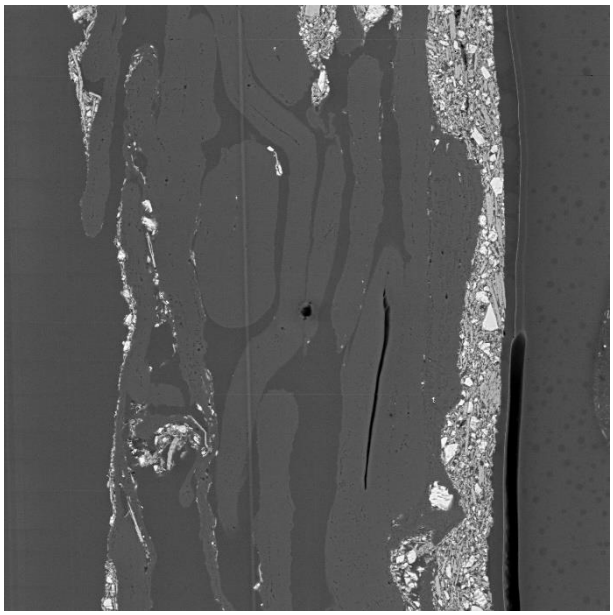

Figure 83: BSE image (detector from *Gatan*) of the block face of the paper label investigated with *3View* (image width: 68.3 µm)

A 3D investigation of 600 slices was performed. The investigated volume had the dimensions of 68.3x68.3x60 μm^3. In comparison to the *ATUMtome* slices on the wafer, beam damage can be a significant problem of *3View*. Most of the electron beam interaction happens in the bulk of the sample which is investigated in the following slices. The first slices show the worst beam damage due to the longer interaction time of the beam with the sample during the optimization of the imaging parameters (during this process the same area is repeatedly scanned which leads to a higher electron dose). Figure 84 shows the evolution of beam damage during the first slices. The image of the first slice shows strong beam damage in some areas and other parts are not strongly affected. Within the first cuts the whole ROI gets affected by beam damage (slice 5 is shown in Figure 84b). After 10 slices most of the beam damage is gone and a “clean” block-face can be imaged. Slice 10 and 15 show the increased beam damage in the middle (indicated by a white arrow in the images) of the ROI due to a wrong beam resting position (this problem could be fixed before further investigations e.g. the investigation of the special high quality sample in chapter 6).

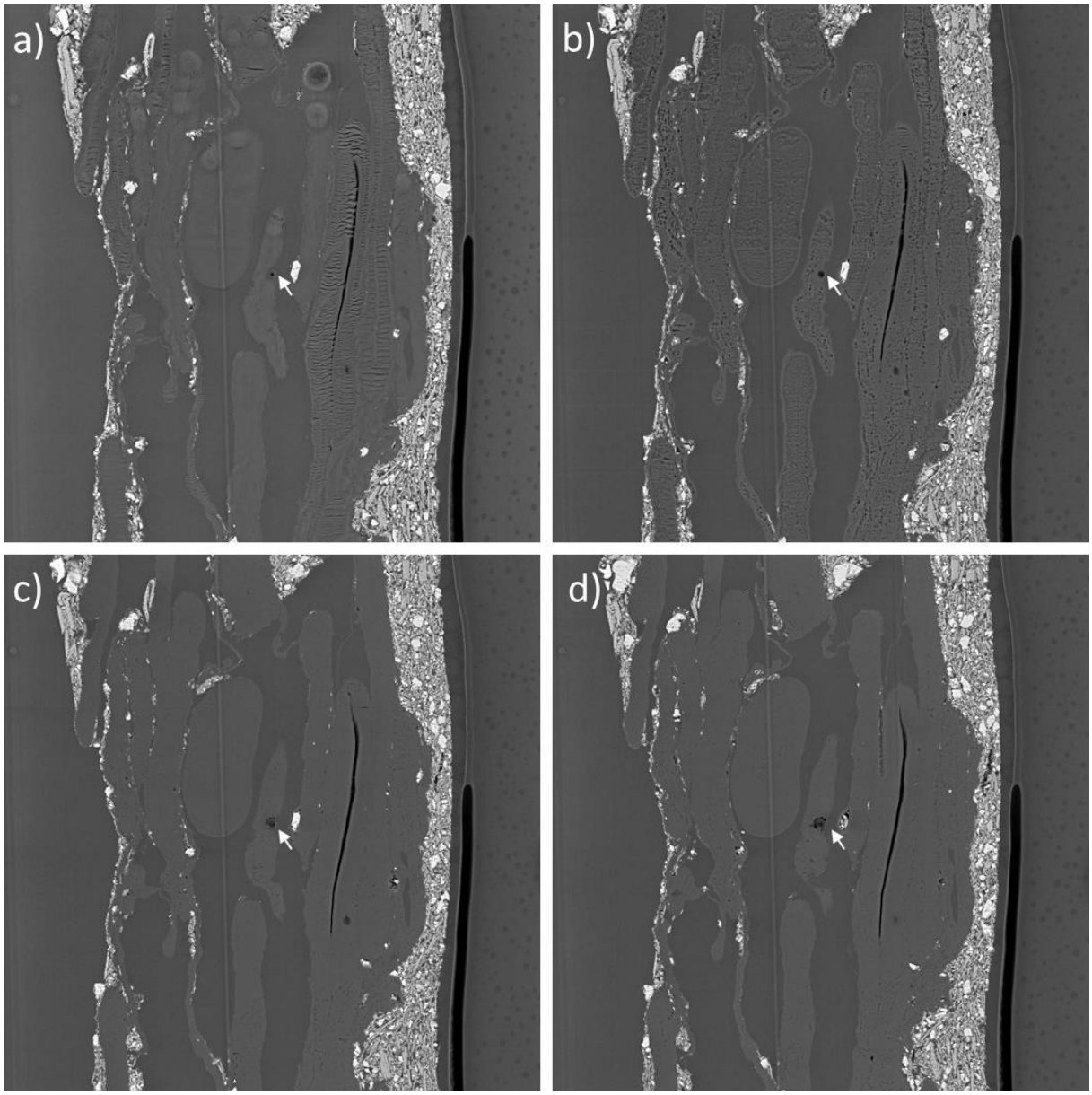

Figure 84: Evolution of beam damage at the start of a 3D investigation with *3View*: (a) slice 1, (b) slice 5, (c) slice 10 and (d) slice 15

Due to the beam damage the first 10 slices were discarded before starting with the evaluation. For the evaluation the image processing (enhancement and segmentation) described in chapter 3 was performed for 300 slices (the morphological structure of this sample is not changing much – over the whole volume only cellulose, filler material, resin and some voids are found). For this sample the segmentation was performed with *ilastik*. The visualization of the data was realized with the program *Avizo 9*. Figure 85 shows the evaluated volume of the 3D investigation. In the left image the uncorrected BSE micrographs in *ortho slice* visualization can be seen. In the middle of the investigated ROI the beam damage from the resting position is visible, which was corrected manually. The right image (Figure 85b) shows an *ortho slice* visualization of the image segmentation: black is the embedding resin, dark gray is cellulose, light gray is the filler material and white are voids (regions where the resin could not penetrate the sample).

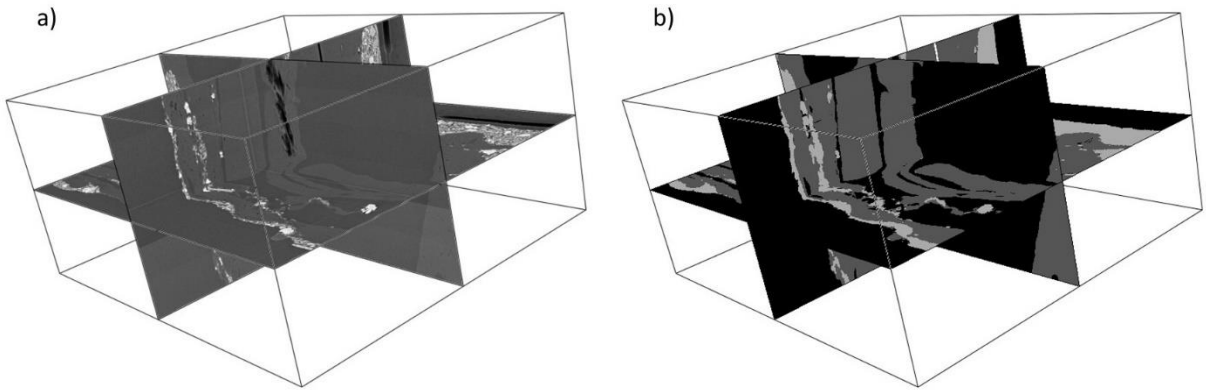

Figure 85: Visualization of the data with *ortho slice*: (a) BSE images as recorded, (b) fully segmented images (box size: 56x65x30 µm³)

With these segmentations the volume reconstruction of the individual phases was performed. The results of this reconstruction are shown in Figure 86. Cellulose is distributed over the whole sample volume. An interesting property of the cellulose fibers is that they are all oriented along one direction (y-axis). The filler material (Figure 86b) is found mostly in layers (small filler particles are distributed within the layers). The voids (Figure 86c) are volumes where the resin could not penetrate. In the combined reconstruction (Figure 86d) one sees, that a relevant fraction of the paper label are voids (volumes filled with embedding resin were voids prior to sample preparation).

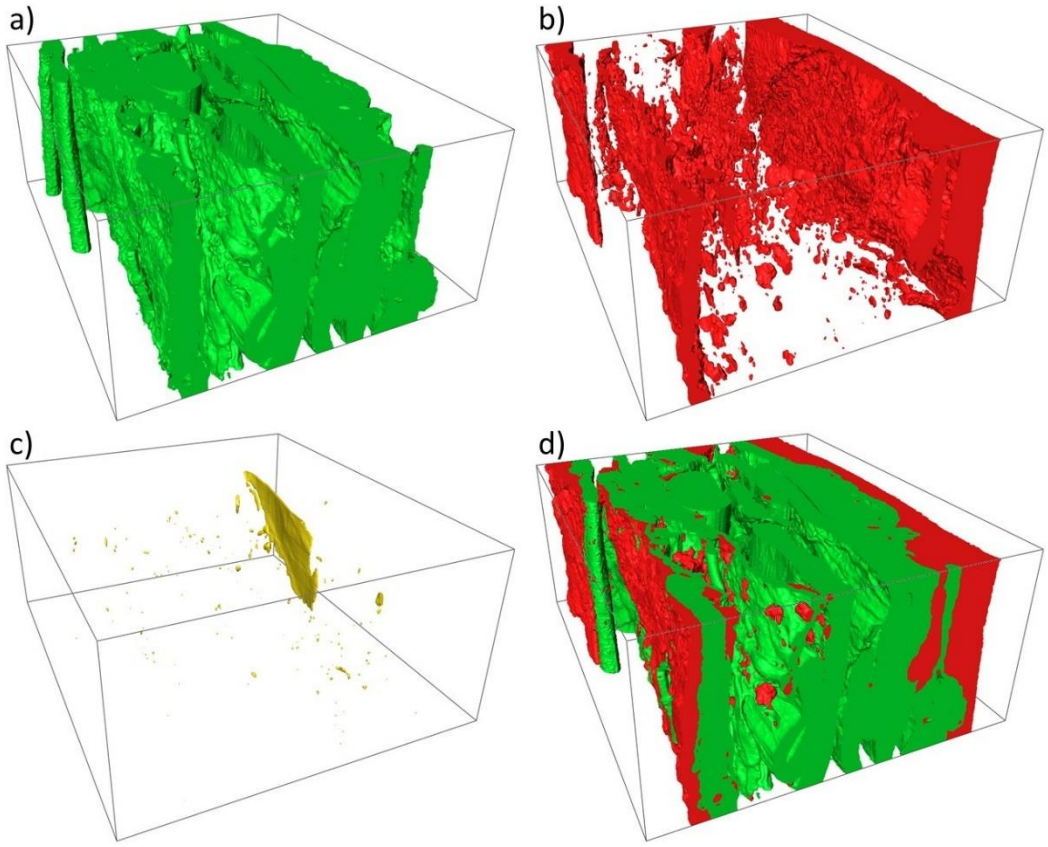

Figure 86: Volume reconstruction of the individual phases of the paper label: (a) cellulose, (b) filler material, (c) voids, (d) combined volumes of cellulose and filler material. (box size: 56x65x30 µm³)

7.7 Conclusion *ATUMtome* & *Atlas 5*

The usage of *ATUMtome* for array tomography is a very promising technique for investigating 3D volumes within the SEM. With this method it is possible to prepare larger sample volumes for investigations in a semi-destructive manner. The sample gets cut into slices, but the slices are collected on a polymer tape. This enables the repetitions of some SEM recordings at a later stage. The availability of the slices on the wafer gives the additional possibility to perform different spectroscopic measurements (EDX, Raman) of the same sample which was verified in this work in the previous chapter.

Atlas 5 itself is a very powerful imaging software for large area investigations or large section sets. Unfortunately, the software needs much manual input to work properly and to deliver good results.

The real drawback of this method is the limited number of materials which can be investigated. The origin of the method in life sciences is obvious. Most samples in life sciences are sliceable and able to be collected in section ribbons. In a materials science point of view, it is very challenging to find suitable materials for this technique. Many materials like light metals or alloys are sliceable but the slices cannot be collected because they break. Polymeric materials are often too soft for successful cutting. Layered materials can separate after cutting.

For the test of this method a paper sample (well-known in materials science) was chosen. The same sample was successfully investigated with *3View* for a 3D reconstruction in this work. The test sample was very problematic for the investigation with *ATUMtome*, because the water in the knife boat, which is used as transfer medium between knife and tape, interacts with the sample (the cellulose swells) and a changed sample is not usable for a further investigation.

8 Summary, Conclusion and Outlook

8.1 Summary

This thesis had two main aims: the possibility to combine serial block-face scanning electron microscopy (SBFSEM) with spectroscopic techniques and a test of the method automated tape collecting ultramicrotomy (ATUM) in the scope of materials science. With these tasks the field of correlative scanning electron microscopy can be enlarged.

For the combination of the SBFSEM device *3View* with energy dispersive X-ray spectroscopy (EDX), also called *3D elemental mapping*, in a first step the newly installed EDX detector *Element* from *EDAX* was characterized. The acquisition parameters of the spectrum images were chosen to have a reasonable recording time. In the test of *3D elemental mapping* the general process worked well, but it was not possible to replicate the results of a previous investigation at the FELMI-ZFE with an alternative detector. The main problem is the EDX detector which does not allow the recording of spectrum images with a sufficient energy resolution. Additionally the quantification with the *EDAX APEX* software of the EDX detector was troublesome for L-lines. The calculated concentration of some elements was significantly too low. During the experiment with EDX it was discovered that the backscattered electron (BSE) detector shadows the EDX detector in its conventional position. For recording of BSE images during *3D elemental mapping* a special detector holder was developed.

Within this thesis it was possible to implement the first combination of *3View* and Raman spectroscopy in the world. Combining *3View* and Raman spectroscopy needs a transfer to a second scanning electron microscope. In order to make this transfer possible the rotational alignment in 3View was improved and for the *3View* sample holder a fixating ring was manufactured. With the test of a special paper sample with a layered structure this technique could be successfully performed. Before the *3View* imaging process and after several stacks of 200 cuts Raman spot measurements were executed for further characterization of the material.

The ATUM device *ATUMtome*, which collects the sections cut by an ultramicrotome on a polymer tape, was tested for its capability in materials science. As test sample a paper label was chosen. During the recordings of the sections in the SEM it was found that the sections got wrinkles during the cutting process. With these wrinkles it was not possible to evaluate the images in a meaningful way because of width changes for two consecutive sections. For the evaluation in terms of image segmentation the machine learning software *ilastik* was tested. Despite bad image quality of the sections, the segmentation of one phase could be performed. For SBFSEM images the software *ilastik* was used for successful image segmentation. Additionally to imaging of a materials science sample prepared with ATUM also the possibility of spectroscopic measurements on the sections was tested. These tests had promising results for further investigations. EDX measurements can easily be performed on the prepared sections. Due to fluorescence successful Raman measurements could only be performed at some spots.

8.2 Conclusion

During a *3View* investigation with EDX (*3D elemental mapping*) a special holder for the BSE detector is needed which was manufactured during this work. The *EDAX APEX* software of the EDX detector has problems in quantifying the L-lines. To overcome this problem an alternative software has to be used or a quantification routine has to be programed. If these two problems are solved meaningful EDX is possible in combination with *3View*. The combination of Raman with *3View* (or similar *slice and view* techniques) is possible with the improved alignment routines. For a simple usage of this combination additional automated processes like the alignment of two following image stacks should be developed. During the preparation of a sample with *ATUMtome* it has contact with water. For materials which react with water this can be problematic. The machine learning software *ilastik* produces useful image segmentations with less needed preceding image enhancement and is therefore more efficient than alternative methods.

8.3 Outlook

8.3.1 Combining *3View* with Spectroscopic Methods

The technique *3D elemental mapping* is working, but a better EDX detector is needed for good results. Also, the implementation of automation would provide the possibility to record spectrum images with a long pixel dwell time for a higher number of counts in the pixel spectra. The combination of *3View* with Raman spectroscopy should be repeated with a sample of 3D Raman interest. For an shorter faster experiment time the alignment process in *3View* should be further improved. The rotational alignment could be enhanced by a goniometer on the *3View* sample holder.

8.3.2 *ATUMtome* in Materials Science

The technique itself and the possibility to combine it with spectroscopic measurements is very promising. In future it would be interesting to find materials science samples which can be cut in *ATUMtome* without distortions. On these samples correlative microscopy can then be performed with devices like *RISE*. In the near future it should be tested if a metallized polymer tape improves the Raman measurements significantly. Also the possibility of Raman mappings on the slices should be tested.

References

Aluminium Batz + Burgel, 2019. EN AW-2024 [WWW Document]. URL https://batz-burgel.com/metallhandel/lieferant-aluminium/en-aw-2024/ (accessed 2.20.21).

Baena, V., Schalek, R.L., Lichtman, J.W., Terasaki, M., 2019. Serial-section electron microscopy using automated tape-collecting ultramicrotome (ATUM), in: Methods in Cell Biology. Academic Press Inc., pp. 41–67. https://doi.org/10.1016/bs.mcb.2019.04.004

Berg, S., Kutra, D., Kroeger, T., Straehle, C.N., Kausler, B.X., Haubold, C., Schiegg, M., Ales, J., Beier, T., Rudy, M., Eren, K., Cervantes, J.I., Xu, B., Beuttenmueller, F., Wolny, A., Zhang, C., Koethe, U., Hamprecht, F.A., Kreshuk, A., 2019. ilastik: interactive machine learning for (bio)image analysis. Nature Methods 16, 1226–1232. https://doi.org/10.1038/s41592-019-0582-9

Böhm, T., Moroni, R., Thiele, S., 2020. Serial section Raman tomography with 10 times higher depth resolution than confocal Raman microscopy. Journal of Raman Spectroscopy 51, 1160–1171. https://doi.org/10.1002/jrs.5878

Buades, A., Coll, B., Morel, J.-M., 2011. Non-Local Means Denoising. Image Processing On Line 1, 2011–2020. https://doi.org/10.5201/ipol.2011.bcm_nlm

Danilatos, G.D., 1991. Review and outline of environmental SEM at present. Journal of Microscopy 162, 391–402. https://doi.org/10.1111/j.1365-2818.1991.tb03149.x

Danilatos, G.D., 1988. Foundations of Environmental Scanning Electron Microscopy. Advances in Electronics and Electron Physics 71, 109–250. https://doi.org/10.1016/S0065-2539(08)60902-6

Darbon, J., Cunha, A., Chan, T.F., Osher, S., Jensen, G.J., 2008. Fast nonlocal filtering applied to electron cryomicroscopy, in: 2008 5th IEEE International Symposium on Biomedical Imaging: From Nano to Macro, Proceedings, ISBI. pp. 1331–1334. https://doi.org/10.1109/ISBI.2008.4541250

Denk, W., Horstmann, H., 2004. Serial Block-Face Scanning Electron Microscopy to Reconstruct Three-Dimensional Tissue Nanostructure. PLoS Biology 2, e329. https://doi.org/10.1371/journal.pbio.0020329

Drouin, D., Couture, A.R., Joly, D., Tastet, X., Aimez, V., Gauvin, R., 2007. CASINO V2.42—A Fast and Easy-to-use Modeling Tool for Scanning Electron Microscopy and Microanalysis Users. Scanning 29, 92–101. https://doi.org/10.1002/sca.20000

Gauvin, R., 1999. Some theoretical considerations on X-ray microanalysis in the environmental or variable pressure scanning electron microscope. Scanning 21, 388–393. https://doi.org/10.1002/sca.4950210605

Genoud, C., Galloway, S., Pfeiffer, S., Kraus, B., 2008. Automatic acquisition of large amounts of 3D data at the ultrastructural level, using SBFSEM. Microscopy and Microanalysis 14, 1614–1615. https://doi.org/10.1017/S1431927608081658

Goldstein, J.I., Newbury, D.E., Michael, J.R., Ritchie, N.W.M., Scott, J.H.J., Joy, D.C., 2017. Scanning electron microscopy and x-ray microanalysis, Scanning Electron Microscopy and X-ray Microanalysis. https://doi.org/10.1007/978-1-4939-6676-9

Hayworth, K.J., Morgan, J.L., Schalek, R., Berger, D.R., Hildebrand, D.G.C., Lichtman, J.W., 2014. Imaging ATUM ultrathin section libraries with WaferMapper: a multi-scale approach to EM reconstruction of neural circuits. Frontiers in Neural Circuits 8, 68. https://doi.org/10.3389/fncir.2014.00068

JASCO, 2021. Confocal Raman Microscopy (The Basics) | JASCO [WWW Document]. URL https://jascoinc.com/learning-center/theory-of-spectroscopy/confocalramanmicroscopy/ (accessed 3.28.21).

Kubota, Y., Sohn, J., Hatada, S., Schurr, M., Straehle, J., Gour, A., Neujahr, R., Miki, T., Mikula, S., Kawaguchi, Y., 2018. A carbon nanotube tape for serial-section electron microscopy of brain ultrastructure. Nature Communications 9, 1–15. https://doi.org/10.1038/s41467-017-02768-7

Long, D.A., 2002. The Raman Effect: A Unified Treatment of the Theory of Raman Scattering by Molecules. John Wiley & Sons, Ltd, Chichester, UK. https://doi.org/10.1002/0470845767

Michler, G.H., 2019. Kompakte Einführung in die Elektronenmikroskopie, essentials. Springer Fachmedien Wiesbaden, Wiesbaden. https://doi.org/10.1007/978-3-658-26688-2

Schaffer, M., Wagner, J., Schaffer, B., Schmied, M., Mulders, H., 2007. Automated three-dimensional X-ray analysis using a dual-beam FIB. Ultramicroscopy 107, 587–597. https://doi.org/10.1016/j.ultramic.2006.11.007

Schalek, R., Kasthuri, N., Hayworth, K., Berger, D., Tapia, J., Morgan, J., Turaga, S., Fagerholm, E., Seung, H., Lichtman, J., 2011. Development of High-Throughput, High-Resolution 3D Reconstruction of Large-Volume Biological Tissue Using Automated Tape Collection Ultramicrotomy and Scanning Electron Microscopy. Microscopy and Microanalysis 17, 966–967. https://doi.org/10.1017/s1431927611005708

Schindelin, J., Arganda-Carreras, I., Frise, E., Kaynig, V., Longair, M., Pietzsch, T., Preibisch, S., Rueden, C., Saalfeld, S., Schmid, B., Tinevez, J.Y., White, D.J., Hartenstein, V., Eliceiri, K., Tomancak, P., Cardona, A., 2012. Fiji: An open-source platform for biological-image analysis. Nature Methods 9, 676–682. https://doi.org/10.1038/nmeth.2019

Schmidt, R., Fitzek, H., Nachtnebel, M., Mayrhofer, C., Schroettner, H., Zankel, A., 2019. The Combination of Electron Microscopy, Raman Microscopy and Energy Dispersive X-Ray

Spectroscopy for the Investigation of Polymeric Materials. Macromolecular Symposia 384. https://doi.org/10.1002/masy.201800237

Shabestari, S.G., Ghoncheh, M.H., Momeni, H., 2014. Evaluation of formation of intermetallic compounds in Al2024 alloy using thermal analysis technique. Thermochimica Acta 589, 174–182. https://doi.org/10.1016/j.tca.2014.05.024

Ul-Hamid, A., 2018. A Beginners' Guide to Scanning Electron Microscopy, A Beginners' Guide to Scanning Electron Microscopy. Springer International Publishing. https://doi.org/10.1007/978-3-319-98482-7

Vandenabeele, P., 2013. Practical Raman Spectroscopy - An Introduction, Practical Raman Spectroscopy - An Introduction. John Wiley & Sons, Ltd, Chichester, UK. https://doi.org/10.1002/9781119961284

Wagner, T., Behnel, P., 2016. ij-nl-means: Non local means 1.4.6 [WWW Document]. https://doi.org/10.5281/ZENODO.47468

Zankel, A., Kraus, B., Poelt, P., Schaffer, M., Ingolic, E., 2009. Ultramicrotomy in the ESEM, a versatile method for materials and life sciences. Journal of Microscopy 233, 140–148. https://doi.org/10.1111/j.1365-2818.2008.03104.x

Zankel, A., Reingruber, H., Schröttner, H., 2011. 3D Elemental Mapping in the ESEM A Combination of Serial Block-face SEM and EDS. Imaging & microscopy 2, 35–37.

Zankel, A., Wagner, J., Poelt, P., 2014. Serial sectioning methods for 3D investigations in materials science. Micron 62, 66–78. https://doi.org/10.1016/j.micron.2014.03.002

Appendix

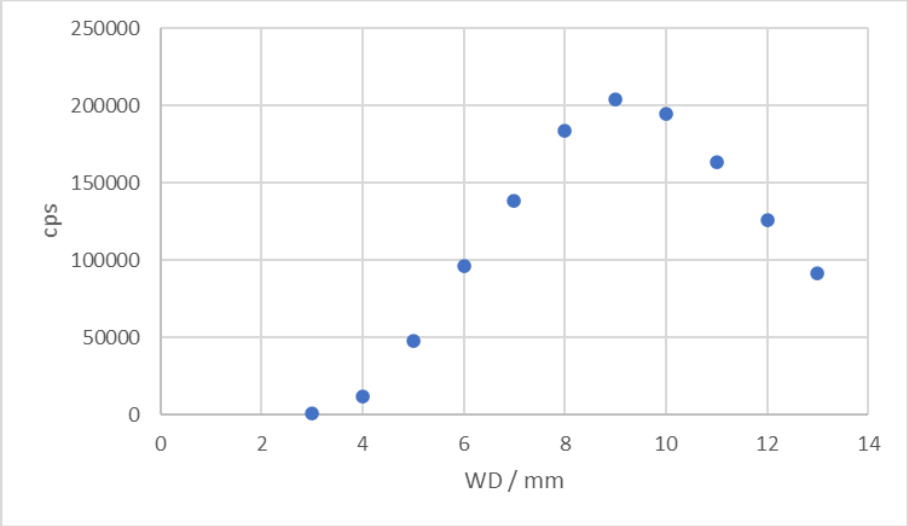

Figure 87: Measurement of the count rates at different values of the working distance (WD) for determining the intersection distance of the *EDAX Element* detector

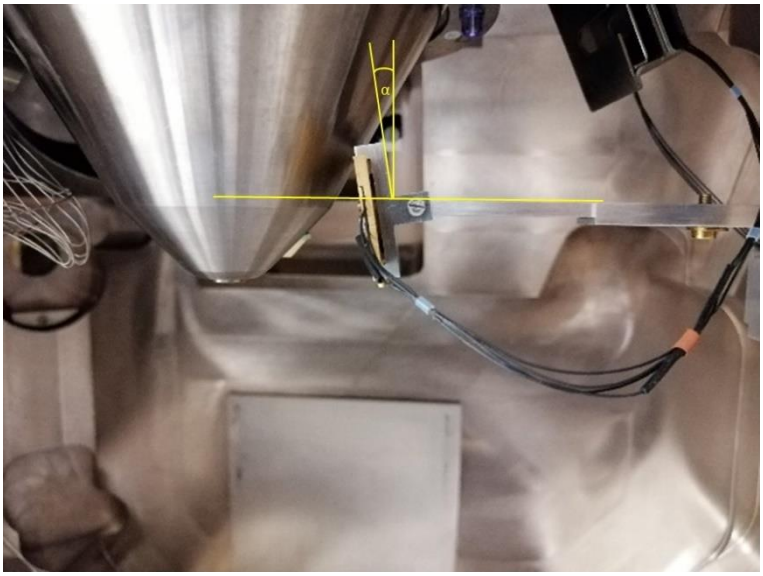

Figure 88: Sketch of the angle measurement with photographs and square during the BSE detector holder test

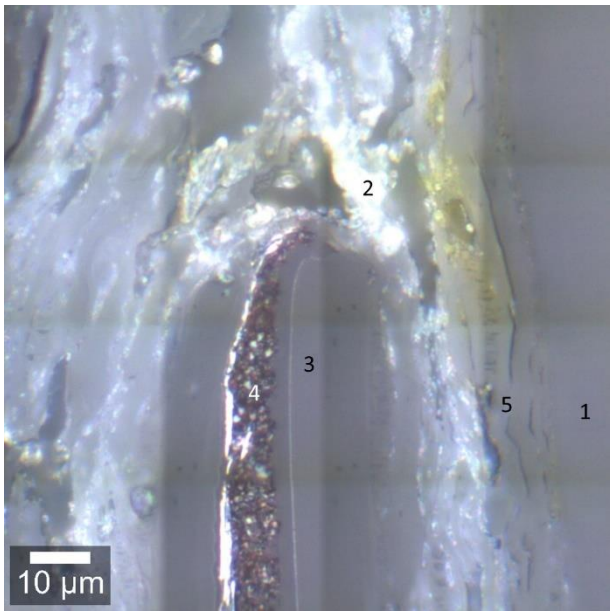

Figure 89: Stitched LIMI image of the sample block-face for the Raman measurements after slice 400. The numbers mark the positions where the spot measurements were performed.

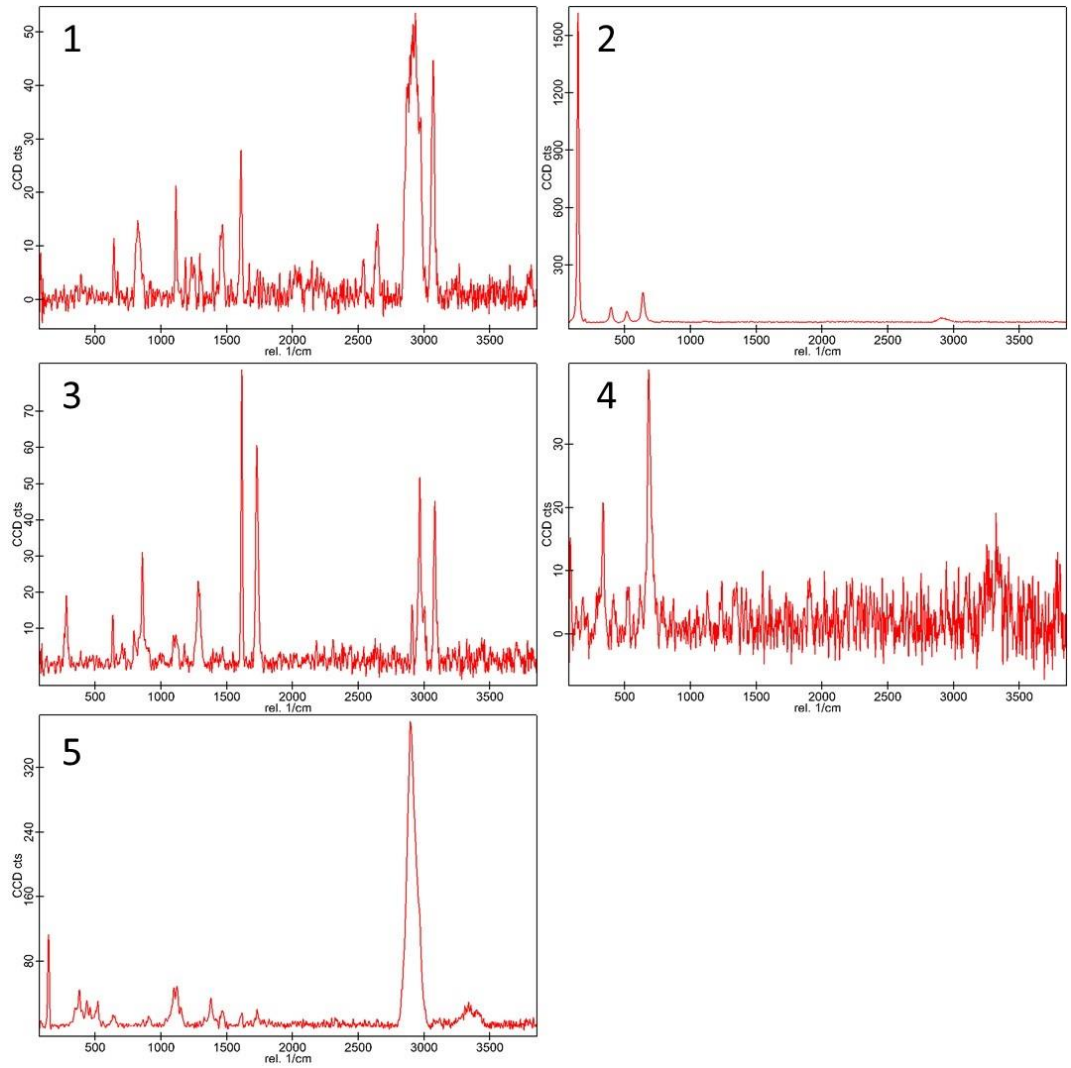

Figure 90: Raman spectra of the marked spots in Figure 89: (1) resin, (2) TiO_2 – anatase, (3) PET, (4) iron oxide, (5) cellulose

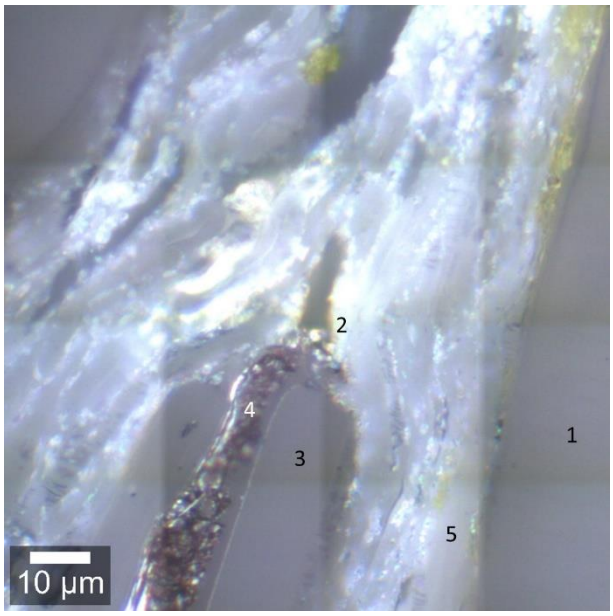

Figure 91: Stitched LIMI image of the sample block-face for the Raman measurements after slice 600. The numbers mark the positions where the spot measurements were performed.

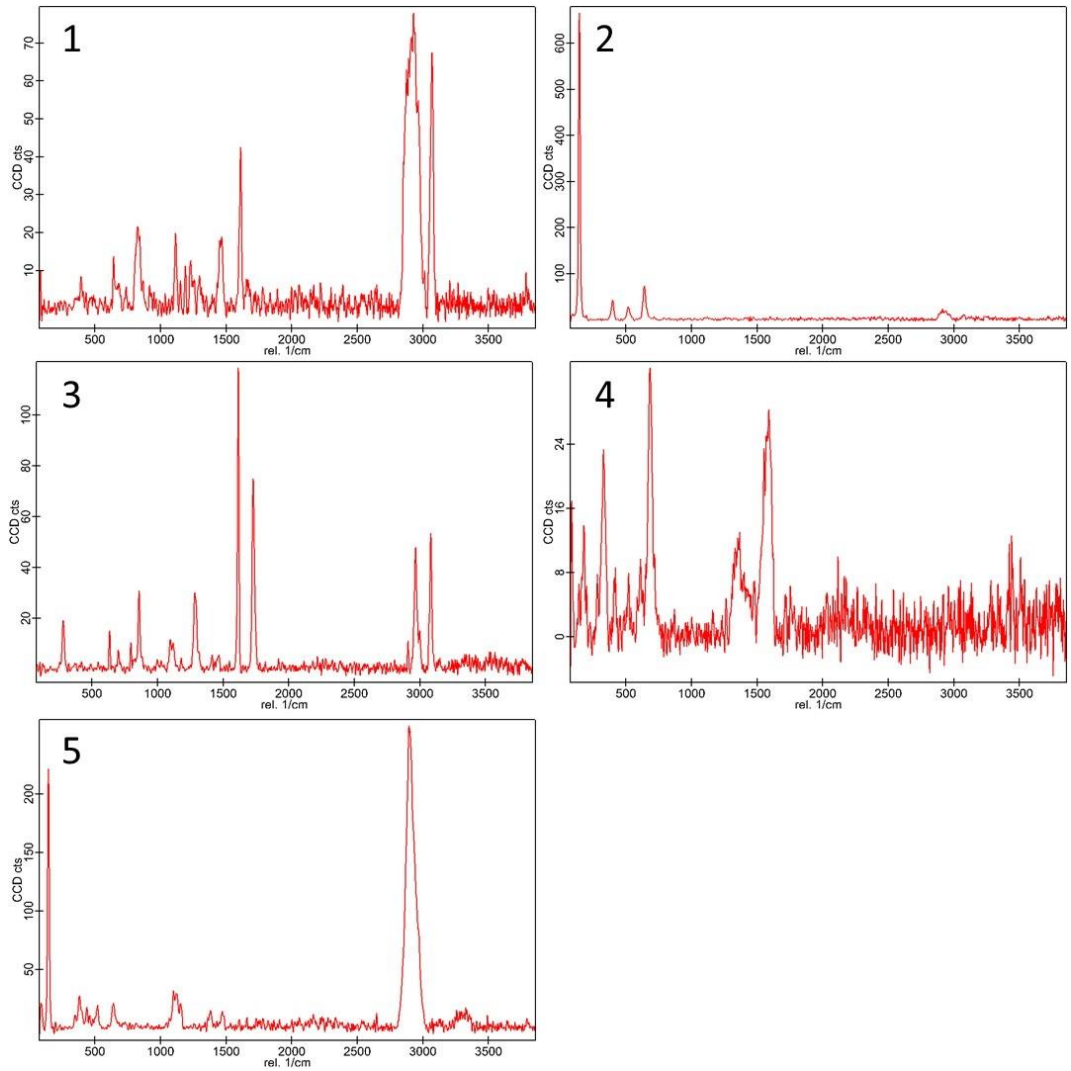

Figure 92: Raman spectra of the marked spots in Figure 91: (1) resin, (2) TiO_2 – anatase, (3) PET, (4) iron oxide, (5) cellulose

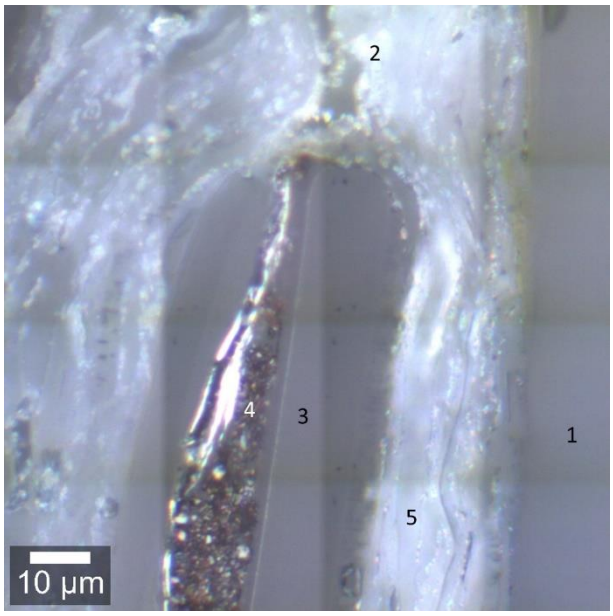

Figure 93: Stitched LIMI image of the sample block-face for the Raman measurements after slice 800. The numbers mark the positions where the spot measurements were performed.

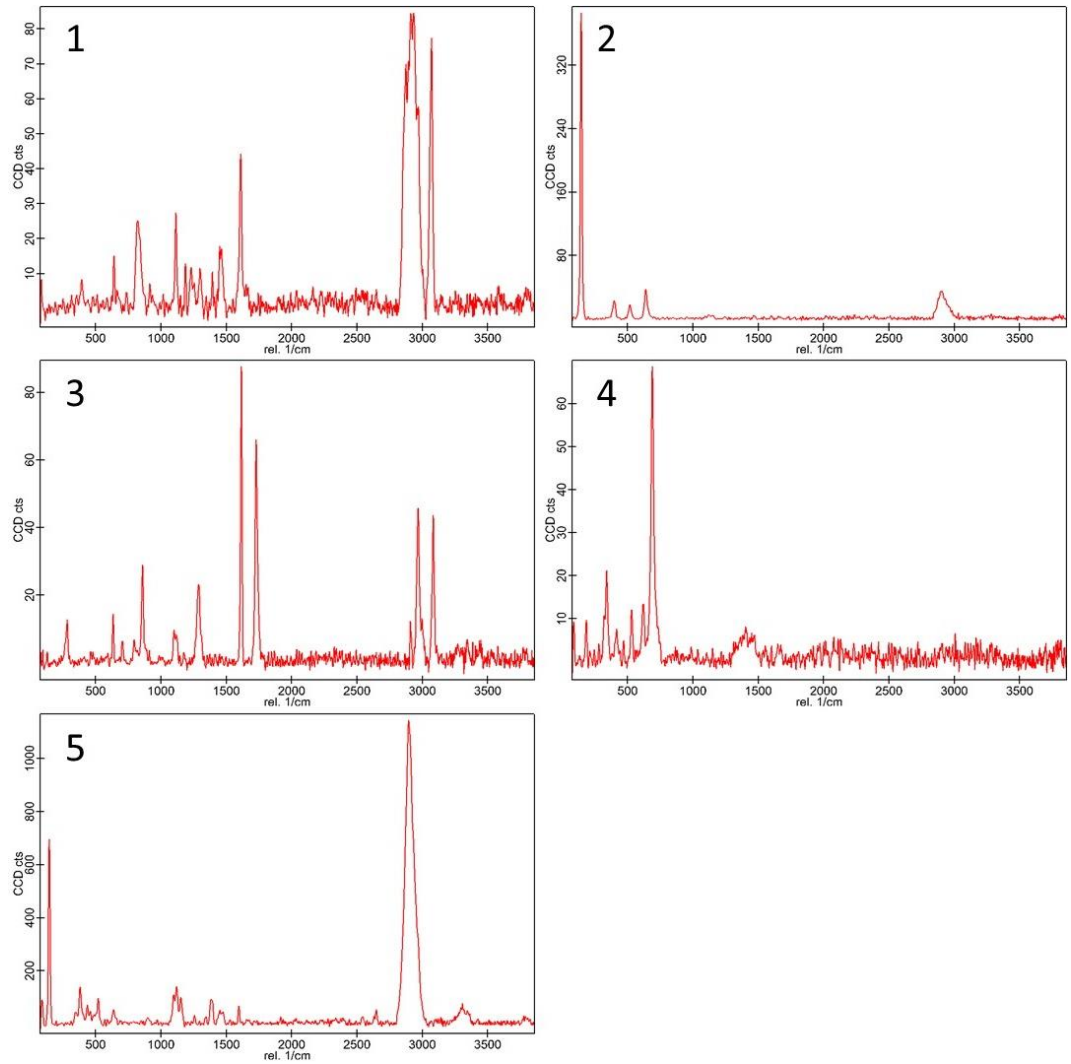

Figure 94: Raman spectra of the marked spots in Figure 93: (1) resin, (2) TiO_2 – anatase, (3) PET, (4) iron oxide, (5) cellulose

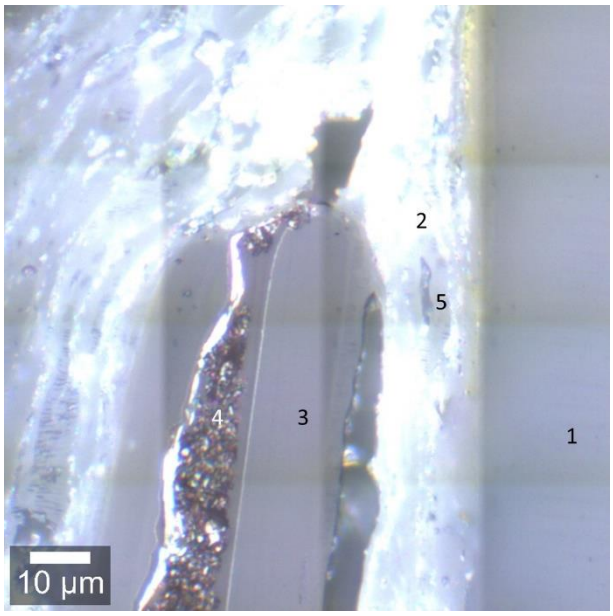

Figure 95: Stitched LIMI image of the sample block-face for the Raman measurements after slice 1000. The numbers mark the positions where the spot measurements were performed.

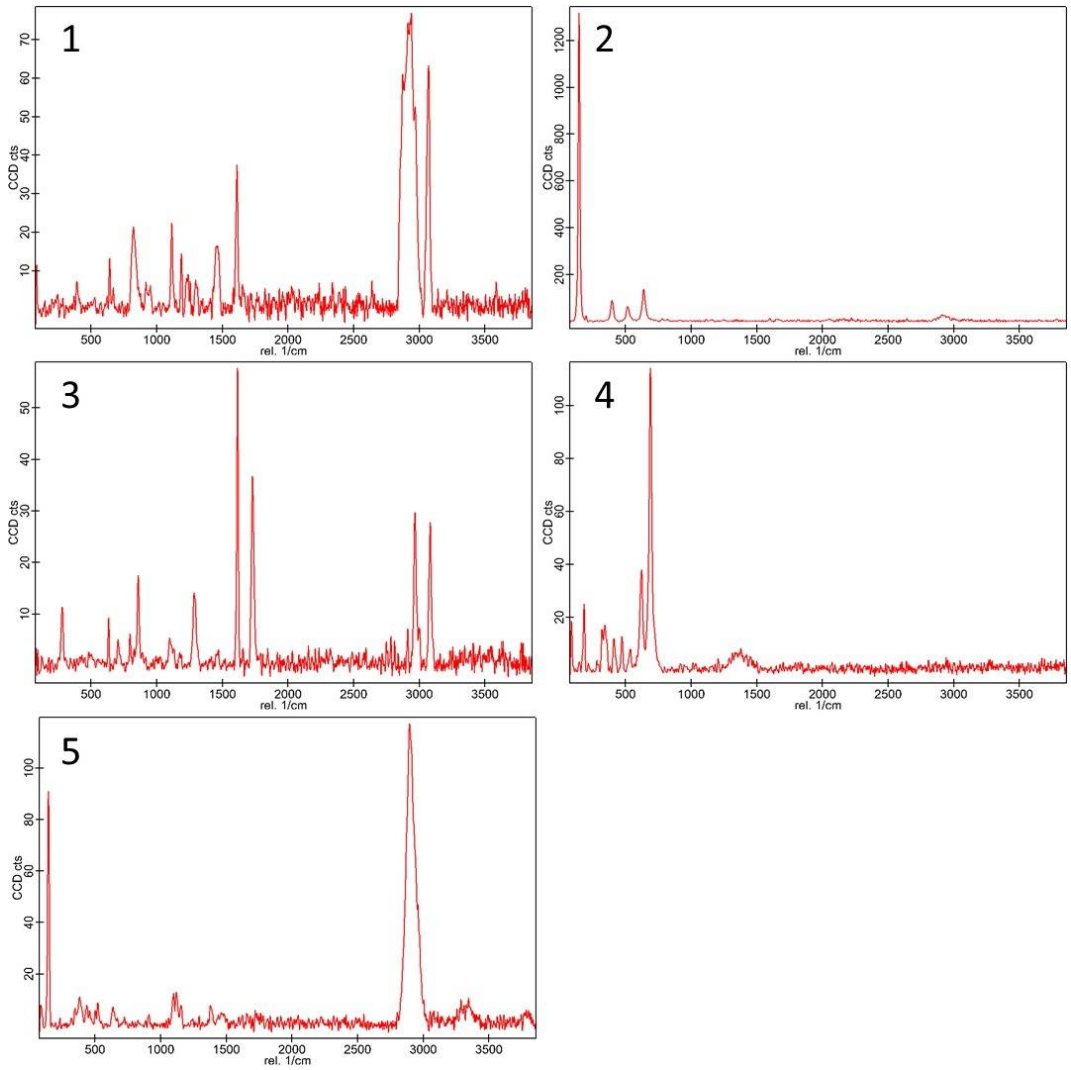

Figure 96: Raman spectra of the marked spots in Figure 95: (1) resin, (2) TiO_2 – anatase, (3) PET, (4) iron oxide, (5) cellulose

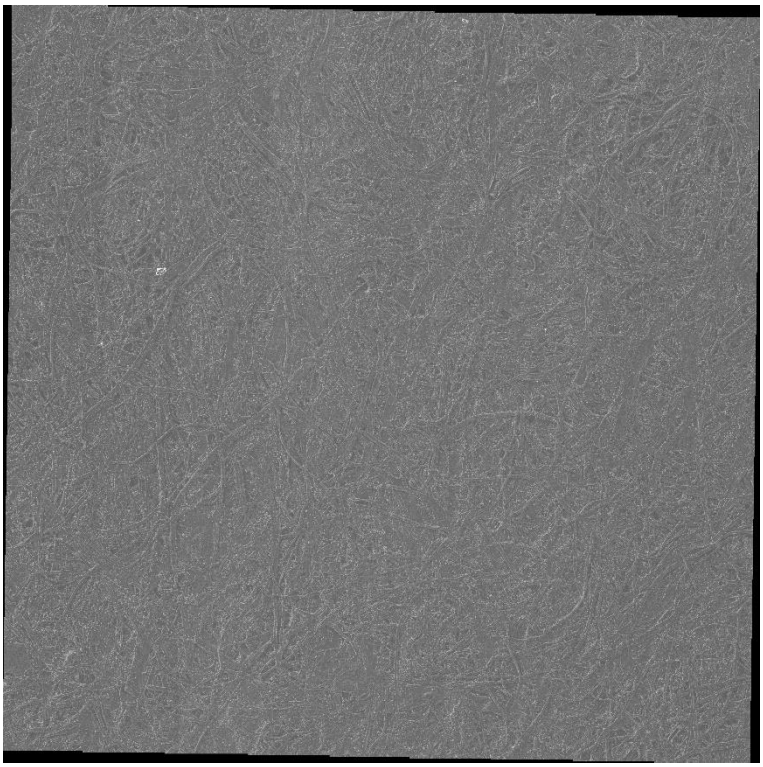

Figure 97: Large area image of the paper sample recorded with *AZtec* (image width: 3.2 mm, SE image)

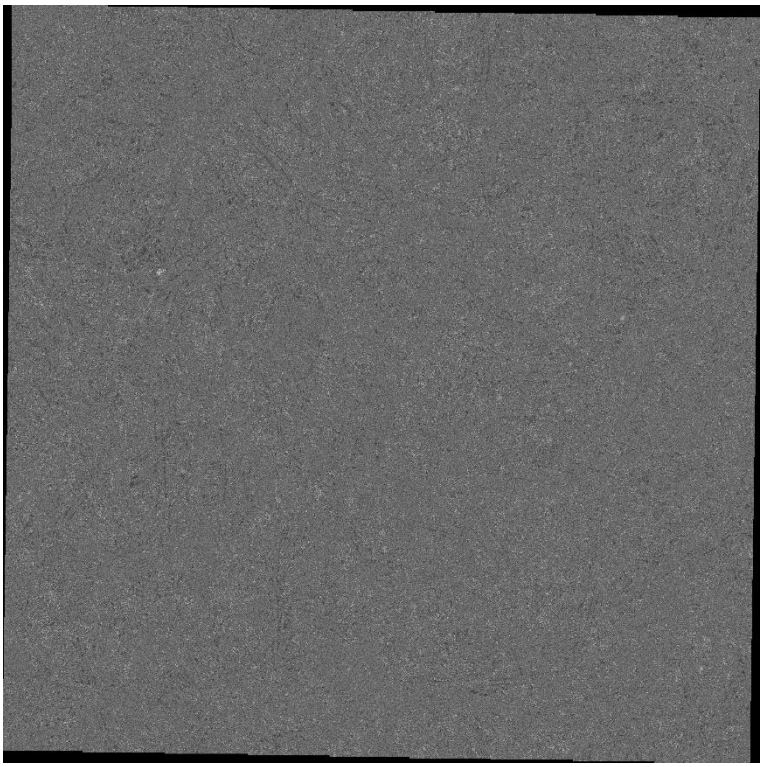

Figure 98: Large area image of the paper sample recorded with *AZtec* (image width: 3.2 mm, BSE image)

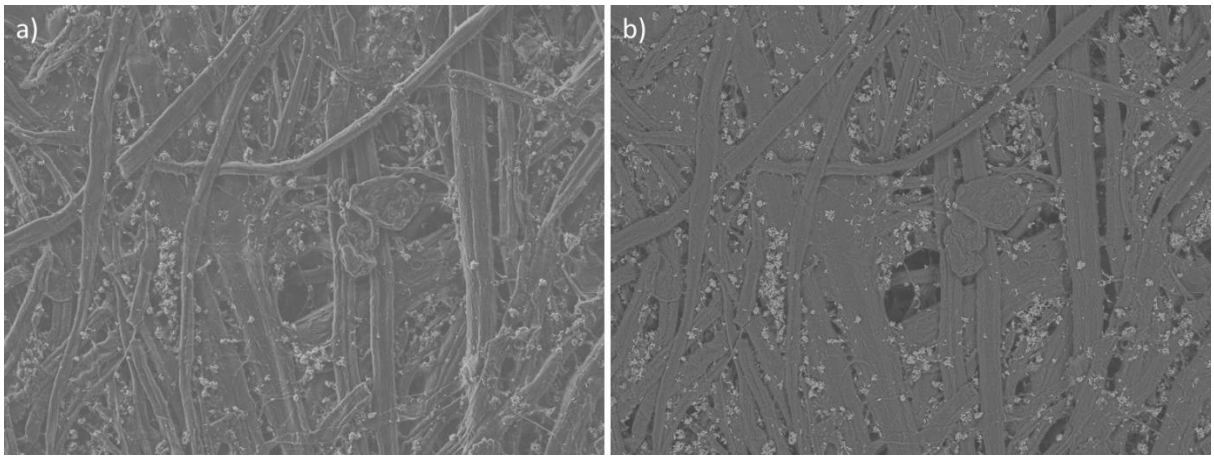

Figure 99: Zoom into the large area image of the paper sample recorded with *AZtec:* (a) SE image, (b) BSE image. (image width: 410 µm)